# Deceleration and Electron Cooling of Highly Charged Ions at HITRAP

TECHNISCHE UNIVERSITÄT DARMSTADT

Fachbereich Physik
Institut für Kernphysik
AG Nörtershäuser

LASER SpHERe

Deceleration and Electron Cooling of Highly Charged Ions at HITRAP
Abbremsung und Elektronenkühlung von Hochgeladenen Ionen an HITRAP

Accepted doctoral thesis by Simon Rausch

Date of submission: 10.10.2024
Date of thesis defense: 04.11.2024

Darmstadt, Technische Universität Darmstadt

# Erklärungen laut Promotionsordnung

### §8 Abs. 1 lit. c PromO

Ich versichere hiermit, dass die elektronische Version meiner Dissertation mit der schriftlichen Version übereinstimmt.

### §8 Abs. 1 lit. d PromO

Ich versichere hiermit, dass zu einem vorherigen Zeitpunkt noch keine Promotion versucht wurde. In diesem Fall sind nähere Angaben über Zeitpunkt, Hochschule, Dissertationsthema und Ergebnis dieses Versuchs mitzuteilen.

### §9 Abs. 1 PromO

Ich versichere hiermit, dass die vorliegende Dissertation selbstständig und nur unter Verwendung der angegebenen Quellen verfasst wurde.

### §9 Abs. 2 PromO

Die Arbeit hat bisher noch nicht zu Prüfungszwecken gedient.

Darmstadt, 10.10.2024

_____

S. Rausch

# Kurzfassung

Die Untersuchung hochgeladener Ionen (HCI) bietet die Möglichkeit, Umgebungen nachzubilden, die auf der Erde sonst nicht zugänglich sind. So entsprechen die magnetischen Feldstärken, die Elektronen in wasserstoffartigen Ionen in der Nähe der Kernoberfläche erfahren, denen in der Umgebung eines Pulsars. Damit lassen sich beispielsweise grundlegende Theorien wie die Quantenelektrodynamik (QED) in solchen Feldern überprüfen. Die höchste Präzision wird in der Regel bei Experimenten mit gekühlten und gespeicherten Ionen in einer Ionenfalle erreicht. Bislang ist dies jedoch nur für leichte und mittelschwere hochgeladene Ionen möglich.

Die Erzeugung großer Mengen schwerer, hochgeladener Ionen, wie z.B. wasserstoffartigem Uran $U^{91+}$, beruht auf dem Herauslösen von Elektronen bei hohen kinetischen Energien. Diese Technik wird üblicherweise in Beschleunigeranlagen wie dem GSI Helmholtzzentrum für Schwerionenforschung in Deutschland eingesetzt. Um schwere HCI in einer Ionenfalle für Präzisionsexperimente einzufangen, ist eine vorherige Abbremsung im Anschluss an den Produktionsprozess erforderlich. Dies ist das Ziel der HITRAP-Anlage an der GSI, bei der die Energie des Ionenstrahls in einem Linearbeschleuniger reduziert wird. Anschließend sollen die Ionen in einer Penningfalle eingefangen und mittels Elektronenkühlung für den Weitertransport zu den Präzisionsexperimenten gekühlt werden.

Im Rahmen dieser Arbeit wurde der Linearbeschleuniger nach fast acht Jahren Stillstand wieder in Betrieb genommen. Dazu wurden mit der Beschleunigeranlage der GSI $^{36}Ar^{18+}$ Ionen erzeugt, im Experimentierspeichering ESR auf 4 MeV/u abgebremst und in die HITRAP Anlage eingespeist. Nach erfolgreicher Abbremsung wurden erstmals hochgeladene Ionen aus dem ESR entlang der Niederenergiestrahllinie zur HITRAP Kühlfalle transportiert, dort eingefangen und nachweißlich für kurze Zeit gespeichert. Zusätzlich wurde der Fallenaufbau mit $^{40}Ar^{16+}$ Ionen aus einer Elektronenstrahlionenquelle (EBIT) in Betrieb genommen. Die gleichzeitige Speicherung dieser Ionen und eines kalten Elektronenplasmas führte zu einer deutlichen Verringerung der kinetischen Energie der Ionen. Dies ist die erste erfolgreiche Demonstration von Elektronenkühlung an hochgeladenen Ionen in einer Penning-Falle. Zusammen mit der ersten erfolgreichen Speicherung der im Beschleuniger erzeugten HCI stellt dies einen gewaltigen Fortschritt bei der Inbetriebnahme der HITRAP-Anlage dar, in dessen Folge für das kommende Jahr erstmalig ein Experiment an HITRAP in den Strahlzeitplan der GSI aufgenommen wurde.

# Abstract

The investigation of highly charged ions (HCI) offers the potential to recreate environments that are otherwise inaccessible on Earth. For instance, the magnetic field experienced by electrons in hydrogen-like heavy ions close to the surface of the nucleus compares to that in the vicinity of a pulsar. Consequently, this allows for the most stringent tests of fundamental theories, such as quantum electrodynamics (QED), in these extreme fields. Ultimate precision is typically attained in experiments conducted on cooled and confined ions in an ion trap. However, to date this remains a viable option only for light and medium-heavy, highly charged ions.

The production process of large quantities of heavy, highly charged ions, such as hydrogen-like uranium $U^{91+}$, relies on electron stripping at high kinetic energies. This technique is commonly employed in accelerator facilities, such as the heavy ion research facility GSI Helmholtzzentrum für Schwerionenforschung in Germany. In order to confine heavy HCI in an ion trap for precision experiments, prior deceleration subsequent to the production process is necessary. This constitutes the objective of the HITRAP facility at GSI, where the energy of the ion beam is reduced in a linear decelerator. Subsequently, the ions will be captured in a Penning trap and cooled by the application of electron cooling for further transport to precision experiments.

In the context of the work, the linear decelerator was recommissioned following a shutdown period of almost eight years. For this purpose, $^{36}Ar^{18+}$ ions were produced by the accelerator complex of GSI, decelerated to 4 MeV/u in the Experimental Storage Ring ESR, and injected into the HITRAP facility. After successful deceleration, the ion beam was transported for the first time further along the low-energy beam line towards the HITRAP Cooling Trap, captured, and confined for short periods of time. Furthermore, the trap setup was commissioned with $^{40}Ar^{16+}$ ions produced by an electron beam ion trap (EBIT). The simultaneous storage of these ions with a cold plasma of electrons resulted in an considerable reduction of the ions' kinetic energy. This constitutes the first demonstration of electron cooling on highly charged ions in a Penning trap. Together with the first successful storage of accelerator-produced HCI, this marks a tremendous advancement in the commissioning of the HITRAP facility, as a result of which an experiment at HITRAP has been included for the first time in the beamtime schedule of GSI for the upcoming year.

# Contents

# List of Figures

# List of Tables

# 1 Introduction

Highly charged ions (HCI) can naturally only be found in the most extreme conditions in the universe as for instance present within stars or supernovae. With the development of ion sources for higher charge states and accelerator facilities in the mid of the 20th century, these ions became also available for investigations in laboratory environments [1, 2]. Since then, highly charged ions constitute an active field of study in numerous research sectors of physics. Their applications span a range of fields, from cancer treatment by ion-beam irradiation over the development of new standards for atomic clocks to the most stringent tests of fundamental theories [3–5].

For example, quantum electrodynamics (QED) represents the experimentally most precisely confirmed theory for light and medium-heavy, highly charged ions [6, 7]. In the case of heavy HCI on the other hand, current technically feasible experiments are unable to achieve the same level of precision [8]. Consequently, the theoretical predictions of QED effects in the extreme conditions present close to a heavy nucleus remain without experimental confirmation.

This limitation is related to the production process of heavy HCI. While light and medium-heavy isotopes can be produced in the highest charge states and in large quantities in comparatively small ion sources [9, 10], the heaviest elements remain practically inaccessible with these kinds of sources. To date, only acceleration to velocities approaching the speed of light by particle accelerators and subsequent electron stripping by solid targets enables the production of the heaviest elements in their highest charge states and in large quantities, such as bare uranium [11]. A leading facility for research on highly charged ions that employs this approach is the GSI Helmholtzzentrum für Schwerionenforschung in Germany, where any stable isotope, as well as several unstable isotopes can be produced in an arbitrary charge state.

At these high kinetic energies, the precision of experiments is often limited by the uncertainty associated with the knowledge of the ions' velocity [12]. An examination of the most precisely performed experiments on charged particles reveals that they are most commonly conducted within particle traps [7, 13–15]. In order to confine heavy HCI produced at high kinetic energies in an ion trap, prior deceleration is required.

This outlines the objective of the HITRAP project, which is a unique facility located at GSI that aims to provide the heaviest elements for precision experiments [16]. Currently, there are four experimental setups already established or in preparation, that will employ heavy highly charged ions at low kinetic energies, ranging from laser spectroscopy in a Penning trap to the application of HCI for optical clocks [17–20]. Following production in the GSI accelerator facility and a first deceleration step in the Experimental Storage Ring (ESR), the HCI are transported towards HITRAP with a kinetic energy of 4 MeV/u. Subsequently, the energy is further reduced in a two-stage linear decelerator down to only 6 keV/u, employing a combination of several bunchers, an interdigital H-type linac, and a radiofrequency quadrupole (RFQ). In 2014, the linear decelerator could be successfully commissioned, when decelerated ions were detected

after the second deceleration stage [21]. After this achievement, an almost eight-year-long period of shutdown with no operation of the decelerator followed. The recommissioning of the linear decelerator represents one of the two major objectives of this work.

During the deceleration process, the energy width and emittance of the ion beam increase significantly, thereby rendering an efficient transport towards experimental setups unfeasible. The width of the energy distribution after the deceleration in the RFQ is observed to be approximately 1 keV/u. This challenge is addressed by the HITRAP Cooling Trap, a cryogenic setup comprising a seven-electrode cylindrical Penning trap. Subsequent to deceleration, the hot ion beam is captured in the trap simultaneously with a cold electron plasma which results in energy transfer via Coulomb interaction. The development and investigation of this process of electron cooling is the second major objective of this work.

Within three beamtimes in 2022 and 2024 the linear decelerator was successfully recommissioned. Moreover, for the first time, it was possible not only to transport the ions further along the beam line but also to capture accelerator-produced and decelerated ions within the Cooling Trap and confine them for an extended period of time. In addition, the process of electron cooling is investigated extensively with HCI produced by a local EBIT ion source. When stored simultaneously with an electron plasma in a nested-trap configuration, the reduction of the ions' kinetic energy is observed. Both the storage of accelerator-produced ions in a Penning trap and the observation of electron cooling on HCI were achieved within the scope of this work. These steps are also world-wide unique achievements and represent a significant advancement towards the finalisation of the commissioning process of the HITRAP facility.

# 2 Theoretical Background

This chapter presents a discussion of the theoretical background associated with the motivation, instrumentation and methods employed in this study. One of the major theoretical concepts that will eventually be studied extensively with ions from the HITRAP facility is that of quantum electrodynamics (QED), with particular focus on its reliability in extreme conditions. Such conditions are present in the vicinity of a heavy nucleus, where both the electric and magnetic field reach extreme values. In Sec 2.1, the underlying theory of two exemplary experiments testing the QED is presented. This will demonstrate the advantages of ion deceleration for superior precision, which comprises the application of cooling methods in an ion trap.

The second section, Sec. 2.2, outlines various approaches to the storage of charged particles, with a particular focus on cylindrical Penning traps. This includes the design of ion traps, as well as the motion of trapped charged particles and relevant detection schemes. Several cooling techniques are presented and discussed in Sec. 2.3 in the context of the main objective of this work, i.e., cooling of HCI with an initially broad energy distribution.

## 2.1 Testing QED with Highly Charged Ions

The study of highly charged ions (HCI) paves the way for a vast variety of applications and research fields. On the one hand, there are already established techniques in ion-beam therapy for the treatment of cancer patients, or applications currently under investigation, such as increasing the accuracy of atomic clocks with single HCI [3, 4, 18]. On the other hand, the unique characteristics of HCI render them an invaluable instrument for the assessment of theoretical frameworks, such as quantum electrodynamics.

In 1928, Paul Dirac laid the foundation for QED by unifying quantum mechanics and special relativity with his formulation of the Dirac equation [22]. It turned out that a fully relativistic equation cannot be formulated with a 'classical' wave function but requires a four-component spinor $\Psi(x)$. This was interpreted as the spin up and spin down components of a spin 1/2 particle, e.g. the electron, and its antimatter counterpart, the positron. When describing a spin 1/2 particle of mass $m_e$ in an orbit around the nucleus, this equation can be written as

$$(\gamma^\mu \hat{p}_\mu - m_e c)\Psi(x) = 0, \tag{2.1}$$

with the Dirac matrices $\gamma^\mu$ and momentum operator

$$\hat{p}_\mu = -i\hbar\partial_\mu. \tag{2.2}$$

Subsequently, the theory was further developed by Sin-Itiro Tomonaga, Julian Schwinger and Richard P. Feynman in the late 1940s, building upon Dirac's approach and explaining, e.g., the Lamb shift between the $^2S_{1/2}$ and $^2P_{1/2}$ levels in hydrogen and the deviation of the electron's

$g$-factor from the value predicted by the Dirac equation. Today, QED is the most accurately confirmed theory, as the experimentally derived value for the $g$-factor of a free electron agrees with the theoretical prediction within its relative uncertainty of $< 10^{-12}$ [13].

Furthermore, the $g$-factor of a bound electron has been determined with great precision through experimental means, with relative uncertainties in the order of $10^{-9}$ [6, 7, 23, 24]. It should be noted, however, that these highly precise tests of QED are currently limited to only light and medium-heavy isotopes. In the case of heavy HCI, such as hydrogen-like bismuth, the precision with which the $g$-factor of the ground-state electron can be measured is orders of magnitude lower, with a relative uncertainty of only $10^{-3}$ [8].

Another possible approach of testing the limits of QED is the determination of the hyperfine splitting of the ground-state. This phenomenon describes the splitting and shift of electronic energy levels in an atom or ion as a result of the magnetic field exerted by the nucleus [25]. An accurate theoretical description of the splitting is contingent upon not only the nuclear magnetic moment but also higher-order corrections stemming from QED. At present, the feasibility of measuring these QED corrections is limited by the uncertainty associated with the magnetic moment and another correction describing the magnetisation distribution within the nucleus, namely the Bohr-Weißkopf effect. For heavy ions, the uncertainty of the Bohr-Weißkopf effect is larger than the expected contribution of the QED correction, rendering a precise measurement impossible [26]. An experimental campaign has been proposed which would largely eliminate the Bohr-Weißkopf effect from the theoretical calculation, thereby providing access to testing of QED corrections [5, 27].

Both of the aforementioned approaches would provide a most stringent test of QED when performed with heavy HCI. The fields present in close proximity to the nucleus are otherwise unattainable in experimental environments and only occur in the most extreme conditions within the universe, as predicted on the surface neutron stars for example. To illustrate, the electric and magnetic fields at the surface of an uranium nucleus are in the order of $10^{19}$ V/cm and $10^{10}$ T, respectively [28]. At this field strength, the energy within a sphere with a radius equal to the Compton wavelength of an electron is almost sufficient to create an electron-positron pair (Schwinger limit) [29].

To date, QED has only been tested for light or medium-heavy ions with high precision, where the fields are orders of magnitude weaker. The most precise tests of bound state QED on heavy HCI are currently being conducted and planned within storage rings, where the accuracy of the measurement is mostly limited by the uncertainty of the ions kinetic energy [30]. Performing these investigations instead on ions stored in a trap, would consequently enhance the precision of the results. To this end, the HITRAP facility was designed with dedicated setups for $g$-factor and hyperfine splitting measurements [17, 19]. The following two sections present a brief overview of the underlying theoretical models.

### 2.1.1 Bound-Electron g-Factor

For a particle with charge $q$, mass $m$ and an intrinsic angular momentum (spin) $\vec{S}$, the magnetic moment $\vec{\mu}$ is given by

$$\vec{\mu} = g \frac{q}{2m} \vec{S}.$$

(2.3)

The proportionality constant $g$ is referred to as the $g$-factor. In the special case of a free electron ($q = e, \vec{S} = \frac{1}{2}\hbar$), this equation can be rewritten as

$$\vec{\mu}_S = g_e \frac{\mu_B}{\hbar} \vec{S}, \tag{2.4}$$

with the Bohr magneton

$$\mu_B = \frac{e\hbar}{2m_e}. \tag{2.5}$$

The herein introduced $g$-factor of the free electron $g_e$ can be derived from the Dirac equation (Eq. 2.1) as $g_e = 2$ [31].

In light of the advancements in QED made by Tomonaga, Schwinger and Feynman, it becomes necessary to correct this value by accounting for higher-order contributions. The first order corrections $C_2$ are represented as Feynman diagrams on the left of Fig 2.1. These corrections are based on self-energy, vacuum polarisation and vertex correction. From a mathematical perspective, they can be expressed as an expansion in the fine-structure constant $\alpha \approx 1/137$. To obtain a more precise value, it is necessary to consider these higher-order QED corrections and contributions from the hadronic and weak interactions, which result in

$$g_e = 2\left(1 + C_2[\alpha]\left(\frac{\alpha}{\pi}\right) + C_4[\alpha]\left(\frac{\alpha}{\pi}\right)^2 + C_6[\alpha]\left(\frac{\alpha}{\pi}\right)^4 + ... + a_{hadronic} + a_{weak}\right) \tag{2.6}$$

[32].

In order to experimentally measure the free-electron $g$-factor, the electron is exposed to an external magnetic field $B$. Subsequently, the electron then executes a radial motion around the magnetic field with the cyclotron frequency of

$$\omega_c = \frac{eB}{m_e}. \tag{2.7}$$

Furthermore, the magnetic moment of the electron begins to gyrate around the external field, resulting in the Larmor precession with frequency

$$\omega_L = g_e \frac{e}{2m_e} B. \tag{2.8}$$

The measurement of both the cyclotron and Larmor frequencies consequently allows the $g$-factor of the free electron to be determined [33]:

$$g_e = 2\frac{\omega_L}{\omega_C}. \tag{2.9}$$

In the case of an electron bound to a nucleus, the magnetic moment of the electron is no longer solely dependent on its spin. It is also influenced by the orbital angular momentum. In this particular instance, it is referred to as the Landé $g$-factor $g_J$, and the relation 2.3 can be formulated as

$$\vec{\mu}_J = g_J \frac{e}{2m} \vec{J}, \tag{2.10}$$

with the total angular momentum

$$\vec{J} = \vec{L} + \vec{S}. \tag{2.11}$$
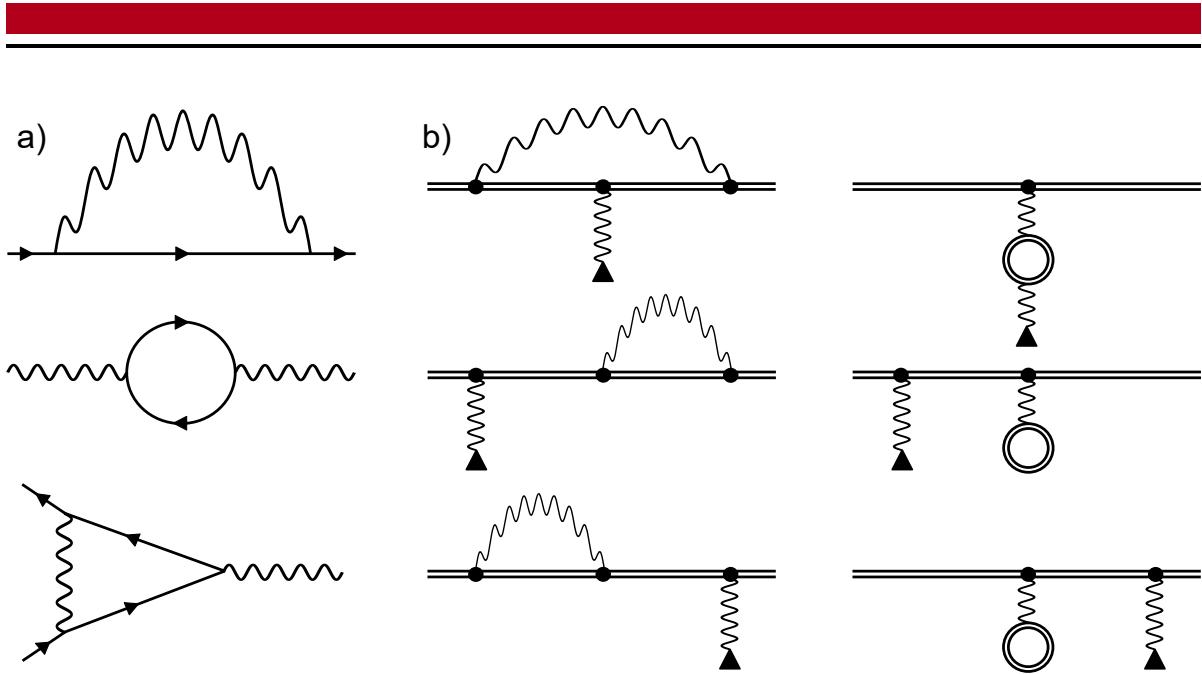
Figure 2.1: Feynman diagrams for first-order QED corrections. a) self-energy, vacuum polarisation and vertex correction for an unbound electron (top to bottom). b) self-energy (left column) and vacuum polarisation (right column) for a bound-state electron, where the bound state is indicated by the double line.

The $g$-factor can be derived once more from the Dirac equation as

$$g_J = \frac{2(1 + 2\sqrt{1 - (\alpha Z)^2})}{3}, \tag{2.12}$$

with the atomic number of the nucleus represented by $Z$ [34]. To derive Eq. 2.12, the nucleus is approximated as a point-like particle of infinite mass. Similarly, as with the corrections for the free electron, an adaptation to higher-order effects is also required for the bound electron $g$-factor.

Considering a hydrogen-like ion, the dominant contributions can be divided into QED and finite-nuclear-size effects. On the QED side, the requisite correction is once more obtained from the Feynman diagrams for self-energy and vacuum polarisation, as illustrated on the right-hand side of Fig. 2.1. The finite nucleus is represented in considerations $a_{nuc}$ of the nuclear size, structure, recoil and polarisation, which are particularly relevant for the treatment of heavy nuclei [35]. The QED-based corrections can again be represented by a series expansion in $\alpha$, although now both the expansion factor and the coefficients $D_i$ scale with the atomic number $Z$ [32]:

$$g_J = 2(1 + D_2[\alpha Z]\left(\frac{\alpha Z}{\pi}\right) + D_4[\alpha Z]\left(\frac{\alpha Z}{\pi}\right)^2 + D_6[\alpha Z]\left(\frac{\alpha Z}{\pi}\right)^4 + ... + a_{nuc}). \tag{2.13}$$

This considerably complicates the theoretical calculation of the bound electron $g$-factor in comparison to its free counterpart, especially for high-$Z$ nuclei.

The measurement of the bound electron $g$-factor is feasible in a manner analogous to that employed for the free electron. In this case, the Larmor precession of the electron is observed

concurrently with the cyclotron frequency of the ion. Subsequently, the $g$-factor can be determined by employing the relation

$$g_j = 2\frac{q}{e}\frac{m_e}{m}\frac{\omega_L}{\omega_c}, \tag{2.14}$$

with the ion's charge $q$ and mass $m$ [33].

In order to extract experimental information about the contributions of the aforementioned corrections, it is necessary to ensure that the uncertainties associated with the measurement are smaller than the magnitude of the correction itself. For light ions, such as $^{28}\text{Si}^{13+}$, the achieved relative uncertainty of $< 10^{-9}$ even allows probing for third-order two-loop QED effects and the influence of the non-zero nuclear size [32]. For heavy ions on the other hand, the currently achievable relative uncertainty of $10^{-3}$ is not suitable for effectively testing theoretical predictions, which themselves exhibit a precision on the level of $< 10^{-6}$.

The current values of the bound-electron g-factor in hydrogen-like ions are extracted by observing the lifetime of an excited state for ions stored in a storage ring, a method that is subject to relatively large uncertainties [8]. It is anticipated that greater experimental precision will be achieved through the utilisation of frequency-sensitive techniques within a Penning trap, as employed for lighter isotopes. This represents the objective of the ARTEMIS project, situated at the HITRAP facility [19].

### 2.1.2 Ground-State Hyperfine Splitting

The concept of utilising emission spectra as a distinctive fingerprint for materials was already born in the early 19th century. A theoretical explanation for the distinct observed lines was first provided by Niels Bohr approximately a century later with the introduction of his atomic model. According to this model, the emission lines originate from electrons that undergo transitions between discrete levels of binding energy, thereby emitting photons at a wavelength that corresponds to the energy difference between the involved states. These states are associated with certain radial orbits $n$, wherein the orbit with the highest energy is the closest to the nucleus [36]. The binding energy of each orbit can be calculated by employing the equation

$$E_n = -E_{Ryd}\left(\frac{Z}{n}\right)^2, \tag{2.15}$$

with the Rydberg energy

$$E_{Ryd} = \frac{m_e e^4}{8\epsilon_0^2 h^2}. \tag{2.16}$$

In this context, $\epsilon_0$ denotes the vacuum permittivity and $h$ is the Planck constant.

A more detailed analysis of the atomic or ionic spectrum reveals minor discrepancies from the predicted values. The atomic model as described by Bohr is unable to account for these deviations, as it does not include quantum mechanical nor relativistic effects. Both theories are incorporated into the Dirac equation (Eq. 2.1) which allows for a more accurate description in comparison to Eq. 2.15.

The discrepancy can be attributed to a multitude of relativistic and quantum mechanical effects, collectively known as 'fine structure'. The most dominant factors are the relativistic motion of the electron around the nucleus, the coupling of the electron's spin and orbital angular momentum, and corrections due to the quantum mechanical wave character and therefrom stemming

uncertainties in the position of the electron. In the case of the ground state with n = 1, the fine structure results in a small shift in the binding energy. Additionally, for higher levels, a splitting in multiple levels is observed [25].

In order to achieve an even higher level of precision in the theoretical prediction, it is necessary to overcome the limitations of the Dirac equation once more. As with the preceding section on the electron $g$-factor, the advancement of QED offers a solution. The effects of self-energy and vacuum polarisation, as illustrated in the Feynman diagrams of Fig. 2.1, are the dominant contributors to the observed shift in the binding energy of the electron. This so-called 'Lamb shift' exerts the greatest influence for ground-state electrons [37].

The following discussion will present an effect that is even smaller than those discussed above and is induced by the coupling of the nucleus' and electron's magnetic moments: the hyperfine splitting. Analogous to the relation between the magnetic moment and spin of the electron, also the nuclear magnetic moment can be defined as

$$\vec{\mu}_I = g_I \frac{e}{2m_p} \vec{I},\tag{2.17}$$

with the $g$-factor and spin of the nucleus $g_I$ and $\vec{I}$ and proton mass $m_p$. The ground-state spin, and consequently the magnetic moment, of the nucleus is only non-zero for uneven $Z$ or neutron number $N$. In the case of even $Z$ and $N$, each nucleon is paired with a nucleon of counter-orientated spin, which effectively results in a total nuclear spin of zero.

For a non-zero nuclear spin, the magnetic moment of the nucleus couples with the magnetic moment of the electron, yielding a total angular momentum of

$$\vec{F} = \vec{I} + \vec{J}.\tag{2.18}$$

This results in a splitting of the electronic state into multiple states with [38]

$$|J - I| \leq F \leq J + I.\tag{2.19}$$

The energy difference for a hydrogen-like ion can be calculated using the following set of equations:

$$\triangle E = \frac{\alpha(\alpha Z)^3}{n^3} g_I \frac{m_e}{m_p} \frac{F(F+1) - I(I+1) - J(J+1)}{2J(J+1)(2l+1)} m_e c^2 [A(\alpha Z)(1-\delta)(1-\varepsilon) + \chi_{rad}],\tag{2.20}$$

$$A(\alpha Z) = \frac{n^3(2l+1)\kappa(2\kappa(\gamma + n_r) - N)}{N^4\gamma(4\gamma^2 - 1)},\tag{2.21}$$

$$\kappa = (-1)^{j+l+1/2}(j+1/2),\tag{2.22}$$

$$\gamma = \sqrt{\kappa - (\alpha Z)^2},\tag{2.23}$$

$$N = \sqrt{n_r^2 + 2n_r\gamma + \kappa^2},\tag{2.24}$$

$$n_r = n - |\kappa|.\tag{2.25}$$

In this context, $n_r$ denotes the radial quantum number. $A(\alpha Z)$ accounts for relativistic effects, while parameter $\delta$ represents corrections for the nuclear charge distribution and $\varepsilon$ the Bohr-Weißkopf effect. The radiative correction is incorporated into the factor $\chi_{rad}$ [39].

As the energy splitting scales with $(Z/n)^3$, it becomes especially pronounced for ground-state (n = 1) electrons in heavy (high-$Z$) ions, making the splitting an accessible observable via laser spectroscopy. To illustrate, the splitting in the case of hydrogen-like bismuth is equivalent to a laser wavelength of 243 nm, compared to 21 cm in the case of a hydrogen atom [30].

As previously stated in the introduction to this section, the theoretically calculated correction $\varepsilon$ for the nuclear magnetisation distribution, the Bohr-Weißkopf effect, comes with a considerable degree of uncertainty. This uncertainty is for heavy nuclei of higher magnitude than the anticipated QED contributions. To circumvent this limitation, the so-called specific difference between the ground-state hyperfine splitting of the same isotope in hydrogen-like and lithium-like configurations can be measured. The specific difference is defined as

$$\triangle' E = \triangle E^{(2s)} - \xi \triangle E^{(1s)}, \tag{2.26}$$

with a parameter $\xi$, which significantly reduces the influence of the Bohr-Weißkopf effect, if selected appropriately, thereby providing access to QED contributions [5].

This measurement principle is currently employed in a series of storage-ring experiments at GSI, in which the specific difference of $^{208}$Bi and $^{209}$Bi is investigated [27, 30]. The precision of the most recent results is primarily limited by the knowledge of the ions' velocity in the storage ring and the therefrom resulting Doppler shift. However, if performed in a Penning trap, this contribution to the uncertainty can be significantly reduced, allowing for an even more stringent test of QED effects on ground-state hyperfine splitting in extreme fields. Such an experiment is planned for the SPECTRAP project at the HITRAP facility [17].

## 2.2 Ion Storage

There are several different ways to capture ions within a confined space and even more applications that benefit from the storage of these ions. Accelerators use a special form of storage rings, namely cyclotrons, to confine ions on a circular or elliptical trajectory, continuously accelerating them on each revolution. Prominent examples of these accelerator rings include the Large Hadron Collider (LHC) at CERN or the heavy ion cyclotrons SIS18 and SIS100 at GSI and FAIR [40–42].

While these rings, in particular those at GSI and FAIR, are primarily utilised for acceleration, there are also storage rings, which permit the storage of ions for extended periods of time while experiments are conducted. Depending on the ion energy, the ions can be stored at GSI in the Experimental Storage Ring (ESR), CRYRING@ESR or, after the completion of FAIR, in the High Energy Storage Ring (HESR) [43–45]. In these rings, a wide variety of experiments on stable and exotic ions are possible, including laser spectroscopy, dielectronic recombination or mass measurements [46–48].

In comparison to single-pass experiments, storage rings offer the advantage that experiments can be conducted on the ions on each turn thereby greatly increasing the statistical reliability of the measurement. Furthermore, they permit the study of observables for a wide range of ion energies. For example the Lorentz boost in the ESR ($\gamma \leq 1.4$) renders laser spectroscopy a suitable tool for probing the optical clock transition in a thorium-229 nucleus. As the transition energy of approximately 8.3 eV (corresponding to $\lambda = 149$ nm) [49] renders a considerable challenge for currently available laser systems, such experiments are facilitated with ions at high

kinetic energies.

While some experiments profit from this Lorentz boost, other experiments would benefit from slower ions or even ions at rest, as indicated in the previous sections. This energy range can be accessed by low-energy storage rings such as CRYRING@ESR or in ion traps for superior precision. There are two main types of ion traps: the Paul trap and the Penning trap. Paul traps use a combination of static and radio frequency electric fields to confine ions. They are commonly used for high-precision experiments, optical clocks or in quantum computers [50, 51]. As a significant part of this work has been conducted using a Penning trap setup, this concept will be discussed in more detail in the following sections.

### 2.2.1 Penning Trap

In 1936 Frans Penning laid the foundations for the development of the Penning trap. The results of his work on electrons in magnetic fields led to the development of the first Penning trap in 1959 by Hans Georg Dehmelt who was later awarded the Nobel Prize for his work. Dehmelt demonstrated that charged particles could be trapped using perpendicular magnetic and electric fields [52, 53]. This, at this time, so-called magnetron trap, which was later named Penning trap after Frans Penning, achieves axial confinement by two electrostatic potentials and radial confinement by a magnetic field. These traps are most commonly used in high-precision setups for laser spectroscopy or measurements of mass, g-factor and magnetic moments [17, 54, 55]. In comparison to storage rings, experiments conducted in a Penning trap can achieve a significantly higher degree of precision. For instance, the most precise mass measurements of $^{208}$Pb were performed in the Pentatrap Penning trap [56]. Similarly, the recently measured hyperfine transition in H-like $^{209}$Bi is expected to be improved by several orders of magnitude when repeated in the SPECTRAP@HITRAP experiment [12, 30]. Other applications of Penning traps include ion accumulation and cooling, as used at the ISOLTRAP setup at CERN [57]. While high-precision trap setups often work with small ensembles down to single ions, setups such as the HITRAP Cooling Trap, which is a crucial part of this work, are designed to capture large numbers of ions simultaneously.

The following sections will commence with a theoretical description of an idealised Penning trap design and the motions of the stored charged particles, followed by a theoretical treatment of realistic trap designs and their differences.

### 2.2.2 Particle Motion in a Penning trap

A theoretical approach to Penning traps necessitates an understanding of the forces acting on charged particles in electric $\vec{E}$ and magnetic $\vec{B}$ fields. The Lorentz force

$$\vec{F}_L = q(\vec{v} \times \vec{B} - \nabla\Phi), \tag{2.27}$$

named after Hendrik Antoon Lorentz, can be employed to describe such a particle with charge $q$ and velocity $\vec{v}$. The ideal Penning trap is of a hyperbolic geometry, as illustrated in Fig. 2.2, and consists of three electrodes that generate a quadrupole electrostatic potential $\Phi$. In cylindrical coordinates, $\rho$ and $z$, this geometry would result in a harmonic potential of the form

$$\Phi(\rho, z) = \frac{U_0}{4d^2}(A\rho^2 + Bz^2). \tag{2.28}$$
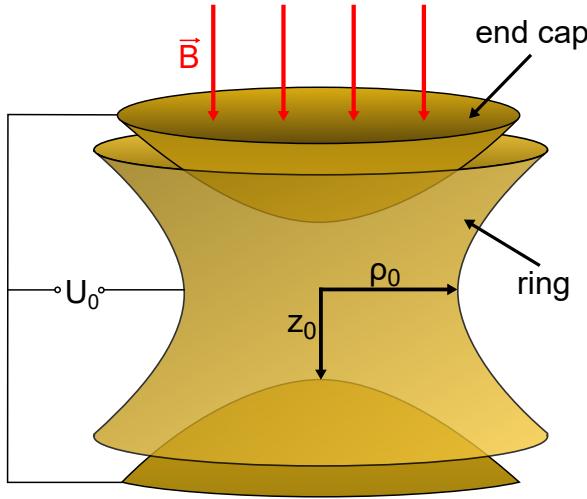
Figure 2.2: Schematic of a hyperbolic Penning trap with dimensions $z_0$ and $\rho_0$. The direction of the magnetic field is indicated in red.

$U_0$ is the potential difference between the hyperbolic end caps and the ring electrodes, and $d$ is the trap parameter, given by

$$d = \sqrt{\frac{1}{2}\left(z_0^2 + \frac{1}{2}\rho_0^2\right)}. \tag{2.29}$$

The parameters $A$ and $B$ are arbitrary factors that must satisfy the Laplace equation

$$\triangle \Phi = -\nabla \cdot \vec{E} = 0, \tag{2.30}$$

leading to the relation [58]

$$2A + B = 0. \tag{2.31}$$

According to Earnshaw's theorem [59], one of these parameters must be negative, otherwise the solution would not correspond to a minimum potential but to a saddle point. This directly implies that an ion trap consisting only of electrostatic potentials is not possible, hence leaving only alternating electric potentials, as used in a Paul trap, or a combination of the static electric field with a static magnetic field must be employed.

A possible solution to Eq. 2.31 is the pair $A = -1$ and $B = 2$, resulting in a quadrupole potential of

$$\Phi = \frac{U_0}{4d^2}(-\rho^2 + 2z^2). \tag{2.32}$$

This potential is capable of confining charged particles in the direction of $z$, but is radially unstable. This is compensated for by a perpendicular magnetic field. Combining Eq. 2.27 with Newton's second law of motion

$$\vec{F} = m\frac{\mathrm{d}^2}{\mathrm{d}t^2}\vec{x} \tag{2.33}$$

gives the following differential equations:

$$\frac{\mathrm{d}^2}{\mathrm{d}t^2}\vec{z} + \frac{qU_0}{md^2}\vec{z} = 0$$

$$\frac{\mathrm{d}^2}{\mathrm{d}t^2}\vec{\rho} - \frac{q}{m}\vec{B} \times \frac{\mathrm{d}}{\mathrm{d}t}\vec{\rho} - \frac{qU_0}{2md^2}\vec{\rho} = 0 \tag{2.34}$$
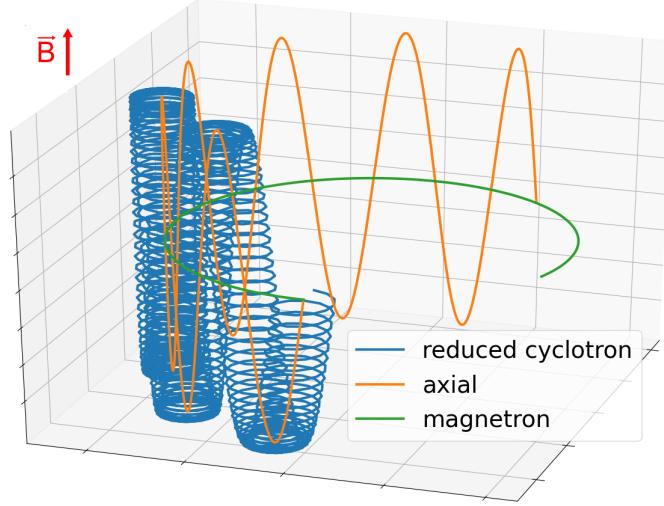
Figure 2.3: Illustration of the three modes of motion a particle executes when confined within a Penning trap. The direction of the magnetic field is indicated in red. Amplitudes and frequencies of the motions are chosen to improve clarity and can significantly differ in a real setup.

These differential equations can be solved analytically and result in particle motion as shown in Fig. 2.3 with three different modes of motion. The axial motion is independent of the magnetic field and its frequency $\omega_z$ is given by

$$\omega_z = \sqrt{\frac{qU_0}{md^2}}. \tag{2.35}$$

The overlapping magnetic and electric fields give rise to the slow magnetron drift around the symmetry axis and the fast reduced cyclotron motion. Their respective frequencies $\omega_-$ and $\omega_+$ are given by

$$\omega_\pm = \frac{1}{2}(\omega_c \pm \sqrt{\omega_c^2 - 2\omega_z^2}), \tag{2.36}$$

with the unperturbed cyclotron frequency

$$\omega_c = \frac{qB}{m}. \tag{2.37}$$

From equations 2.35 and 2.36, the stability criteria for charged particles stored in a Penning trap can be derived as

$$0 \le qU_0$$
$$\omega_z \le \frac{\omega_c}{\sqrt{2}}. \tag{2.38}$$

The first condition states that the polarity of the particle's charge and the confining electric potential must be equal. Rewriting the second condition as

$$\frac{q}{m} \le \frac{d^2B^2}{2U_0} \tag{2.39}$$
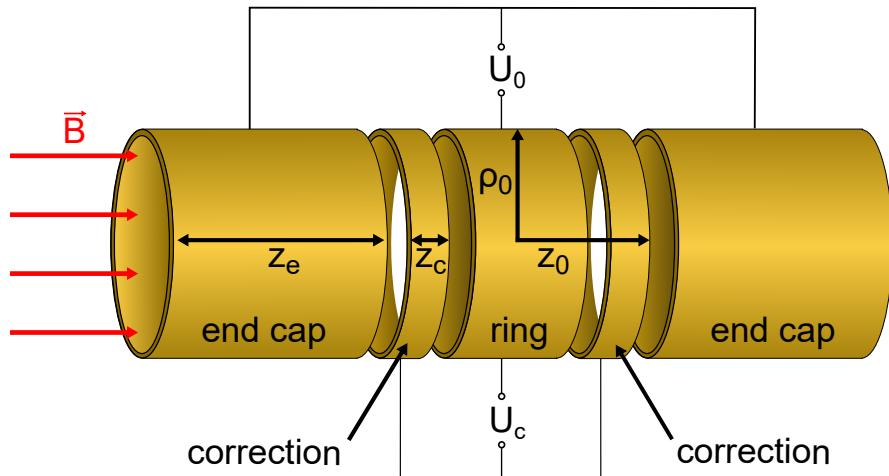
Figure 2.4: Schematic of an electrically compensated cylindrical Penning trap with dimensions $z_0$ and $\rho_0$. The direction of the magnetic field is indicated in red.

allows for estimation of the maximum charge-to-mass ratio that can be stored in a Penning trap for given confining-field values. Typically, magnetic and electric fields are chosen in a way that the relation

$$\omega_- \ll \omega_z \ll \omega_+ \tag{2.40}$$

is satisfied [58, 60].

All the equations and relations introduced above are based on the assumption of a harmonic electric potential. In theory, such a potential can be achieved most effectively by a hyperbolic trap design, as depicted in Fig. 2.2. However, in reality, this design has several disadvantages and limitations. It is challenging, although possible, to produce the hyperbolic electrodes mechanically. These traps must also be of a closed form which makes them difficult to access for both ion injection and measurement devices. Furthermore, the trapping volume is relatively small, which limits the number of particles that can be trapped. To address these challenges, most setups employ cylindrical Penning traps. These so-called Penning-Malmberg traps will be discussed in more detail in the following section.

### 2.2.3 Penning-Malmberg Trap

The more popular alternative to the hyperbolic design is the cylindrical Penning trap as depicted in Fig. 2.4. This approach, which was created by John Holmes Malmberg and is hence known as the Penning-Malmberg trap [61], has numerous advantages over the original hyperbolic design. These traps consist only of cylindrical electrodes, which are comparatively easy to fabricate and often have open end caps that enable simpler ion injection. Furthermore, larger trapping volumes can be achieved by implementing longer electrodes, which allows for the storage of higher numbers of particles.

However, their main disadvantage to a hyperbolic design is the electric field. In general, cylindrical traps do not produce a harmonic field potential but there are ways to achieve an approximate harmonic shape. In a cylindrical Penning trap, the electric potential at the centre of the trap can be described by a multipole expansion of the electric field potential in Legendre polynomials

$P_k(\cos\theta)$ as

$$\phi(r,\theta) = \frac{1}{2}U_0 \sum_{k=0}^{\infty} C_k \left(\frac{r}{d}\right)^k P_k(\cos\theta), \qquad k \in 2\mathbb{Z}. \tag{2.41}$$

Due to the parity of the Legendre polynomials for reflection-symmetric charge distributions, the expansion coefficients $C_k$ are non-zero only for even $k$. Consequently these coefficients are given by

$$C_k = 4\frac{(-1)^{k/2}}{k!}\left(\frac{\pi}{2}\right)^{k-1}\left(\frac{d}{z_0+z_e}\right)^k \sum_{n=0}^{\infty}(2n+1)^{k-1}\frac{A_n}{J_0(k_n\rho_0)} \tag{2.42}$$

with

$$A_n = (-1)^n - \sin\left(k_n z_0\right) - \sin\left(k_n(z_0-z_c)\right) \tag{2.43}$$

and

$$k_n = \frac{(n+\frac{1}{2})\pi}{z_0+z_e}. \tag{2.44}$$

In this context, $z_e$ denotes the length of the end-cap electrodes and $J_0(k_n\rho_0)$ is the zero-order Bessel function. The constant monopole coefficient $C_0$ has no effect on the particle motion, and for a perfect harmonic potential the quadrupole coefficient $C_2 = 0$, while all higher-order coefficients $C_{k\geq 4}$ vanish.

For a real hyperbolic and in particular for cylindrical traps this is not the case. The trap can then either be compensated mechanically by choosing the appropriate ratio between the trap radius $r_0$ and length $z_0$ or electrically by inserting additional correction electrodes of length $z_c$ (see Fig. 2.4). This can result in vanishing sextupole and octupole coefficients $C_4$ and $C_6$. Higher-order multipoles can be neglected as their impact decreases with $(r/d)^k$. Although theory allows for the realization of harmonic potentials in mechanically compensated cylindrical traps, in practice this is not achievable, even for hyperbolic traps. It is inevitable that there will be some deviation from a perfect harmonic potential due to margins of error in the manufacturing process and the finite size of the electrodes. Nevertheless, high-precision experiments are possible by combining mechanical and electrical compensation [62, 63].

While most precision experiments work with particle numbers down to single particles, cylindrical Penning traps also find application in the storage of high numbers of particles. Typical examples are accumulation traps or non-neutral plasma experiments [57, 64]. Increasing the amount of stored charges will also inevitably lead to space-charge effects that will alter the behaviour of the trapped particles and introduce constraints that must be considered. This will be discussed in more detail in the following Sec. 2.2.4. To some extent, these space-charge effects can be counteracted by reducing the particle density, i.e., increasing the trap volume. This is usually achieved by installing longer and/or more trap electrodes. To maintain a harmonic electric potential, the electrode radius must also be increased for effective mechanical compensation.

An alternative approach is to extend the electrodes without increasing their radii at the expense of a harmonic field potential. At this point, the frequencies of the eigenmotions gain an energy dependence from the no longer vanishing $C_4$ octupole coefficient, leading to a shift in frequency.
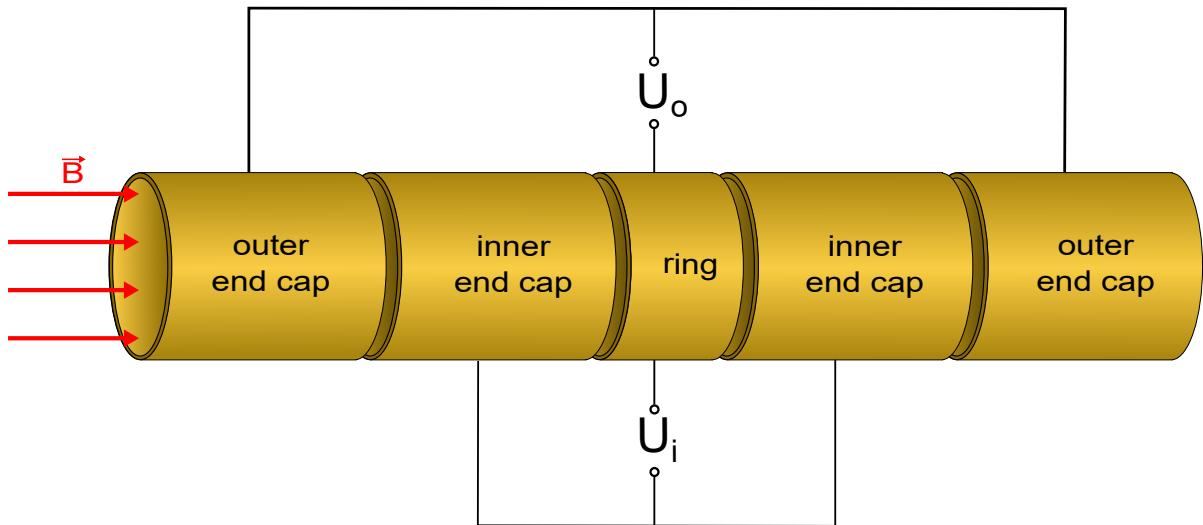
Figure 2.5: Schematic of a cylindrical Penning, which allows for the formation of a nested trap potential and thereby the storage of multiple particle clouds with different polarities. This is achieved by selecting appropriate potentials for the outer and inner end caps, $U_o$ and $U_i$, respectively.

The relative shift for each motions $\triangle\omega_i/\omega_i$ is given by

$$
\begin{aligned}
\frac{\triangle\omega_z}{\omega_z} &= \frac{C_4}{C_2}\frac{1}{qU_0}\left[\frac{3}{2}E_z - 3\left(\frac{\omega_z}{\omega_+}\right)^2 E_+ + 6E_-\right] \\
\frac{\triangle\omega_+}{\omega_+} &= \frac{C_4}{C_2}\frac{1}{qU_0}\left(\frac{\omega_z}{\omega_+}\right)^2\left[-3E_z + \frac{3}{2}\left(\frac{\omega_z}{\omega_+}\right)^2 E_+ - 6E_-\right] \\
\frac{\triangle\omega_-}{\omega_-} &= \frac{C_4}{C_2}\frac{1}{qU_0}\left[6E_z - 6\left(\frac{\omega_z}{\omega_+}\right)^2 E_+ + 6E_-\right].
\end{aligned}
\tag{2.45}
$$

These equations also show that the eigenmotions can no longer be considered independent as also the frequency $\omega_i$ of other motions influences the resulting frequency [60]. Consequently, such trap designs are frequently employed in accumulation or cooling traps, where a precise quadrupole field is not essential as they are not designed for precision experiments.

The implementation of multiple additional electrodes, as illustrated in Fig. 2.5, also enables the storage of multiple clouds of particles or even the simultaneous storage of particles of opposite polarities. For instance, positively charged ions can be stored together with electrons in overlapping volumes. This particular technique is commonly employed for electron cooling which will be discussed in more detail in Sec. 2.3.6.
Figure 2.6 schematically illustrates the potential distribution in such a so-called nested trap. It should be noted that the resulting electric field, particularly for the stored ions, can no longer be assumed to be harmonic. Depending on the exact electrode configuration and applied potentials, there are even regions with constant electric fields, resulting in 'bathtub'-like confinement potentials. In any case, the above introduced theoretical discussion is no longer valid and can at best provide a very rough estimate of the actual particle motions.
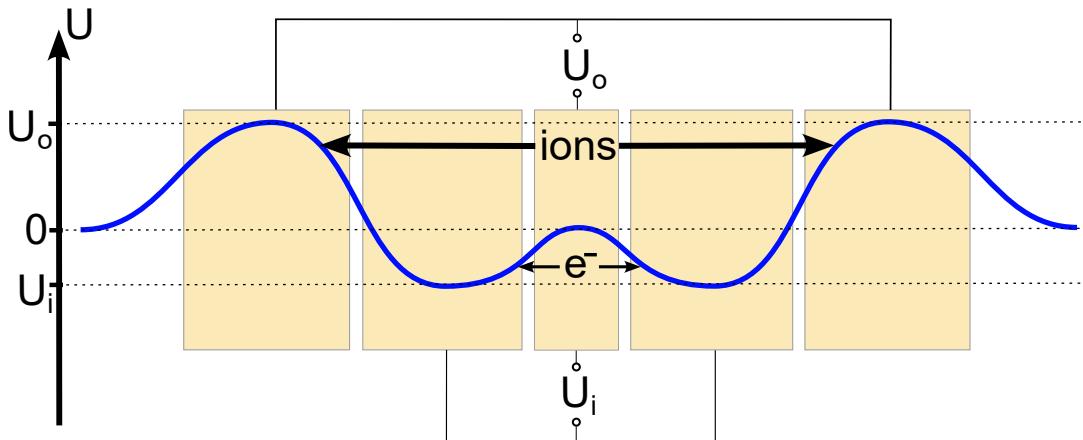
Figure 2.6: Visualisation of the electric potential, formed by a cylindrical Penning trap, that allows for the simultaneous storage of positively charged ions and electrons. The outer and inner end-cap electrodes are biased by potentials $U_o$ and $U_i$, respectively. Electrons are then trapped by the negative potential applied to the inner end-cap electrodes, while positive potentials at the outer end-cap electrode confine the ion cloud.

### 2.2.4 Space-Charge Effects

In particular, for the storage of a non-neutral plasma, additional effects come into play that influence the given electric potential. The cloud of charged particles itself produces a space-charge potential, which changes the effective electric potential experienced by a test charge. This results in the following corrections for the oscillation frequencies for all given modes of motion

$$
\begin{aligned}
\omega_z' &= \sqrt{\omega_z^2 - \frac{1}{3}\omega_p^2} \\
\omega_\pm' &= \frac{1}{2}(\omega_c \pm \sqrt{\omega_c^2 - 2\omega_z^2 - \frac{4}{3}\omega_p^2},
\end{aligned}
\tag{2.46}
$$

with the plasma frequency

$$
\omega_p = \sqrt{\frac{q^2 n}{\epsilon_0 m}}.
\tag{2.47}
$$

Assuming real oscillation frequencies in equations 2.46, yields the conditions for the particle density $n$

$$
n \leq \frac{3\epsilon_0 U}{q d^2}
\tag{2.48}
$$

and

$$
n \leq \frac{3}{4}\frac{\epsilon_0 B^2}{m} - \frac{3}{2}\frac{\epsilon_0 U}{q d^2}
\tag{2.49}
$$

respectively. The combination of both conditions results in the so-called Brillouin limit

$$
n_{\text{Brillouin}} = \frac{\epsilon_0 B^2}{2m},
\tag{2.50}
$$

which is the highest particle density theoretically achievable in a Penning trap. Although the Brillouin limit fulfils the aforementioned stability conditions, operating a Penning trap close to that limit will result in significant losses of the stored particles [60].

In addition to changing the particle motions, working with a high-density plasma will also strongly influence the required capture potential. The on-axis space-charge potential for a cylindrical, evenly distributed electron cloud can be described by

$$\Phi = \frac{eN}{4\pi\epsilon_0 l_p} \left( 1 + 2\ln\left(\frac{r_t}{r_p}\right) \right), \tag{2.51}$$

with the number of stored electrons $N$, plasma length and radius $l_p$ and $r_p$ and the trap radius $r_t$ [65]. This can be assumed as a valid model, especially for the above-introduced 'bathtub'-like trap configurations. For proper confinement of such a particle cloud, the capture potentials must obviously be higher than the produced space-charge potential.

### 2.2.5 Detection of Stored Particles

Two fundamentally different approaches can be employed to gain information about the particles stored in a Penning trap. After the storage process the particles can be detected by a destructive detection method such as Faraday cups or microchannel plate detectors. This form of detection is relatively easy to implement and is also widely used at the HITRAP facility [66]. An overview of the variety of destructive detectors employed at HITRAP will be given in Sec. 3.2.8.

While these detectors cover a wide range of applications, the detected particles are 'destroyed' during the measurement. This trait prevents the observation of dynamic processes that take place during the storage in a storage ring or trap setup. Hence, for observing stored particles, non-destructive detection methods are needed. Most commonly, these methods are based on so-called 'image' charges induced by moving charged particles.

When a charged particle comes into proximity with a conductor, it induces a shift of the conductor's charge carriers, forming a charge distribution that mirrors the charged particle. As the particle moves close to the conductor, so does the induced image charge inside, resulting in an image current. This effect was first postulated by William Shockley [67] and Simon Ramo [68] leading to the Shockley-Ramo theorem.

By measuring this current, information about the particle can be extracted. In its most basic form, such a detector consists solely of a hollow metal tube that is capacitively coupled to an amplifier (see Fig. 2.7). When a bunch of charged particles enters the tube, the image currents cause a rise in the measured voltage, which drops again when the particles leave the tube (or vice versa for opposite charges). The measured signal is given by

$$U(t) = \frac{QG(t)}{\alpha C} \tag{2.52}$$

with the amplification factor $\alpha$ and capacitance $C$. The term $G(t)$ describes the time-dependent relation between the total charge of passing particles $Q$ and the charge induced in the conductor. The measured signal thus includes information about the longitudinal shape and total charge of the particle bunch [60, 69]. Combining two spatially separated cylinders also allows for extracting the kinetic energy, which is achieved by analysing the phase shift of the measured signals in a manner analogous to that employed in phase probe detectors [70].
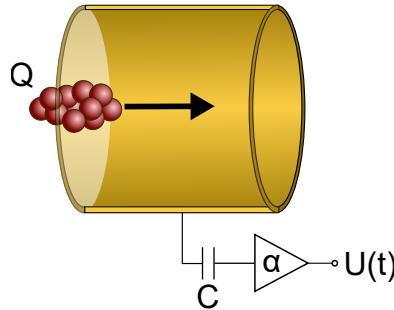
Figure 2.7: Schematic visualisation of a setup for the non-destructive detection of a moving particle ensemble with charge Q, whereby the induced potential change $U(t)$ in a hollow cylinder is measured.

Non-destructive detection methods are also a popular tool for Penning trap setups, especially for observing the reduced cyclotron frequency. Instead of measuring the signal induced by charged particles passing through an electrode, the radial motion inside the electrode is detected. Prerequisite for this is a radially segmented electrode with a minimum of two segments. Observing the induced signal on one electrode segment results in a periodic progression with the frequency of the corresponding motions motion [71]. A differential measurement of the induced signal on two opposite electrodes, will enhance the measurement sensitivity as the detected signal is amplified. In this case, the current induced by a particle with charge q can be described as

$$I(t) = \omega_+ \frac{q}{D_+} \rho_+(t) \tag{2.53}$$

with the frequency $\omega_+$ and amplitude $\rho_+(t)$ of the reduced cyclotron motion. The model parameter $D_\pm$ denotes the effective distance of the electrode segments and adjusts for the deviation from the theoretical model of two infinitely wide parallel electrodes [72, 73].

As the induced signal typically is too small for direct measurement, further amplification is required. One approach employs resonant excitation, whereby the eigenmotion is excited by applying a radio-frequency signal at the corresponding frequency to the segmented electrode. This transfers energy into this motion and, in the case of cyclotron motion, increases its radius [74]. For ensembles of multiple particles, resonant excitation also ensures that all particles oscillate in phase. As the phase of the radial motion is determined during the injection and distributed statistically over the whole phase space, the induced signal of two particles with a 180° phase shift is cancelled. For a large ensemble, this leaves only a small fraction to contribute to the measurable signal. Resonant excitation externally determines the phase of all particles, thus increasing the induced signal [75].

For detecting single ions, the more efficient approach is an external resonant circuit. Such a circuit consists in its most basic form of an inductance $L$ and capacitance $C$ and has a resonant frequency of

$$\omega_{LC} = \frac{1}{\sqrt{LC}}. \tag{2.54}$$

When in resonance with an eigenmotion the measured signal is given by

$$U(t) = \omega_{LC} q L I(t) \tag{2.55}$$

with the image current $I(t)$ introduced in Eq. 2.53 [76].

The radial frequencies of stored particles can be used to determine properties including their charge, mass and lifetime. While these motions are generally independent of the kinetic energy for setups with a harmonic potential, this is no longer the case for long setups with regions of constant electrostatic potentials. In these cases, the measured frequencies of the eigenmotions may also provide access to the kinetic energy of the stored particles [58].

### 2.2.6 Loss of Stored Particles

When discussing the loss of stored particles, it is necessary to differentiate between two distinct categories of loss processes: the particle actually leaving the trap volume and the particle undergoing a change in charge state or composition. While the latter does not necessarily result in a loss of the particle itself, in the majority of cases it becomes irrelevant, as experiments often require a specific particle in a certain charge state. In order to facilitate the following discussion, the particle will be considered lost for processes of both categories.

The first prerequisite for a stable storage over an extended period of time is a well-aligned setup, namely perpendicular magnetic and electric fields. Should this condition not be sufficiently well fulfilled, stored particles may enter unstable trajectories that possibly lead to magnetic reflection, are not suited for subsequent ejection or exhibit high radii in the magnetron motion, which may cause collision with the trap electrodes. Furthermore, for a charged plasma misalignment can also result in heating and subsequent particle loss [65, 77].

The given trap settings, i.e., magnetic field and trap potential play also an important role in the stability of the trapping conditions. Firstly, the condition stated in Eq. 2.39 must be fulfilled and ideally the trap potential should be such that the right-hand side of the condition is significantly greater than the left-hand side [60]. Furthermore, the frequencies of the modes of motion in a Penning trap must not be an integer multiple of one another. This condition is represented by the equation

$$N_+ \omega_+ + N_- \omega_- + N_z \omega_z \neq 0, \qquad N_i \in \mathbb{Z}. \tag{2.56}$$

With at least two frequencies in resonance, the confinement of the particles becomes unstable [78]. Any imperfections or instabilities in the electric or magnetic fields will further enhance this form of particle loss, as the resulting variations in motion frequencies increase the chance of fulfilling the condition from Eq. 2.56 at some point during the storage.

Neglecting possible inaccuracies in the setup, there are nevertheless processes that may potentially lead to particle loss. If the energy in the magnetron motion of a stored particle is reduced, the increasing magnetron radius may eventually exceed the available trap volume. In addition to active cooling methods such as resistive or electron cooling, this phenomenon, which is also known as magnetron loss, can be caused by passive cooling techniques such as cyclotron cooling of light particles (for further details, see Sec. 2.3.2).

Alternatively, it can be attributed to interactions with residual gas atoms. Elastic scattering with residual gas atoms can transfer energy from the magnetron motion, thereby increasing its radius $r_-(t)$. The time dependent magnetron radius can be expressed as a function of the initial radius $r_-(t_0)$ at time $t = 0$,

$$r_-(t) = r_-(t_0) \, e^{\gamma \frac{\omega_-}{\omega_+ - \omega_-} t}, \tag{2.57}$$

where $\gamma$ denotes the rate of energy loss. This rate is given by

$$\gamma = \frac{q}{mK_0} \frac{pT_0}{p_0 T} \tag{2.58}$$

with the reduced particle mobility $K_0$, normal pressure $p_0$ and normal temperature $T_0$ [79].
In addition to magnetron loss, elastic scattering with residual gas can also cause particle loss due to resulting unstable trajectories. Both loss mechanisms can be suppressed by improving the vacuum conditions as the probability of particle loss caused by these mechanisms scales with $\frac{1}{p}$.

It is particularly relevant to consider charge-changing loss processes in the context of highly charged ions. Recombination of charged ions or molecules with free electrons becomes only significant when electrons are trapped simultaneously, as it is the case during electron cooling of ions. The relevant electron recombination processes are subsequently discussed in the corresponding Sec. 2.3.6.
For solely trapped highly charged ions, the dominant loss mechanism is charge exchange with residual gas. During this process, a trapped ion captures one or multiple electrons from residual gas atoms, thereby transferring to a lower charge state. Depending on the trapping conditions the ion may remain confined, but is, as stated above, no longer of interest and considered lost. The semi-empirical Müller–Salzborn equation

$$\sigma_{q,q-k} = A_k \, q^{\alpha_k} I^{\beta_k} \left[ \text{cm}^2 \right] \tag{2.59}$$

can be used to calculate the cross-section $\sigma_{q,q-k}$ of $k$-fold charge exchange between charged ions with charge state $q$ and atoms or molecules with an ionization energy $I$ in eV. The empirically derived coefficients $\alpha_k$ and $\beta_k$ can be taken from [80]. In a cryogenic setup with ultra-high vacuum conditions, the residual gas is dominated by molecular hydrogen with an ionisation energy of 15.43 eV [81, 82].
From the cross-section for charge exchange, the lifetime of a certain charge state inside a Penning trap can be derived from

$$\tau = \frac{k_B T}{\sigma p v}, \tag{2.60}$$

with the Boltzmann constant $k_B$, trap temperature $T$, pressure $p$ and ion velocity $v$. Provided a stable and well adjusted setup, the lifetime of highly charged ions in a Penning trap is predominantly determined by the lifetime of a certain charge state.

## 2.3  Cooling Mechanisms of Charged Particles

In experiments involving stored charged particles, the precision of the measurement is often limited by the particle energy, particularly in relation to the accuracy of the energy and its distribution. For instance, atomic clock or g-factor measurements require the use of ultra-cold ions in the sub-eV regime in order to achieve the highest precision [83, 84]. Other experiments, such as the laser spectroscopic measurements of the transition energies in ions strongly depend on the Doppler shift caused by the ion motion relative to the laser beam [85]. In this case, not only a precisely known mean kinetic energy is required but also a narrow energy distribution. Not merely an experiments precision is limited by the kinetic energy of a particle, but also the

transport of the particle beam. In this case, again the energy distribution is of importance, as is the emittance of the particle beam. Effective transport with respect to loss of particles is only possible for a narrow energy distribution and a low emittance. In Sec. 2.3.1, the quantification of a beam's quality is discussed with respect to beam properties such as emittance and energy distribution.

The reduction of the emittance, the mean kinetic energy and its energy width can be achieved using various cooling techniques, which will also result in an improved beam quality for subsequent transport. The choice of the most suitable cooling mechanism is contingent upon the specific application, the initial energy, beam properties and the prevailing setup conditions. This section will subsequently delve into a detailed examination of a selection of available techniques.

## 2.3.1 Beam Quality

The quality of a particle beam can be described in terms of two key properties: the emittance and the energy distribution. An ideal beam would comprise particles with an identical trajectory and kinetic energy. In this physically impossible case, both the emittance and the width of the energy distribution would be zero.

However, a real particle beam will also exhibit non-zero transversal components of motion, which require the use of focusing elements in a beam line. The transverse motion in one direction can be quantified by the beam's emittance $\epsilon_x$ of the beam, which is given by

$$\epsilon_x = \frac{1}{\pi} \int \int \mathrm{d}x \, \mathrm{d}\sin\theta_x, \tag{2.61}$$

with the distance of a particle from the ideal position $x$ and its angle to the ideal trajectory $\theta_x$. In the case of a parallel beam, the emittance is equal to zero, as the angle of each particle with respect to the beam's longitudinal motion is also zero.

An increase in beam emittance results also in a more complicated transportation through a beam line. The maximum admissible emittance is determined by the focusing elements employed in the beam line, as a higher value requires stronger focusing and, consequently, a reduction in the distance between the elements. In accordance with Liouville's theorem, the emittance of a beam represents a conserved property within a conservative system. Therefore, the beam quality with respect to the emittance cannot be enhanced by focusing elements and requires cooling of the beam.

Furthermore, the width of the energy distribution of a particle beam, strongly influences the transport efficiency through a beam line. As it describes the deviation of the longitudinal velocity of a particle from the reference particle, the energy width is often also referred to as longitudinal emittance. The focal length of beam-guiding elements depends on the energy of a charged particle, which ultimately leads to different trajectories in the beam line for different energies. Eventually, this will result in unstable trajectories and subsequent particle loss. As the width of the energy distribution also cannot be reduced by conventional beam line elements, cooling of the beam is imperative for an effective transport [86].

## 2.3.2 Cyclotron Cooling

For light particles, such as electrons or positrons, trapped in a Penning trap, cyclotron cooling is the most straightforward method to employ, as it is a passive effect. A charged particle in

the presence of a magnetic field performs a circular motion due to the Lorentz force. The exact form and origin of this motion are discussed in detail in Sec. 2.2.2. Due to their radial drift, the particles are constantly accelerated perpendicular to the direction of motion. This results in a constant emission of energy in the form of bremsstrahlung, which in turn decelerates the particle in this direction of motion [87].

In a Penning trap, this phenomenon is observed for both the magnetron and the reduced cyclotron motion. However, as the dissipated energy is proportional to the square of the angular frequency and $\omega_+$ is several orders of magnitude higher than $\omega_-$, the magnetron motion can be neglected. The time-dependent energy $E(t)$ of a particle with charge $q$ in a magnetic field can be modelled by the equation

$$E(t) = E_0 \, e^{-t/\tau}, \tag{2.62}$$

where $E_0$ is the initial energy at $t = 0$. The cooling constant $\tau$ depends on the mass $m$, charge $q$ and unperturbed cyclotron frequency $\omega_c$ of the particle and is given by

$$\tau = 3\pi\epsilon_0 \frac{mc^3}{q^2\omega_c^2} = 3\pi\epsilon_0 \frac{m^3c^3}{q^4B^2} \tag{2.63}$$

[58]. As the cooling constant is proportional to the cube of the mass it becomes evident that this cooling mechanism is only suitable for very light particles. While an electron is cooled down to $1/e$ of its initial energy within 72 ms in a 6 T magnetic field, a proton would require 14 years and bare uranium 2.5 years. Consequently, different approaches to actively cool ions are therefore inevitable.

### 2.3.3 Laser-Doppler Cooling

One prominent ion-cooling technique down to the sub-eV regime is laser cooling. The stored ions are overlapped with a laser that ideally addresses a closed ground state transition with a short excited state lifetime compared to the axial frequency $\omega_z$. During the excitation of the transition, a momentum transfer in direction of the laser beam takes place. The photons produced during spontaneous relaxation on the other hand have no preferred direction, which results in a net acceleration in the direction of the laser beam. Due to the Doppler shift, a slight red-detuning of the laser frequency results in an effective deceleration for ions moving towards the laser, while ions moving in colinear direction to the laser less probably affected. Consequently, the mean kinetic energy of the ion ensemble is reduced.

Reducing the red-detuning of the laser during the cooling process will lead to a reduced ion temperature that can theoretically reach the Doppler limit, which can be in the mK-regime, depending on the electronic system [88]. Alternatively, the laser can be set to a constant frequency close to the rest-frame frequency, addressing only ions approaching the turning point at the capture electrodes. This reduces the cooling efficiency but allows for a simpler laser setup [89].

The disadvantage of this cooling method, while being both fast and efficient for systems of limited momentum distribution, is that it is only applicable for ions with a suitable optical transition. The possible applications for laser cooling are limited by the initial properties of the ions and their electronic system. Only if the ion species has a fast and closed transition that can be accessed by a sufficiently strong and narrow-banded laser system, laser cooling becomes a viable option. Unfortunately, only a limited number of ion species exhibit such a transition, and even for those

that do, the laser system must be tailored to this specific transition. In addition, the Doppler width of the ions is required to be in the order of the laser linewidth to allow for fast and efficient cooling. Consequently, laser cooling represents a valuable tool for certain applications but is not a universal method for a vast variety of ion species [89].

### 2.3.4 Resistive Cooling

The presence of charged particles in the vicinity of a conductor induces an image charge within the conductor. As the particle moves so does the image charge, leading to the generation of an image current (see Sec. 2.2.5). The utilisation of an RLC circuit to dissipate the energy in this current effectively dampens the motion of the original particle, thereby reducing its kinetic energy. The energy is dissipated in the form of thermal energy, which limits the minimal achievable temperature to that of the circuit itself. For effective resistive cooling, the resonance frequency of the RLC circuit, at which the complex impedance reaches extreme values, must be close to the motion frequency of the charged particle. In most applications, the axial frequency is chosen for resistive cooling. For a parallel RLC circuit, the quality factor, which represents the effectiveness of energy dissipation in the resistor, is given by

$$Q = \frac{R}{L\omega}.$$ (2.64)

A high value for $Q$ results in an effective and rapid cooling process. Simultaneously, a high $Q$-factor also implies a narrow bandwidth $\Delta\omega$ of the circuit as

$$\Delta\omega = \frac{\omega_0}{Q},$$ (2.65)

with the resonance frequency $\omega_0$ [90]. This implies that effective resistive cooling is only applicable to harmonic trap potentials with a narrow distribution of the motion frequencies. In inharmonic setups, where for instance the axial frequency is dependent on the energy distribution of the ion ensemble, this method becomes inefficient resulting in long cooling times. Prior cooling, for example, through sympathetic cooling, is therefore essential for hot ion ensembles to enable efficient resistive cooling.

### 2.3.5 Buffer-gas Cooling

While both cyclotron and laser-Doppler-cooling are only applicable to a limited set of particles, buffer gas cooling can be applied to a wide range of ion species. The buffer gas consists of neutral atoms that are generally lighter than the ions to be cooled. Through elastic scattering, the ions transfer their energy to the atoms, which are lost during this process. Following the cooling process, the buffer gas can be removed, as would be necessary when applied in a trap setup [91], or it can be replaced continuously, as is done in buffer gas cells for accelerator beam lines [92]. While this technique provides rapid cooling of the mean kinetic energy and its distribution and can be applied to almost all ions or molecules, it is not suitable for the cooling of HCI. The probability of charge exchange during elastic scattering increases with the ion's charge state and resulting in a non-negligible ion loss. Negligible losses can only be expected if the binding energy of the electrons in the buffer gas atoms is higher than the ionisation energy of the missing electrons in the ions. Consequently, this technique is usually employed for lowly charged ions

using a noble gas such as helium, argon or xenon as buffer, where the electrons' binding energy is comparably high.

### 2.3.6  Sympathetic Cooling

A method very similar to buffer-gas cooling is sympathetic cooling. In contrast to the buffer-gas technique, the particles of interest are captured simultaneously with another species of charged particles. Here, the energy transfer is not conducted through elastic scattering but through Coulomb interactions between the particle species. Therefore, sympathetic cooling necessitates charged particles rather than a neutral buffer-gas.

For effective application, the non-neutral plasma itself must also be cooled, as otherwise it will heat up and the equilibrium temperature will increase. Commonly employed for this purpose are either ions that are available for laser cooling, such as $Be^+$ or $Mg^+$, or electrons/positrons that are cooled via cyclotron cooling. Non-neutral plasma comprising of electrons or positrons have the advantage, that they are passively cooled by cyclotron cooling in the magnetic field of the Penning trap and do not require the setup of a laser cooling system [93].

#### Electron Cooling

In the specific case of electron/positron cooling, a cold plasma of electrons or positrons, respectively, is stored simultaneously with the ion cloud. While the use of positrons would obviously prevent recombination between ions and electrons, due to the difficulty of positron production, electron cooling provides a less challenging alternative. Therefore, the following discussions will focus on sympathetic cooling with electrons. The phenomenon of electron cooling was first observed on anti-protons in 1989 [94] and on protons in 1996 [95]. Recently, electron cooling has also been successfully applied to heavier singly charged ions [96], although cooling of highly charged ions has thus far only been discussed theoretically [97, 98].

When electrons and ions are stored simultaneously in a nested trap potential (see Sec. 2.2.3), the ions transfer energy to the electron plasma. This leads to an increase in the electron cloud temperature, which is counteracted by the cyclotron cooling of the electrons (see Sec. 2.3.2). The time derivative of the temperature $T_e$ of an electron cloud of $N_e$ electrons is given by

$$\frac{dT_e}{dt} = \frac{N_i}{N_e} \frac{1}{\tau_i} (T_i - T_e) - \frac{1}{\tau_e} (T_e - T_t), \tag{2.66}$$

with the ion number and temperature $N_i$ and $T_i$ and the temperature of the surrounding trap setup $T_t$. The cooling constant for cyclotron cooling of electrons is described in Eq. 2.63 and the corresponding value for ions cooled via electron cooling can be written as

$$\tau_i = (4\pi\epsilon_0)^2 \frac{m_i m_e}{n_e q_i^2 e^2} \frac{1}{\ln \Lambda} \left( \frac{k_B T_i}{m_i} + \frac{k_B T_e}{m_e} \right)^{3/2}. \tag{2.67}$$

Here, $m_i$ and $m_e$ denote the mass and $q_i$ and $e$ the charge of ions and electrons, respectively, while $k_B$ is the Boltzmann constant [60]. The term $\ln \Lambda$ is the Coulomb logarithm that results from integrating the energy loss per collision over the possible impact parameters. As this integral would not converge, it is necessary to choose physically reasonable limits. The Coulomb logarithm is usually defined as

$$\ln \Lambda = \ln \left( \frac{b_{\max}}{b_{\min}} \right) \tag{2.68}$$

where $b_{min}$ corresponds to the minimum impact parameter for maximum momentum transfer and $b_{max}$ is the impact parameter one Debye length from $b_{min}$. The Debye length is defined as the distance where the effective potential of a charge is reduced by a factor of $1/e$ due to electrical screening by other charges within a plasma [99, 100].

The cooling time parameter for electron cooling, $\tau_i$, defined in Eq. 2.67, allows the time derivative of the ion temperature to be calculated as

$$\frac{dT_i}{dt} = -\frac{1}{\tau_i}(T_i - T_e). \tag{2.69}$$

This, in conjunction with Eq. 2.66, forms the basis for previously performed simulations for electron cooling of highly charged ions [96, 97]. These simulations suggest that the time scale for electron cooling of highly charged ions is of the order of seconds. It should be noted that, due to the non-trivial impact of electron and ion temperature on the cooling parameter $\tau_i$, the results of these simulations should be treated with caution and are strongly dependent on the input parameters. This becomes even more complicated if the recombination of the highly charged ion with the electrons is taken into account.

Relevant loss mechanisms associated with electron interaction are radiative recombination (RR), dielectronic recombination (DR) and three-body recombination (TBR). While RR is negligible for ions in low charge states, for HCI this process is the most dominant one, as the probability scales with the charge state. An unbound electron is bound by an ion and irradiates the binding energy in the form of a photon. The ion charge state is therefore reduced by one [101]

$$X^{q+} + e^- \rightarrow X^{(q-1)+} + \gamma. \tag{2.70}$$

In the context of DR, the term describes the resonant capture of a free electron into a weakly bound state, while a bound electron is simultaneously excited. During the deexcitation of both electrons, a series of photons is emitted [102]

$$X^{q+} + e^- \rightarrow [X^{(q-1)+}]^{**} \rightarrow X^{(q-1)+} + n\gamma. \tag{2.71}$$
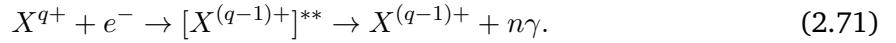
In the case of three-body recombination, two electrons interact within the Coulomb field of an ion. One electron is then captured into a bound state, while the other electron absorbs the corresponding binding energy [95, 103]

$$X^{q+} + e^- + e^- \rightarrow X^{(q-1)+} + e^-. \tag{2.72}$$
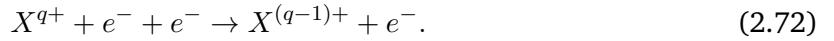
For HCI, DR and TBR are expected to be negligible compared to RR, due to their high charge. Simulations that only consider RR ([97, 98]) predict a high survival probability for highly charged ions as long as either $T_i$ or $T_e$ are high. At the beginning of the cooling process, the electron temperature increases significantly, which in turn reduces the probability of RR as it scales with $T_e^{-1/2}$ [98]. As this leads to a reduction in cooling power, cyclotron cooling rapidly dominates over the heating process. The electron cloud cools down again which in turn increases the cooling power.

Once the ions have transferred all their energy, the electrons cool down to their initial temperature leading to a significant increase in RR as both temperatures, $T_i$ and $T_e$, are now low. This can be prevented by removing either the ions or the electrons from the trap before the rate of

recombination begins to increase. At this point, the ions are already cooled, both in terms of their mean kinetic energy and their energy distribution. The achievable temperature of electron cooling is nevertheless limited to the point at which the rate of recombination begins to increase. To further cool the ions, other cooling techniques, such as resistive cooling (see Sec. 2.3.4), can be employed after removing the electron plasma from the setup.

For the effective cooling of HCI, such as $U^{92+}$, electron cooling is the optimal solution. Given the high mass of the ions, cyclotron cooling can be excluded as the cooling time constant would be in the order of years, while laser-Doppler-cooling is only applicable for a very limited set of ion species. Furthermore, the anticipated broad energy distribution of the ions at HITRAP also excludes the possibility of resistive cooling, as this technique is only effective when applied narrow energy widths. While buffer-gas cooling would result in considerable charge exchange of the HCI with the buffer gas, this leaves only sympathetic cooling with a non-neutral plasma as a viable option for HITRAP. The necessity of a laser cooling setup for ionic plasmas and the challenge in producing and handling large quantities of positrons lead to the conclusion that the special case of electron cooling represents the best option.

Through the application of electron cooling, effective cooling of HCI in the order of seconds with losses of approximately 10% would be possible. However, it is important to note that these values are contingent upon on the plasma parameters, both for the ions and electrons [98]. Simulations that incorporate DR and TBR, with a particular focus on singly charged ions, appear to yield comparable results [96]. It is also noteworthy that neither of these simulations included charge exchange with residual gas in their calculations. Although this was considered to be insignificant under XUV-conditions, the results of initial experimental studies with the given setup indicate that this is not the case for HCI [104].

# 3 Experimental Setup

Although a significant proportion of the matter found in the universe is composed of highly charged ions, they do not occur naturally on Earth. In order to simulate conditions that are otherwise only found in outer space and allow for experiments on highly charged ions, dedicated experimental setups and facilities are necessary. The experiments discussed in this work are performed at the heavy ion accelerator facility GSI in Darmstadt.

The following sections provide an overview of the facility and discuss the production process of heavy, highly charged ions (Sec. 3.1). The experiment itself is part of the HITRAP project, which will be described in detail in Sec. 3.2. This section will focus on the Cooling Trap in Sec. 3.2.5, which is the centrepiece of this work. As ions from the GSI accelerator complex are only available for a limited period of time, the HITRAP project is also equipped with a local ion source, as described in Sec. 3.2.7 as well as an electron source to provide the required electrons (see Sec. 3.2.6).

## 3.1 GSI Accelerator

The GSI Helmholtzzentrum für Schwerionenforschung GmbH, hereafter referred to as GSI, is a worldwide unique facility for heavy ion research. Established in 1969, the facility has undergone continuous expansion with the addition of accelerator structures and experimental setups such as storage rings. The most notable achievements in the over 50-year history of the facility include the first synthesises of six super-heavy elements at the SHIP experiment and the development of ion-beam therapy for cancer treatment [3, 105–110]. Currently, a superconducting continuous-wave linear accelerator (HELIAC) is under construction [111] as well as the arguably biggest expansion so far which is the **F**acility for **A**ntiproton and **I**on **R**esearch (FAIR) [112].

To date GSI is the only facility in the world that can produce and deliver ion beams of any stable and a variety of unstable isotopes in an arbitrary charge state to experiments. For this, the ions are first produced in low charge states by an ion source before they are further accelerated and ionised within the GSI accelerator complex. Subsequently, the ions are delivered to experiments or guided into one of the two storage rings. Figure 3.1 depicts the currently existing facilities. In order to provide the HITRAP project with highly charged ions, they must first pass not only the entire accelerator line but also the Experimental Storage Ring ESR. The following sections will describe the pathway of an ion in more detail, beginning at the ion source in Sec. 3.1.1 and continuing through the acceleration and ionisation stages in Sec. 3.1.2 before concluding with the ESR in Sec. 3.1.3. The ESR represents the final stage prior to HITRAP.

### 3.1.1 Accelerator Ion Sources

The ion source represents the starting point of every ion produced by the GSI accelerator. As the ultimate goal of HITRAP is to provide the heaviest elements at low energies, this and the
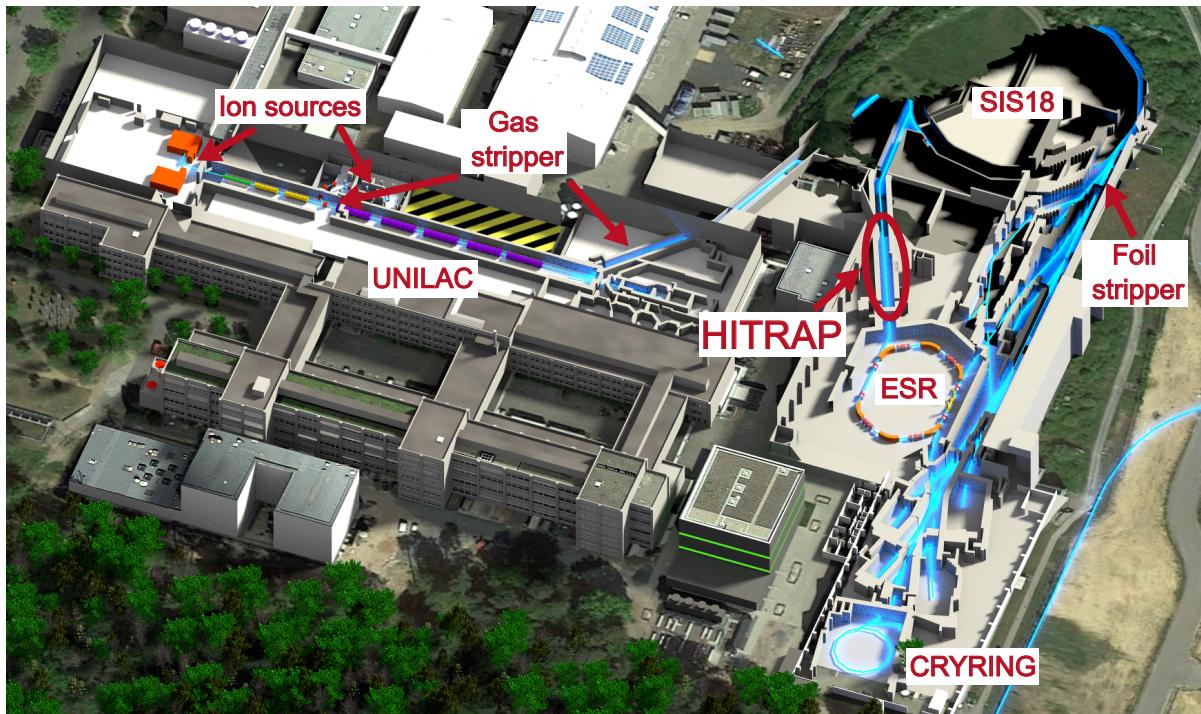
Figure 3.1: The GSI facility and its associated sources, accelerators, stripper targets, storage rings and beam transfer lines. Highlighted with a red circle is the HITRAP project. The different possible ion trajectories are highlighted in blue [113].

following sections will focus on the production of bare uranium as an example.

Available ion sources for the initial production of uranium ions are the Penning Ionization Gauge (PIG), Metal Vapor Vacuum Arc (MEVVA) and Vacuum Arc Ion Source (VARIS). The PIG source is the most versatile of the ion sources considered here, as it is based on ionisation by an electron plasma. In this process, the material is either injected in gaseous form or sputtered from a cathode [114]. The VARIS source is a further developed version of the MEVVA source and both are high-current sources for metal ion beams. A plasma of metal ions is generated by a triggered discharge between a discharge electrode and the cathode.

The ions are then accelerated and guided towards the beam line. After charge separation in a magnetic bender, the continuous-wave (cw) beam of quadruple-charged uranium ions is transported into the high-current injector of the linear accelerator [115, 116].

## 3.1.2 Ion Acceleration

UNILAC is an abbreviation for the **UNI**versal **L**inear **AC**celerator, which is the first acceleration stage of GSI (see Fig. 3.2). The $U^{4+}$ beam, originating from the cw ion sources with an energy of $2.2$ keV/u is then bunched and accelerated by a radio-frequency quadrupole and an interdigital H-mode-drift tube linear (IH-DTL) accelerator to an energy of $1.4$ MeV/u. In a gaseous hydrogen-target stripper, the charge state is increased to $U^{28+}$, which allows for a more efficient acceleration in the following four Alvarez type cavities (Alvarez-DTL) [117]. The final energy after UNILAC may be varied, as the Alvarez cavities allow for beam transport without acceleration and can
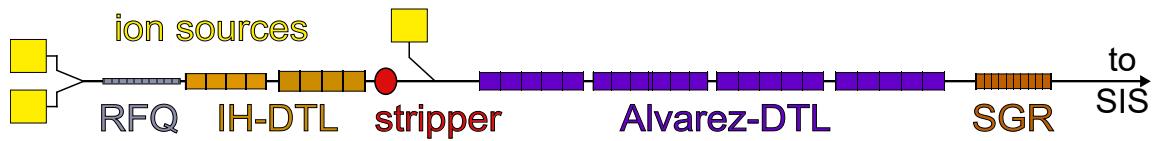
Figure 3.2: Schematic overview of the linear accelerator UNILAC. Produced in the ion sources (yellow), the ions are then accelerated in various acceleration structures before being transported towards the SIS18 synchrotron accelerator or directly towards experiments. For experiments, the final energy can be adjusted by several single gap resonators (SGR) prior to ejection.

be partially excluded from the acceleration process. In combination with multiple single-gap resonators (SGR) the output energy for $U^{28+}$ can be selected by experiments immediately following the UNILAC to be between 3.6 and 13 MeV/u [118].

For experiments requiring higher charged states or higher energies, the beam will be further ionised and then accelerated in the heavy ion synchrotron SIS18 (**S**chwer**I**onen **S**ynchrotron). The ionisation process occurs in the poststripper, where the ion beam with an energy of 11.4 MeV/u is shot onto a solid stripper target. In the case of uranium, a carbon foil of several hundred micrometers in thickness is typically employed, which increases the charge state via electron impact ionisation to $U^{73+}$ [119].

After another magnetic charge separator the ions are injected into SIS18, a synchrotron accelerator with a maximum magnetic rigidity of 18.5 Tm. For experiments requiring high beam intensities, multiple bunches from the UNILAC can be accumulated using a method called multi-turn injection. In the ring of 216 m circumference, the ions are further accelerated with radio-frequency (RF) cavities to a maximum energy of 4.7 GeV/u for protons or approximately 1 GeV/u for $U^{73+}$ [120]. Following acceleration to the desired energy, the ions are either transported to experiments, located for instance at the fragment separator FRS [121], or injected into the experimental storage ring ESR. In the future, ions may also be transported towards the FAIR facility and accelerated to even higher energies by the heavy ion synchrotron SIS100.

Prior to injection into the ESR, a third stripper target is available, which allows for ionisation to the highest charge states up to bare uranium. At this point, nuclear reactions producing rare isotopes are also possible when an ion beam at high energy interacts with the thick stripper target [122].

### 3.1.3 Experimental Storage Ring ESR

Following production, acceleration and stripping, the highly charged ions can finally be injected into the **E**xperimental **S**torage **R**ing (ESR). The schematic layout of the ESR, with a circumference of 108.36 m, is depicted in Fig. 3.3. The injection energy of the ions is dependent on their mass, charge state and intended purpose. For light ions, the injection energy is typically set to 30 MeV/u, while for heavier ions, it can reach a maximum of 550 MeV/u. The upper limit is determined by the ESR's magnetic rigidity of 10 Tm. In particular, if the third stripping stage between SIS18 and ESR is employed, the incoming beam exhibits a high emittance and consists of a mix of charge states and possibly even different isotopes [43, 122]. The high emittance will eventually lead to the loss of the captured ion beam and therefore requires counteraction by cooling the beam.

At the ESR, a combination of stochastic and electron cooling can be applied. In the initial stage
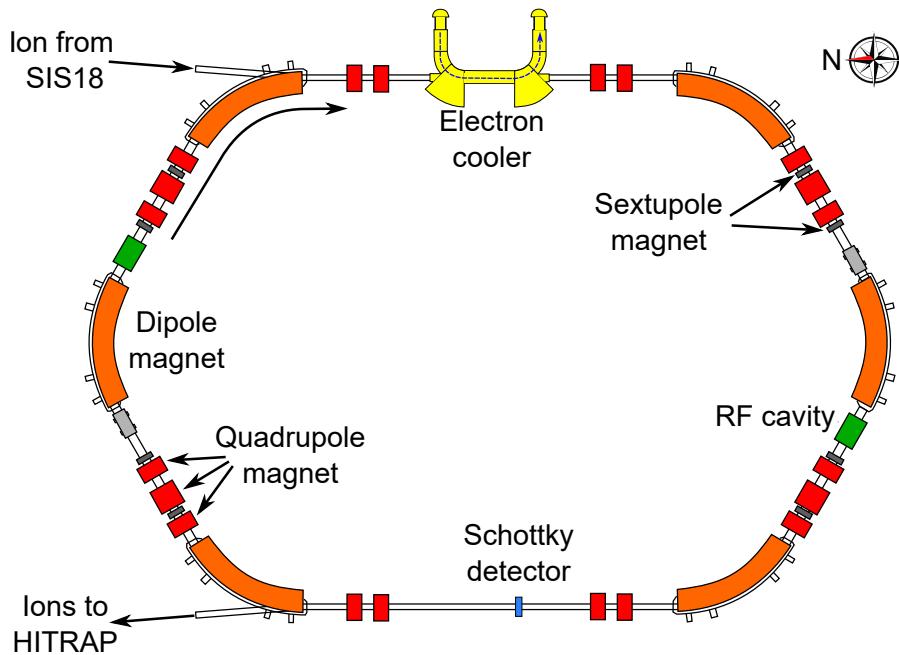
Figure 3.3: Schematic overview of the experimental storage ring ESR. Ions are injected from the SIS18 and then stored, either for experiments or for deceleration and subsequent ejection towards the HITRAP facility. Deceleration is performed within the RF cavities while simultaneously ramping the dipole magnets.

following injection, ion beam properties such as emittance, radius or momentum spread may prevent effective electron cooling, therefore stochastic cooling is employed as a prior cooling step. For this technique, the deviation of the ion beam from the ideal trajectory is detected by an electrical pick-up and translated to a correction signal applied to kicker electrodes [123, 124]. The beam quality is gradually improved during each turn until the beam properties are within the acceptance of electron cooling.

In this second stage, the ions are overlapped with a cold electron beam of approximately the same velocity. Ions travelling at a velocity exceeding that of the electrons transfer energy via coulomb interaction, whereas slower ions are accelerated [125]. This technique results in a very narrow relative momentum uncertainty of down to $10^{-6}$, depending on the number of stored ions [126].

The majority of experiments require a specific ion at a certain charge state. Consequently, it is imperative to select the desired beam components. The ions will circulate on different trajectories, depending on the mass-to-charge ratio. This ratio determines the deflection within the bending magnets. For lower values of the ratio, the deflection is stronger, leading to a smaller radius. Once the beam has been cooled by electron cooling and is on a well-defined trajectory, as a special feature of the ESR the undesired beam components can be blocked by moving in so-called scrapers, allowing for the selection of a single combination of isotope and charge state [127]. Ions with different values of $m/q$ also exhibit different revolution frequencies, which is exploited for Schottky mass spectrometry, where the revolution frequencies of the stored ions are non-destructively picked up and analysed [128].

To provide ions for the HITRAP decelerator, these ions first must be decelerated to an energy of 4 MeV/u within the ESR. While light, highly charged ions such as $C^{6+}$ can already be injected at low kinetic energies, the last ionisation step at the stripper target between SIS18 and the ESR requires significantly higher energies, up to 400 MeV/u for bare uranium. The deceleration in the ESR is achieved by continuously decreasing the frequency of the RF cavities, which reduces the energy with each revolution. This process is divided into two stages, with a short period of electron cooling at 30 MeV/u to restore the beam quality. For lighter ions that are already injected at 30 MeV/u the first stage is omitted. At the end of the deceleration cycle, the ions are cooled once more before being ejected towards HITRAP.

As the beam energy decreases, so does the lifetime of the ions in the storage ring. The dominant loss mechanism here is charge exchange with residual gas, which necessitates maintaining low vacuum conditions of approximately $10^{-11}$ mbar. Nevertheless, a significant loss of ions cannot be avoided, as the beam intensity is reduced by approximately one order of magnitude until the point at which the ions are ejected towards the HITRAP decelerator line. The deceleration process in the ESR can take several tens of seconds, depending on the ion species and initial energy. This is the main limitation for the rate of ions arriving at HITRAP. Including production, acceleration and deceleration in the ESR, it can take as much as one minute from producing an ion in the source to the ion arriving at HITRAP [122, 129].

## 3.2  HITRAP Facility

The HITRAP (**H**ighly charged **I**on **Trap**) facility at GSI has been designed to provide highly charged ions (HCI) for precision experiments. While light and medium-heavy HCI can be produced in large numbers within ion sources such as an electron beam ion trap [9], this is not the case for heavy HCI like $U^{92}$. To date, the production of substantial quantities of heavy HCI requires electron stripping at high kinetic energies. The acceleration and production process of HCI is described in more detail in Sec. 3.1. Depending on mass and charge, the HCI are subsequently stored in the ESR (see Sec. 3.1.3) at kinetic energies of up to 400 MeV/u.

While some experiments require these high kinetic energies and exploit the inherent Lorentz boost [130–132], other experiments would benefit from slower ions or even ions at rest. For example, the precision of laser spectroscopy measurements of the ground-state hyperfine splitting in hydrogen-like $Bi^{82+}$, that was recently performed in the ESR, is dominantly limited by the momentum uncertainty of the stored ions [30]. Performing this measurement on cooled ions within a Penning trap is expected to improve the resulting uncertainty by several orders of magnitude [75]. It is not possible to capture ions at a kinetic energy of several hundreds of MeV/u within an ion trap. Therefore, the ions must first be decelerated again which is precisely the objective of the HITRAP project.

In the initial stage of the process the HCI are decelerated within the ESR to a kinetic energy of 4 MeV/u (for further details, see Sec. 3.1.3). Subsequently, they are ejected towards the HITRAP linear decelerator. The key components of the deceleration line, namely the bunchers, interdigital H-type structure and radio frequency quadrupole, are depicted in Fig. 3.4 and described in more detail within the following chapter. This deceleration line is divided in several beam line sections, starting before the first buncher with GTR1 right after the ESR until the RFQ in GTR4 (see figures A.4 and A.5).
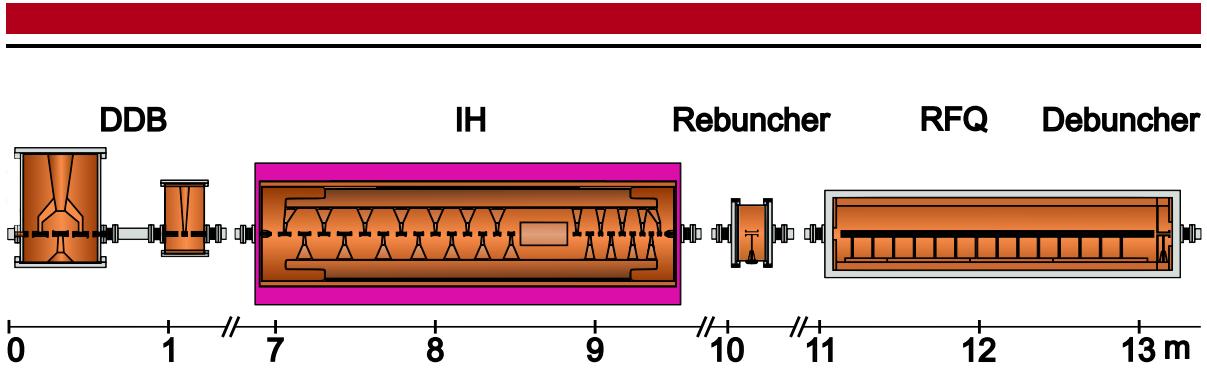
Figure 3.4: Overview of the HITRAP decelerator line (sections GTR2 - GTR4), which consists of a double drift bunching system (DDB), an interdigital H-type (IH) structure, a rebuncher and a radio frequency quadrupole (RFQ) with an installed debuncher. The beamguiding elements between the radio frequency structure are not depicted to improve clarity.

After deceleration, the mean kinetic energy is reduced to 6 keV/u. However, this process also results in a very broad energy distribution of $\pm 1$ keV/u and a $1\sigma$-emittance of approximately 100 $\pi$ mm mrad [16]. Both properties present a significant challenge to further ion transport and require the design of a dedicated beam line for this purpose, which will be discussed in detail in Sec. 3.2.4. The final stage of the HITRAP facility and also the centrepiece of this work is the HITRAP Cooling Trap. Within this Penning trap, the mean kinetic energy of the ion ensemble will be further reduced to a few keV/$q$. Furthermore, the width of the kinetic energy distribution and the emittance will be cooled using electron cooling.

The setup of this trap is described in detail in Sec. 3.2.5 while the for electron cooling required electron source will be discussed in Sec. 3.2.6. As accelerator-produced highly charged ions are only available for a limited time, HITRAP is also equipped with a local ion source, which is treated in Sec. 3.2.7 in more detail. In order to commission both the decelerator line and Cooling Trap a variety of diagnostic tools, as described in Sec. 3.2.8, are necessary.

Following successful deceleration in the linear decelerator line and subsequent cooling within the Cooling Trap, the ions can finally be transported to precision experiments. Currently, four types of experiments are planned at HITRAP, either already partly established or currently under construction. The above mentioned laser spectroscopy on highly charged bismuth is just one of the intended measurements at the **Spec**troscopy **Trap** (SPECTRAP)-experiment. This setup was previously commissioned using locally produced ions [75, 133] and most recently upgraded by a new superconducting magnet and trap design [134]. With the provision of heavy HCI, SPECTRAP enables the study of nuclear and atomic properties such as charge radii or hyperfine splitting via laser spectroscopy with an unprecedented accuracy.

In order to investigate the g-factor of a bound electron in hydrogen-like heavy HCI, the ARTEMIS project was designed. This experiment, which is already in commissioning [135], will employ laser-microwave double-resonance spectroscopy to form a more stringent test of QED in the extreme fields present close to the nucleus of heavy HCI [19].

In addition, at the time of writing this thesis, a new Helmholtz Young Investigator Group is preparing a new experiment, that aims to exploit the unique properties of heavy HCI to form high-precision optical clocks [18]. Furthermore, a GSI Project Advisory Committee (GPAC) approved experiment will perform surface interaction studies with slow heavy HCI in 2025 [20].

### 3.2.1 Bunching System

The first crucial component of the HITRAP decelerator line is a **D**ouble-**D**rift **B**uncher (DDB) located in beam line section GTR2. The pre-decelerated beam, injected from the ESR, has a length of 1-3 µs in the time domain [21]. As the length of the incoming bunches must match the drift tube length within the interdigital H-type structure (for further details, see Sec. 3.2.2), additional bunching is necessary prior to the actual deceleration process.

A DDB comprises two separate bunchers, with the second buncher driven at twice the frequency of the first one. The theoretical bunching efficiency of this device is approximately 60%. The disadvantage of a DDB system is the space-consuming structure, as it requires two bunchers that are separated in space to allow the bunches to form between the two stages. This increases the bunching efficiency, as the bunches are initially formed in the first stage, while the second stage can correct the modulation [136].

At HITRAP, the two bunchers are driven by 108.408 MHz and 216.816 MHz, respectively, and separated by a distance of 0.8 m. The second buncher is located 5.95 m in front of the IH-structure, where distance to the first deceleration stage is given by the longitudinal focus of the DDB [137]. Following the first deceleration stage, a third buncher is installed to account for any longitudinal defocusing. This small spiral buncher is also driven by 108.408 MHz and is designed to maximize the achievable deceleration efficiency within the RFQ (for details see Sec. 3.2.3) [138].

### 3.2.2 IH-Structure

The 10 ns-long microbunches formed by the double drift bunching system are guided into the **I**nterdigital **H**-type (IH) structure, where the first deceleration step at HITRAP takes place. The common use case for such a LINAC (**LIN**ear **AC**celerator) is, as hinted by its name, acceleration of charged particles. The actual acceleration occurs within the gaps between the drift tubes, with the RF-modulation ensuring a polarity change while the bunch is within a tube. The length and velocity of the particle bunch must match the length of the drift tubes, which necessitates the formation of small bunches prior to acceleration. If these conditions are not fulfilled, the efficiency of the acceleration process is significantly reduced.

As the velocity changes after every gap crossing, the design of the drift tubes must also take this into account. For acceleration, this implies that the length of the drift tubes must increase along the cavity in order to fit the particle bunch. Conversely, as the IH-structure at HITRAP is supposed to decelerate ions, the drift tube lengths must decrease along the cavity.

The HITRAP IH-structure in GTR3 is a 2.7 m long cavity with 25 gaps and included quadrupole triplet and steerer pair that decelerates the incoming beam from 4 MeV/u down to 0.49 MeV/u. For ions with a mass-to-charge ratio ≤3 this corresponds to an effective voltage gain of up to 10.5 MV and 180 kW of RF power [137]. By operating at the same frequency of about 108 MHz, the RF signal is phase-locked to the preceding bunching system to ensure efficient deceleration. The cavity was designed using KONUS[1] dynamics, which employs longitudinal focusing through the use of additional rebunching gaps while the quadrupole triplet ensures transversal focusing, eliminating the need for focusing elements within the drift tubes [139].

The deceleration efficiency within the IH-structure is largely determined by the bunching efficiency of the DDB-system, which is approximately 60%. Experimentally, this value was nearly

---

[1]**KO**mbinierte **NU**ll grad **S**truktur or Combined Zero-Degree Structure
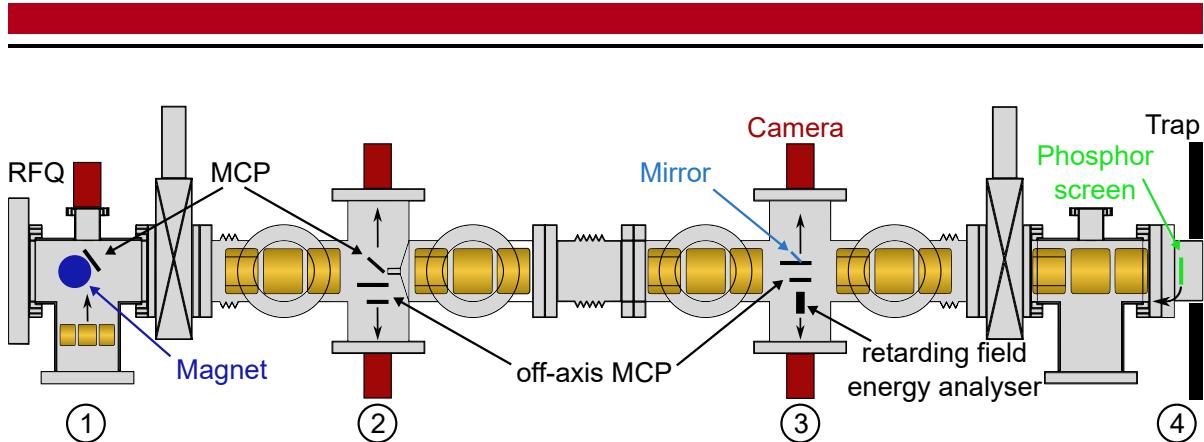
Figure 3.5: Schematic of the low-energy beam line (GTR4-GTR6) between RFQ and Cooling Trap. The numbers below the diagnostic chambers indicate the location referred to in Tab. 3.1.

achieved in previous commission beamtimes at GSI, when more than 50% of the incoming beam could be successfully decelerated [21].

### 3.2.3 Radio Frequency Quadrupole

The final stage of the HITRAP linear decelerator is the four-rod **R**adio **F**requency **Q**uadrupole (RFQ) in GTR4. The ions arrive with an energy of approximately 0.49 MeV/u from the IH-structure and are then further decelerated in the RFQ to a final energy 6 keV/u. The initial design of the RFQ exhibited an energy acceptance of approximately 35 keV/u greater than the output energy of the IH-structure. Consequently, the RFQ underwent a redesign in 2012. This involved modifying the centre of the energy acceptance, increasing its width by a factor of approximately two to $\pm 10$ keV/u, and reducing the sensitivity to the applied RF phase. These improvements facilitate the commissioning process during an experimental beamtime [140, 141].

The current design comprises a 2 m long tube which houses the RFQ itself in addition to a small de-buncher at the end. This de-buncher serves to reduce the energy width of the decelerated beam. The cavity is also driven by a frequency of 108 MHz and can operate at a peak power of up to 80 kW. The decelerated ions are expected to have a mean energy of less than 7 keV/u [141], which was also experimentally confirmed when the energy was measured to be 6-7 keV/u [21]. In addition to the broad energy distribution, the decelerated ion bunch also exhibits a considerable transverse emittance, as simulations suggest it to be up to $100\,\pi$ mm mrad with a deceleration efficiency of up to 60% [16, 21].

### 3.2.4 Low Energy Beam Transport Line

The properties of the decelerated beam with respect to its emittance and width of the energy distribution present a non-trivial challenge for further beam transport. To address this, a **L**ow **E**nergy **B**eam **T**ransport line (LEBT) was specifically designed to handle the divergent ion beam while providing space for proper diagnostic tools.

A one-shot energy analyser is installed to separate the decelerated beam from the non-decelerated components. In order to resolve all present energy components, the magnet of the energy analyser can be combined with two separate screens. More details on the functionality and operation of

Table 3.1: Diagnostic tools installed in the LEBT. Locations 1-4 correspond to the indicators in Fig. 3.5. EA is an abbreviation for energy analyzer.

| location | 1 | 2 | 3 | 4 |
|---|---|---|---|---|
| **installed** | - one-shot EA | - off-axis MCP | - off-axis MCP | - Phosphor screen |
| **diagnostics** | - on-axis MCP | - on-axis MCP | - mirror | |
| | | | - retarding field EA | |

this energy analyser are provided in sections 3.2.8 and 4.2.

Two microchannel plate detectors are included to allow for optimization of the beam transport towards the Cooling Trap. In addition to the detectors needed for ions coming from the RFQ, there is also a retarding-field energy analyser and a phosphor screen detector available that serve as diagnostic tools for ions and electrons ejected from the Cooling Trap during local commissioning. An overview of the installed diagnostics is provided in Tab. 3.1 while a detailed description of the aforementioned detectors is presented in Sec. 3.2.8.

Within the 2 m long connection between the RFQ and the Cooling Trap (see Fig. 3.5), six electrostatic einzel lenses are installed that can be provided with potentials up to $\pm 65$ kV. The set of beam-guiding elements is completed with four additional electrostatic steerer pairs. According to simulations that use a realistic set of decelerated ions from the RFQ, this beam line allows for a transport efficiency of up to 60%. The main limitation for transmission in this case is the implemented pumping barrier with a diameter of 8 mm that separates the RFQs vacuum section from the one of the trap [16]. This is a crucial measure, as the vacuum of the RFQ is only about $1 \cdot 10^{-7}$ mbar and would prevent the desired ultra-high vacuum conditions inside the Cooling Trap, which is of the order of $10^{-13}$ mbar. In order to achieve the required vacuum, this short beam line section is equipped with two ion getter pumps[2], two turbo-molecular pumps[3] and a non-evaporable getter (NEG) pump[4]. The pressure, which is measured directly at the entrance of the Cooling Trap, is below the working range of the installed vacuum gauge of $7 \cdot 10^{-10}$ mbar.

### 3.2.5  Cooling Trap

The HITRAP Cooling Trap represents the central element of this work. Following the deceleration of highly charged ions in the HITRAP linear decelerator, the ions exhibit both a high emittance and a broad energy distribution. This hinders on the one hand an efficient transport of the ions over a long distance towards experiments. On the other hand, the precision of many experiments relies on a well-defined energy distribution that is ideally as narrow as possible. To address these issues and prepare the ions for subsequent experiments, the HITRAP Cooling Trap was designed. The trap setup must overcome a series of challenges, some of which are common to other Penning trap setups, while others are rather unusual and require special solutions. The main challenges are listed in the following:

- The incoming beam of heavy, highly charged ions will have an energy of about 6-7 keV/nucleon. This corresponds to an energy per charge of about $15 \pm 2.5$ keV/$q$ for ions with m/q $\approx 2.5$,

---

[2]Agilent Varian VacIon 300 StarCell
[3]Edwards STP-301 & EBARA ET300W
[4]SAES CapaciTorr Z 400

such as $U^{92+}$. In order to capture an ion bunch with these properties, the trap must be capable of stopping ions with up to $17.5\,\text{keV}/q$. Therefore, a capture potential of more than $17.5\,\text{kV}$ is required. This alone distinguishes the Penning trap setup from the majority of other traps. Furthermore, the length of the ion bunch in the time domain, which is 1-3 µs, demands either a Penning trap with a long distance between the capture electrodes or a method of compressing the ion bunch.

- For the application of electron cooling, it is evident that both electrons and ions must be stored simultaneously in the Penning trap. In addition to the trap having sufficient variability in the electrode configuration to enable the formation of a nested trap potential (see. Sec. 2.2.3), it also must be capable of storing high electron densities. The simulations discussed in Sec. 2.3.6 indicate that an electron cloud comprising approximately $10^9$ electrons is necessary for efficient electron cooling, which in turn gives rise to significant space-charge effects. As these electrons are produced with a pulsed electron source (see Sec. 3.2.6), similar issues to those encountered in the capture of long ion bunches are anticipated. Both these factors and the resulting space-charge potential again demand a long trap volume and the possibility to apply high capture potentials.

- Another crucial aspect of a successful application of electron cooling is the lifetime of an ion's charge state in the Penning trap. In addition to the inevitable losses due to recombination with the electron cloud, the primary mechanism of ion loss is charge exchange with the residual gas. While this process is negligible for ions in low charge states [96], it becomes a significant issue for highly charged ions. The ion lifetime, as defined in Eq. 2.60, is dependent on both the temperature and pressure of the residual gas within the Penning trap. In order to facilitate ion storage over an extended period of time, a cold trap setup with ultra-high vacuum (UHV) conditions is necessary.

- To effectively store bunches of highly charged ions, a sufficiently strong magnetic field is required to radially confine the ions. The magnet must provide a field of several Tesla, that is also highly homogeneous. Inhomogeneities in the magnetic field not only increase the chance of ion loss due to the effects discussed in Sec. 2.2.6, they also reduce the efficiency of non-destructive detection methods or resistive cooling as the motion frequencies become broadened.

These challenges led to the design of the HITRAP Cooling Trap, which is depicted schematically in Fig. 3.6. The key components and features of the setup will be discussed in the following paragraphs.

**Vacuum and Cryogenic Design**

Both the vacuum and cryogenic systems are divided into two sections. The vacuum inside the bore, which contains the electrode stack of the Penning trap, is aimed to be of the order of $\lesssim 10^{-13}$ mbar to minimise ion loss due to charge exchange. To achieve a vacuum pressure this low, the commonly used combination of turbo-molecular pumps, getter pumps and non evaporable-getter (NEG) material is no longer sufficient. Consequently, the vacuum tube containing the Penning trap is cooled down to about $4\,\text{K}$ to act as a cryogenic pump. Any residual gas particles will simply 'freeze' to the cryogenic surface and remain bound. This process is effective for all
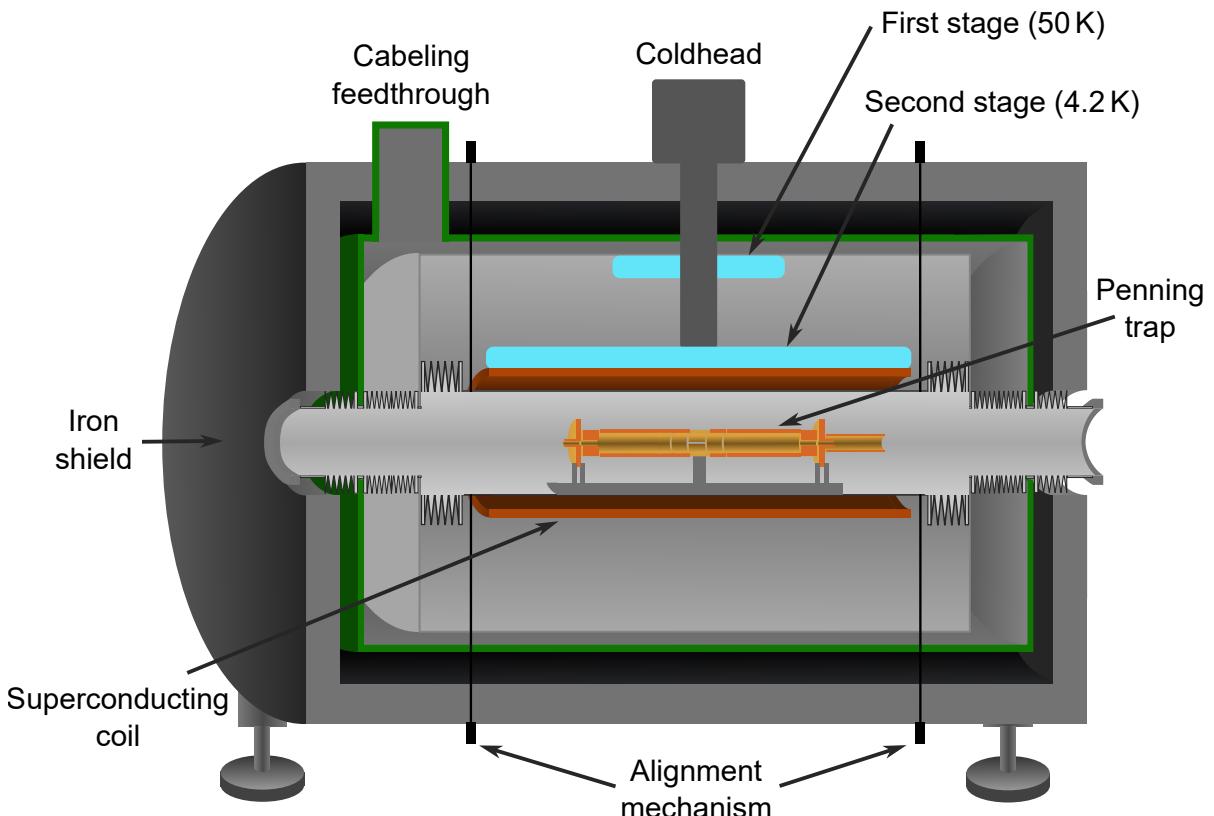
Figure 3.6: Schematic layout of the HITRAP Cooling Trap (GTR6BT1). The two-stage setup contains a isolation-vacuum stage within the green vessel that is cooled by the first stage of the coldhead cooling system. The superconducting magnet and the main vacuum are cooled to approximately 4 K by the second stage of the cooler. To reduce magnetic stray fields, the whole setup is surrounded by an iron shield.

species of particles, although the efficiency drops for lighter particles. Therefore, the remaining residual gas almost exclusively contains hydrogen.

The adjacent vacuum sections are separated by pumping barriers to reduce the flow of additional residual gas into the trap setup, as this would increase the residual gas density in the trap and speed up the coating of the vacuum tube with frozen particles. Once as the cryogenic surface is covered with at least one mono-layer of particles, the pumping efficiency drops, which subsequently leads to a higher residual gas density. At this point, the temperature of the system must be elevated to a level that enables the particles to be released from the surface and to be pumped by vacuum pumps installed in the neighbouring vacuum sections [142].

The main vacuum tube is surrounded by a vessel that contains the isolation-vacuum stage. As conventional copper seals are not applicable at the border between the stages due to the lack of cutting edges, they are separated by an indium seal. Although this type of seal is well suited to these conditions and commonly used for such setups, the achievable vacuum conditions are limited due to a comparably high leakage rate. Consequently, the two-stage design serves two purposes. Primarily it reduces the heat load on the inner tube. The vacuum within the system prevents the transfer of heat due to convection, while the tank itself and the superinsulation

foil inside act as a radiation shield. In addition, the isolation-vacuum stage allows for a lower residual gas density in the main vacuum stage, as it significantly reduces the leakage rate through the indium seal.

Both sections are cooled by a two-stage mechanical cold head cooler[5] with a cooling power of 35 W at 50 K (first stage) and 1.5 W at 4.2 K (second stage). This is driven by a compressor[6] using a Gifford-McMahon cycle with helium [143]. The first stage is connected to the outer tank, while the second stage is connected to the inner vacuum tube and the superconducting magnet. As the cooling power of the second stage is relatively low, it is essential to minimise the heat load, as it is done for example with the radiation shielding [144].

### Superconducting Magnet

The design of the trap setup requires a magnetic field with a strength of several tesla, which can neither be accomplished by the use of permanent magnets nor continuously by conventional electromagnets. Consequently, the HITRAP Cooling Trap incorporates a superconducting magnet that is capable of generating magnetic fields of up to 6 T. As stated in the previous section, the cold bore magnet is cooled to about 4 K in order to facilitate the transition of the niobium-titanium coil into a superconducting state. Within the Penning trap itself, the field inhomogeneity is below $5 \cdot 10^{-4}$ along the trap axis and below $5 \cdot 10^{-5}$ in the radial direction. Outside of the trap region, the magnetic field along the trap axis steeply drops to about 0.5 % at a distance of 1 m from the trap centre. In order to minimise the magnetic field outside of the Cooling Trap in the radial direction, the setup is passively shielded by an iron shield that strongly reduces any stray field outside of the setup.

### The HITRAP Penning Trap

The original Penning trap installed in the HITRAP Cooling Trap consisted of 25 separate electrodes. While this design allowed for a high degree of flexibility in shaping the electric potential inside the trap, due to the complexity and high amount of connections, the electrical setup turned out to be extremely error-prone, which prevented the apparatus from stable operation over an extended period of time.

In 2018, this issue culminated in a completely new design of the Penning trap. The outcome of this redesign is illustrated in Fig. 3.7. While maintaining the fundamental functionality and dimension of the apparatus, the number of electrodes has been reduced to seven. The electrode stack without the mounting structure is approximately 46 cm long with an effective trap length between the two outermost capture electrodes of 38.7 cm. This extended design enables the capture of elongated ion bunches, as expected to arrive at the Cooling Trap from the linear decelerator (see Sec. 3.2.3).

The middle of the electrode stack comprises the so-called 'inner trap' formed by three electrodes with length and radii designed as a mechanically compensated Penning trap allowing for formation of a harmonic potential in the trap centre. The inner trap is separated from the capture electrodes by one long electrode on either side. While the main purpose of these electrodes is to elongate the total trap length, they can also be used for capturing particles.

The set of trap electrodes is completed by the two capture electrodes. While the electrical design

---

[5]SHI Cryogenics Group RDK-415D
[6]SHI Cryogenics Group CSW-71D
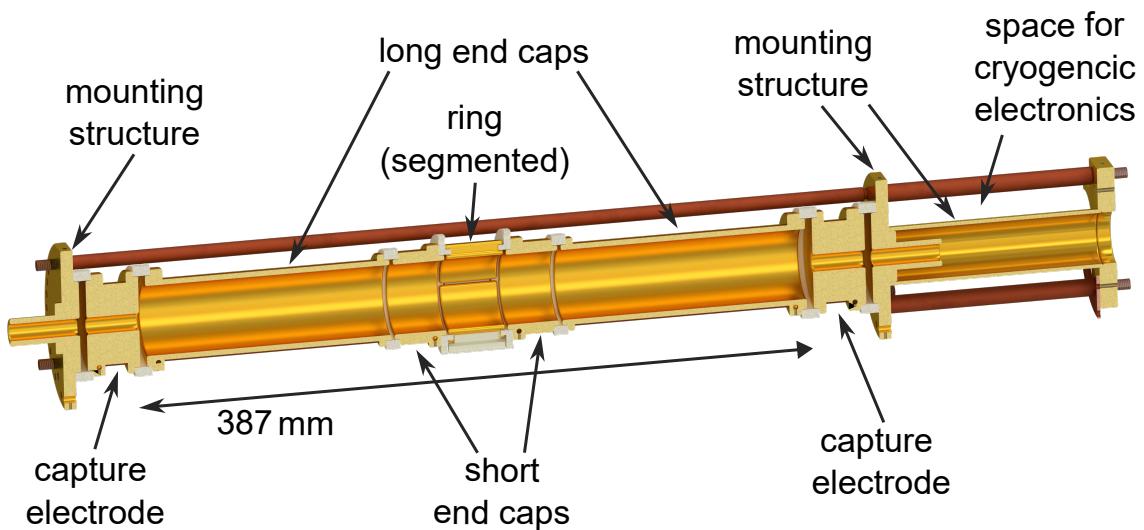
Figure 3.7: Visual representation of the Penning trap inside the HITRAP Cooling Trap setup. The effective trapping volume between the two capture electrodes is 387 mm in length. Between the two short end-cap electrodes, a harmonic potential can be formed as this so-called 'inner trap' is mechanically compensated. In addition to defining the reference potential for the trap, the mounting structure also act as a pumping barrier to improve vacuum conditions inside the trap itself [145].

and insulation for all other electrodes is specified for potential differences of about 1 kV, the cabling and increased spacing for the capture electrodes allows for differences of up to 10 kV. This enables these electrodes to capture ion bunches with energies of several keV/$q$. The inner diameter of the capture electrodes of only 10 mm is also smaller than for the other trap electrodes (41 mm). Simulations indicated that the effective potential in the centre of the capture electrode would only be approximately 75 % of the applied potential if the inner diameter was also 41 mm. In order to reduce the required potential and thereby the likelihood of electrical breakdowns, the inner diameter of the capture electrodes was chosen to be smaller than that of the other trap electrodes.

The capture electrodes are framed by a mounting structure that is set to the same potential as the trap and thereby serves as a potential reference for the trap electrodes. If this structure is biased together with the electrodes, this allows for manipulation of the particles kinetic energy during the capture and ejection process. The electrical design and the hardware involved in shaping the trap potential are described in more detail in the following section. In addition to serve as a potential reference for the trap electrodes, the mounting structure also acts as a pumping barrier. Its small inner diameter of 10 mm reduces the incoming flow of rest gas particles, thereby improving the vacuum inside the trap. One side of the structure also provides space for cryogenic electronics, although at this time there is no hardware installed yet. In the future, the installation of cryogenic resonators, filters and amplifiers is foreseen, which will allow for resistive cooling and non-destructive detection of stored particles.

The electrodes obviously have to be electrically insulated from each other and also from the surrounding vacuum tube. At the same time, the thermal conductivity must be high enough to ensure efficient cooling of the electrodes. This is advantageous, as the temperature of the electrodes limits the lowest temperature achievable by most cooling mechanisms. Additionally,
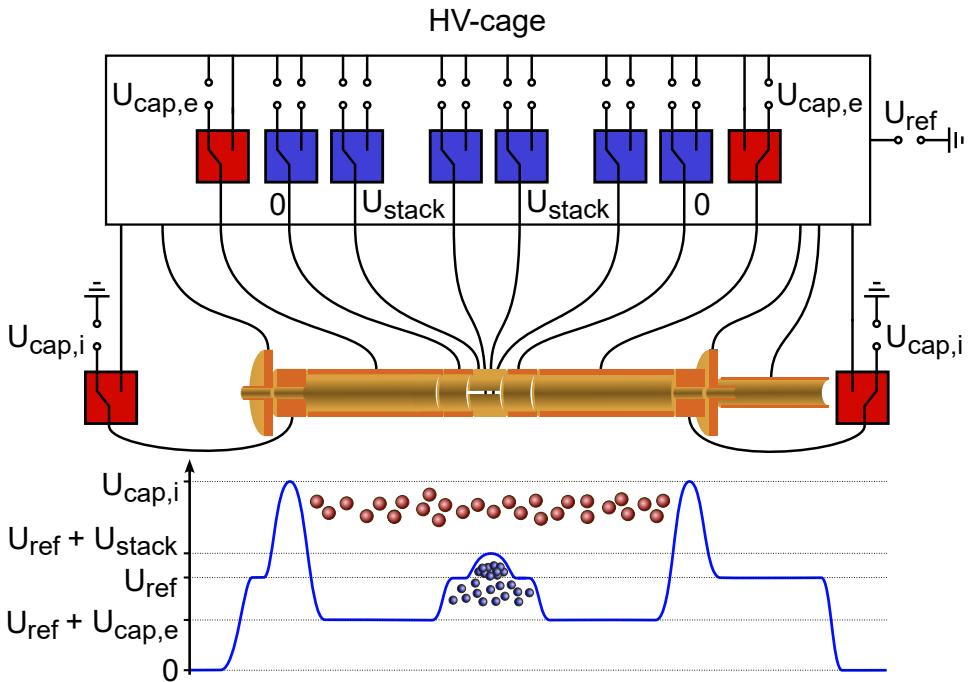
Figure 3.8: Overview of the electrical concept that provides the trap electrodes with the appropriate potentials and switching capabilities. Blue switching units represent the custom-made switches that are provided by $\pm 200\,$V power supplies. Red switching units represent commercial switches with faster transition times. These units are sourced from four-quadrant power supplies that deliver up to $20\,$kV to the capture electrodes and $\pm 6\,$kV to the long end-cap electrodes, respectively. With the exception of the switches and power supplies connected to the capture electrodes, all components are biased by a reference potential of up to $U_{\mathrm{ref}} = \pm 12.5\,$kV. The capabilities of the setup are demonstrated for the example of electron cooling, where the ions and electrons are confined by potentials $U_{\mathrm{cap,i}}$ and $U_{\mathrm{cap,e}}$, respectively. The potential in the trap centre can be shaped arbitrarily and allows in this case for the stacking of multiple electron injections (see Sec. 5.1.1 for details).

the surface of the trap can then act as a cryogenic pump, which improves the vacuum inside. The property of a high thermal conductivity paired with being an electrical insulator is provided in this setup by a composite of aluminium nitride and boron nitride. Both the separation between the electrodes and the mount of the trap are constructed from this material, which allows for cooling of the trap electrodes [145, 146].

**Electrical Concept**

The electrical concept of the HITRAP Penning trap offers a high degree of flexibility in shaping and modifying the potentials within the trap, allowing for a wide range of applications. It is possible to store both negative and positive particles simultaneously in different regions of the trap. Furthermore, the ability to bias the entire setup to potentials up to $\pm 12.5\,$kV enables the manipulation of the particle energy upon injection into the trap or during extraction. This is achieved by defining all electrode potentials relative to this reference potential. While some of these features can also be found in many other trap setups, their combination with the
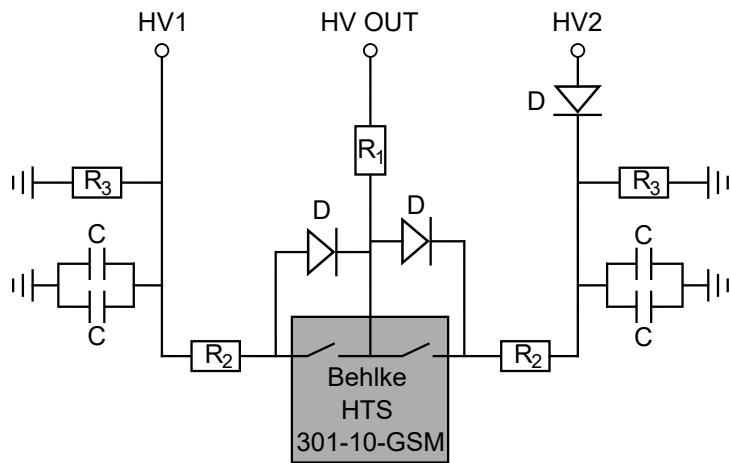
Figure 3.9: Electrical drawing of the switching unit for fast changes in the capture potentials. Resistors $R_1$ and $R_2$ limit the maximum current through the circuit to 100 A at the maximum switching potential of 30 kV, as specified by the manufacturer. For safety reasons, two 1 G$\Omega$ resistors $R_3$ are implemented to discharge the circuit in case the connection to a power supply is removed. The capacitors serve as buffers, while the diodes protect the switch and power supplies from the application of potentially harmful potentials.

comparably high potentials present at HITRAP of up to 20 kV requires several custom solutions. These capabilities are a result of a complex concept comprising a range of cabling solutions, power supplies and switching units, which is schematically illustrated in Fig. 3.8. This section outlines the electrical concept of the setup and subsequently in the following section the timing control will be discussed in more detail.

The cabling is divided into three sections in a manner analogous to the corresponding vacuum stages. Inside the main vacuum tube the cabling between the trap electrodes and the feedthrough towards the isolation-vacuum stage is realised mostly by Kapton-insulated manganin-wires[7] insulated to 6 kV. Their small diameter also ensures a negligible heat load towards the electrodes. Only the two capture electrodes require biasing to up to 20 kV. Thus, they are connected by coaxial cables with higher insulation capabilities.

Inside the isolation-vacuum stage, all cabling is done by high-voltage coaxial cables that lead to three different vacuum feedthroughs. Two of the feedthroughs are reserved for the connection of the capture electrodes, while the third serves for all of the remaining electrical connections, which are transferred through an insulated tube towards a high-voltage cage (HV cage). The cabinet inside this cage contains all of the electrical devices needed for the operation of the Penning trap and can itself be biased to an offset potential. This allows for the manipulation of the reference potential of all electrical devices, including the power supplies, which subsequently leads to an offset in the applied potentials at the electrodes. The reference potential is provided by a four-quadrant power supply that can deliver up to $\pm 12.5$ kV.

Inside the cabinet, the power supplies and switching units for the inner electrodes between the capture electrodes are located. For the short end-caps and ring electrode, this is realised by custom-made units, including both power supplies and switches, produced locally at GSI. These units allow for switching between two arbitrary potentials within the range of $\pm 200$ V. While the

---

[7]312-KAP-MAN-025

transition time $\tau \approx 10\,\mu s$ of these units is sufficient for the manipulation of stored particles, for the capture process shorter transition times are essential. In order to capture fast particles, such as electrons, by the long end-cap electrodes, commercial solid-state switches[8] with a transition time $\tau \approx 100\,ns$ and four-quadrant power supplies[9] are employed.

The two remaining capture electrodes are not connected to the high-voltage cabinet but directly to a custom-made switching unit, which itself is connected to two 20 kV two-quadrant power supplies. This unit was constructed within the scope of this work and its design is based on switching units previously in use at HITRAP. The schematic drawing of the electrical design is shown in Fig. 3.9. The central component of the unit is again a solid-state switch (Behlke HTS 301-10-GSM) that is buffered with two parallel 4.7 nF capacitors on each input side. In order to protect the solid-state switch, any connected power supply and the trap setup, several safety measures have been implemented. The current through the switch is limited by high-voltage resistors to the manufacturer's specified maximum of 100 A at 30 kV switching potential. Additional 1 G$\Omega$ resistors discharge the circuit when the power supply is removed, thereby reducing the potential hazard due to components floating at a high voltage.

### Timing

The timing of the aforementioned switching units is controlled by several high-precision timing units. In order to capture or detect fast particles such as electrons or high-energy ions, precise switching of the electrodes is indispensable. As electrons, for example, take less than a microsecond to pass through the HITRAP Penning trap, the timing precision of the electrode switching must be at least in the same order of magnitude. At HITRAP, this challenge is addressed by utilising a **F**ield **P**rogrammable **G**ate **A**rray (FPGA)-card[10] with a resolution of 5 ns. The Outputs are amplified by a TTL line driver to provide the 5 V-standard.

In order to address the numerous time-sensitive devices, including the aforementioned high-voltage switches, both within and outside the HV cabinet, two FPGA cards are employed. With the exception of the communication between the FPGA modules, which is conducted via optical fibres, the amplified TTL signals are transported using coaxial cables to the corresponding devices. This system is responsible for all devices and timing events that require a sub-millisecond precision including ion and electron production, transport and storage, as well as data acquisition. For less time-critical operations, such as ramping of beam guiding elements, a software-based control is available. Initiated by a signal from an FPGA card, this software runs a predefined sequence in which the desired values are sent directly to the corresponding power supplies. As communication is conducted via network-based variables, it is inevitable that jitters and delays of several milliseconds will occur.

### 3.2.6 Electron Source

A key element for successful electron cooling is a powerful and reliable electron source. Simulations predict that electron densities in the order $10^7\,\frac{1}{cm^3}$ with numbers up to $10^9$ electrons might be necessary to allow for sufficiently fast electron cooling [96–98]. Two principal methods exist for the production and capture of such high electron densities in a Penning trap: accumulation

---

[8]Behlke GHTS 100 A
[9]ISEG THQ 2CH 60W EPU
[10]National Instruments PCI-7811R

by continuous loading and the production and capture of short bunches.

In the case of accumulation by continuous loading, a constant electron beam is injected into the Penning trap and reflected at a far-end electrode while an electrode at the injection side is partially closed. Due to coulomb scattering between the entering and reflected beam, some electrons transfer energy from their axial to their radial modes of motion, enabling them to be trapped between the partially closed electrode and the reflecting electrode. The trapped electrons are cooled via cyclotron cooling (see Sec. 2.3.2) and then enhance the rate of electron capturing as they contribute to the coulomb scattering. This method enabled loading electrons, dependent on the trap length, at rates of up to $6 \cdot 10^8 \frac{1}{s} \frac{1}{cm}$ in [147].

The electron beam itself is typically produced by thermionic cathodes, whereby the metal cathode is heated to sufficiently high temperatures to emit electrons, which are subsequently collimated into a beam. However, the high temperature of the source and the electron beam itself present a challenge for the vacuum around the source, which requires the implementation of numerous precautions for the use in ultra-high vacuum (UHV) environments. Additionally, it is challenging to operate such a source in a pulsed mode, which is necessary if the electron beam has to share a beam line with ions.

An alternative approach is the capture of short high-density electron bunches. The process of capturing electron bunches is analogous to that of ion bunches. In both cases, the charged particles are injected into a Penning trap, reflected at a far-end electrode, and a second electrode at the injection side is switched to a reflecting potential before the particles can leave the trap volume again. These bunches of electrons can, for instance, be produced by a photo-ionization source. The most basic form of such a source operates on the principle of the photoelectric effect, which describes the emission of photons by radiating light of sufficient energy onto a metal surface [148]. This phenomenon has been observed for combinations of a vast variety of metals and light sources, although high yield sources most commonly utilise photo-ionisation based on semiconductors. The measurements presented in this work were conducted using a source developed by Krantz [149], which will be described in more detail in the following.

**The HITRAP Electron Source**

At the HITRAP facility, electrons are extracted from a p-doped gallium arsenide (GaAs) photocathode. The energy gap between the valence and conduction bands is $\Delta E = 1.4$ eV, which means that photons with an energy $E_\gamma > \Delta E$ can excite the electrons from the valence band into the conduction band. Following thermalisation, the electrons settle at the bottom of the conduction band and are separated from the vacuum level by a potential difference, known as the electron affinity $\chi$. While $\chi \approx 4$ eV for GaAs, it can be reduced by applying a monolayer of cesium onto the semiconductor surface. This decreases the potential difference between the conduction band and the vacuum level to $\chi \approx 0$ [150]. The electrons in the conduction band are then only separated from the vacuum level by the very thin potential wall formed by the cesium layer, which they can pass by tunneling through this barrier [149]. The effective potential difference that the electrons must overcome to allow for ionisation is now equivalent to the energy gap between the valence and conduction bands, namely 1.4 eV.

A schematic representation of the electron source and its assembly into the beam line is depicted in Fig. 3.10. The source is mounted at an angle of $35°$ to the beam axis allowing the beam line to
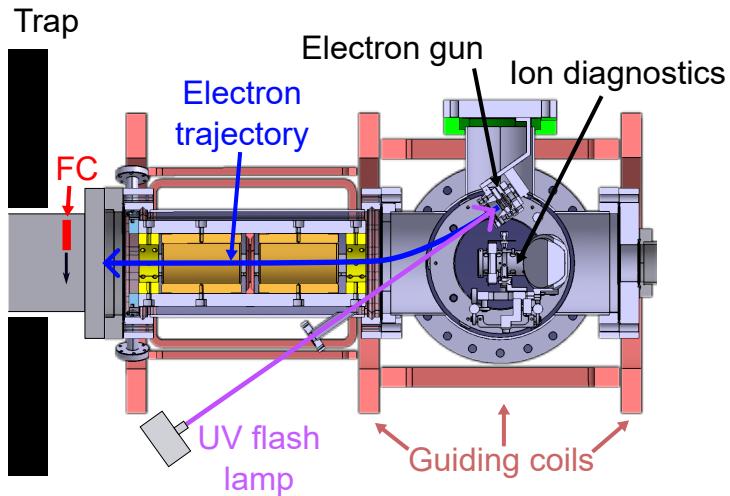
Figure 3.10: Setup of the HITRAP electron source. A flash of UV photons produces a bunch of electrons on the photocathode. The electrons are accelerated by a negative potential and guided towards the Cooling Trap by magnetic coils. Image taken and modified from [149].

be used simultaneously for ion transport. Besides the cathode itself, two additional electrodes are employed to facilitate a controlled extraction and beam shaping. The aforementioned monolayer of cesium can be applied by heating the attached Cs-dispensers[11]. For cleaning purposes, a halogen lamp is installed that can bake the photocathode and thereby remove any pollution from the cathode's surface.

The electrons are produced and released from the GaAs photocathode by radiating an intense flash of ultraviolet light onto the source. The light source in use is a xenon flash lamp[12] with a spectral peak around 5 eV. This lamp is capable of delivering light pulses of up to 100 mJ within less than 1 μs [151]. The electrons produced by this source are accelerated by a negative electric potential applied to the photocathode and then transported towards the HITRAP Cooling Trap using a total of ten guiding coils. These copper coils both steer and focus the electron beam into the magnetic field of the Cooling Trap and are operated in a pulsed mode to prevent interference with any ions sent to the trap.

### 3.2.7 Local Ion Source

The principal technique employed at GSI for the production of highly charged ions is a combination of acceleration and electron stripping, as described in Sec. 3.1.2. While this technique offers a unique flexibility in producing a vast variety of intense ion beams at an arbitrary charge state, it is not suitable for the commissioning of the Cooling Trap. The availability of beamtime, combined with the time-consuming deceleration process, would make the commissioning of a complicated process such as electron cooling in a Penning trap impossible.

There are numerous forms of ion sources that can be operated locally, but only few are capable of producing highly charged ions. Most commonly used are either an **E**lectron **C**yclotron **I**on **R**esonance **S**ource (ECRIS) or an **E**lectron **B**eam **I**on **S**ource/**T**rap (EBIS/T). Ranging from in-

---

[11]SAES Getters $Cs_2CrO_4$
[12]Hamamatsu L11316-11

source X-Ray spectroscopy [152], producing exotic ions for laser spectroscopy [153] or precision mass measurement on heavy highly charged ions [56] to the use as intense ion sources for storage rings [154], these local ion sources can cover a broad spectrum of applications. At HITRAP, a compact EBIS/T is available for the commissioning of the Cooling Trap, as well as offline experiments [133]. This SPARC-EBIT is a room-temperature Dresden EBIT based on permanent magnets that was developed by DREEBIT[13] [155, 156].

The working principle of an EBIT is based on electron impact ionisation. In a manner similar to a Penning trap, the design of such an EBIT includes a three-electrode electrostatic ion trap with open end caps. Produced by a thermionic cathode, a beam of electrons is accelerated by a negative potential towards the trap, where it is focused to the trap centre by the permanent magnets. After passing through the trap region, the electrons are deflected onto a collector by the negatively biased extractor electrode. A schematic drawing of such an EBIT is depicted in Fig. 3.11.

To produce ions in this source, gaseous atoms or molecules are injected into the trap region. The high-intensity electron beam passes through the trap, where it ionises the atoms or molecules present. The resulting ions are trapped axially between the two end-cap electrodes. Radial confinement is achieved by the space-charge potential of the electron beam.

The maximum achievable charge state is first and foremost limited by the density and kinetic energy of the electron beam. The latter must be higher than the binding energy of the electron to be removed, which is achieved with a maximum efficiency at values of about 2-3 times the binding energy [9, 157]. The beam energy is determined by the cathode's acceleration potential and the positive bias applied to the central drift tube. This is also the main limitation for the production of heavy, highly charged ions in an EBIT. For example, ideal conditions for producing bare uranium would require electron energies of up to 300 keV which are technically challenging to realise. Although possible, the production rates of bare uranium with lower electron energies are marginal [158].

In addition to its kinetic energy, in particular the electron beam density and the storage time of the ions play an important role in the resulting charge-state distribution. In a charge breeder such as an EBIT, the latter is referred to as the breeding time, as it describes the time during which the charge state of the ion is formed. The longer the breeding time, the higher the charge state achievable in an EBIT. The breeding process is counteracted by a number of loss mechanisms such as charge exchange with other ions or residual gas, recombination with the electron beam and particle loss from the source. These processes are analogous to those observed in Penning traps and are discussed in greater detail in Sec. 2.2.6. At a certain point, the rate of ion loss will cancel the ionisation rate, and further increasing the breeding time will not result in greater abundances of higher charge states.

After the breeding time, the ions can be ejected towards the adjacent beam line by lowering the trapping potential at the extractor side. It should be noted that the ejected ion bunch contains a broad charge state distribution, depending on the breeding time, as the ionisation process is of statistical nature. The total kinetic energy of the ions is determined by their charge and the bias potential of the central drift tube.

An alternative to the aforementioned pulsed mode operation, is continuous ion beam production. In this mode of operation, the end cap at the extraction side is set to a potential only slightly

---

[13]https://www.dreebit.com/
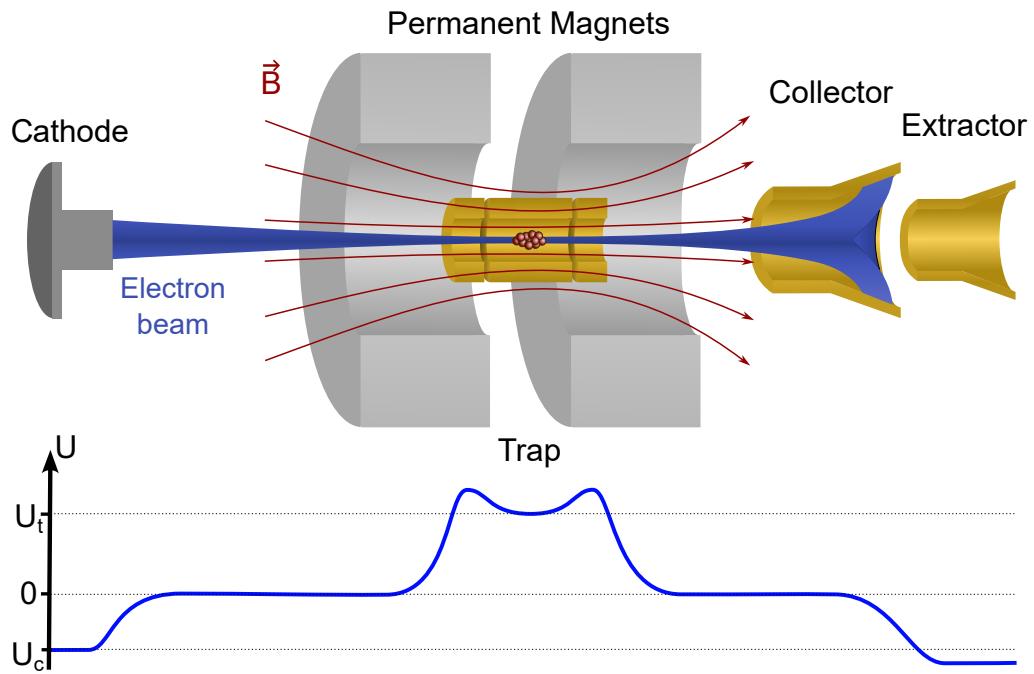
Figure 3.11: Top: Schematic layout of an electron beam ion trap (EBIT). Neutral atoms or molecules (red) are injected into the trap region and then ionised by the electron beam (blue). Following the ionisation process, the ions are ejected by lowering the potential of the right trap electrode. The extractor electrode is at a slightly lower potential than the cathode to deflect the electron beam onto the collector electrode. The ion energy is determined by the potential of the central trap electrode, $U_{\mathrm{t}}$, while the electrons are accelerated by the potential difference between the central trap electrode and the cathode $U_{\mathrm{t}} - U_{\mathrm{c}}$.

higher than the central drift tube potential. Similar to the process of evaporative cooling, ions with sufficient energy to overcome this confining potential are continuously dripping out of the trap into the beam line. Due to the limited interaction time between the electron beam and a single ion, the achievable charge state for this mode is usually also lower than in the pulsed operation [9].

In general, the ions available from an EBIS/T source are limited to gaseous isotopes to allow for injection into the source. The use of gaseous compounds also enables the production of otherwise solid isotopes, such as boron or iron, using the MIVOC (**M**etal **I**ons from **VO**latile **C**ompounds) method [145]. Furthermore, an EBIT can also be employed as a charge breeder in combination with an external ion source. In this operational mode, ions are generated at low charge states externally by a dedicated ion source and then injected into the EBIT. Following further ionisation by the electron beam, the ions can then be ejected once again. This method essentially enables the production of any given stable or long-lived rare isotope in a highly charged state [157].

## 3.2.8 Diagnostics

During the operation of the decelerator and the Cooling Trap, both electrons and ions in a wide range of energies are present and require proper diagnosis. As HITRAP is a unique facility, unique challenges arise alongside the already commonly known ones for such a setup with respect to

the needed diagnostic tools. The following sections will provide an overview of the detectors and diagnostic tools in use at HITRAP.

### Faraday Cups

In many accelerator setups, transformers are employed to measure the beam current. However, due to the combination of low current and high electrical noise, this is not a viable option at HITRAP. Instead, Faraday cup (FC) detectors are utilised, which measure the charge deployed in a conductor. The deposited charge induces a current that is amplified by a fast transimpedance amplifier[14]. The measured signal can then be converted into a current or number of incoming charged particles if the particle's charge is known. In particular, for high-energetic ion beams, this measurement is distorted by secondary electrons released from the FC, which is indistinguishable from the signal produced by positively charged particles. Consequently, the measured signal appears reduced for negative particles and increased for positive particles compared to the actually deposited charge. This can be prevented by applying a retarding field to the suppressor electrode that accelerates the secondary electrons back to the cup [159].

### Luminescence Screens

While Faraday cups yield both the amount of deposited charge and the longitudinal shape of the detected beam, no information on the transversal distribution can be extracted. Therefore, FCs are often combined with a luminescence screen within the same diagnostic chamber, as is also the case at HITRAP. The luminescence induced by the incoming beam is then detected by a CCD camera to extract the transversal beam profile. The choice of screen material depends on the ion beam properties. Commonly used materials include cerium-doped yttrium aluminium garnet (YAG) and P43 phosphor [160, 161]. For sufficient beam intensity and energy as available directly after the ESR, YAG scintillation screens offer an effective solution for beam imaging. Should the intensity of the beam induced luminescence be insufficient for the camera to detect, the YAG screens can be replaced by microchannel plate and phosphor screen combinations in which the produced and multiplied electrons activate the phosphorescence [162].

### Microchannel Plate Detectors

If utilisation of a FC is not feasible due to insufficient beam current or electrical noise, for instance induced by rapid switching of high potentials, which prevents the deployment of a current amplifier, microchannel plate detectors (MCP) offer a viable alternative. Despite the absence of the capability for charge counting, MCPs are sensitive to single particles.
An MCP is an array of electron multiplier tubes that produce electrons when hit by an incoming particle. The electrons are accelerated by a positive potential applied to the back plate of the MCP resulting in the release of secondary electrons, which in turn initiates an electron avalanche. Typical gains of a single MCP are in the order of $10^3$ to $10^4$, depending on the acceleration voltage [163]. At HITRAP, the majority MCP detection units are equipped with a stack of two MCPs which increases the gain to the order of $10^6$. The schematic of such a detection unit is depeicted on the left-hand side of Fig. 3.12.
After passing the two MCPs, the produced secondary electrons are accelerated onto a phosphor

---

[14]FEMTO DHPCA-100
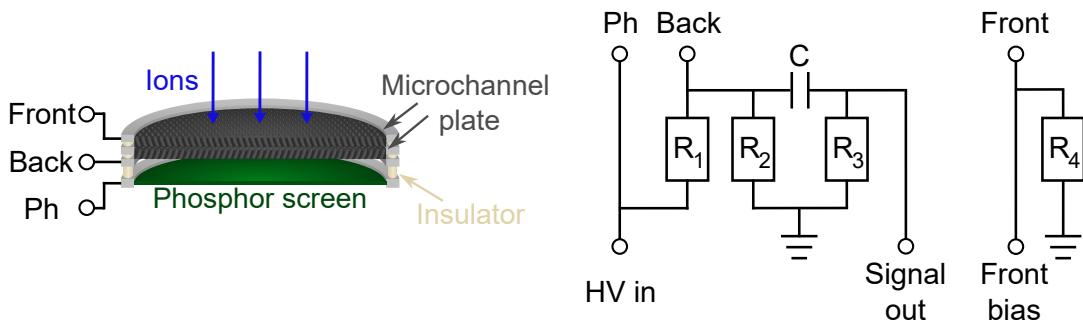
Figure 3.12: Left: schematic of a microchannel plate detection unit comprising two plates and a phosphor screen. Right: Circuit of the voltage divider unit that supplies the necessary potentials for the detector. The ratio between the phosphor screen potential and the back plate of the MCP is at HITRAP either 2:1 or 3:2. While the front plate is typically grounded, it is possible to apply a bias potential.

screen, allowing for the visualisation of the incoming particle beam. The required acceleration potentials for the operation of such a detector are provided by a high-voltage power supply and a voltage divider, as depicted on the right side in Fig. 3.12. The voltage ratio between the phosphor screen and the back plate of the MCP varies depending on the use case and is at HITRAP either 2:1 or 3:2. This configuration enables the measurement of changes in the supply voltage resulting from the deposition of the secondary electrons into the phosphor screen.

The induced signal is related to the quantity of incoming particles and can, to some extent, be employed to quantify relative changes in beam intensity. However, as the number of produced secondary electrons is contingent upon variables such as the mass or energy of the incoming particles and the applied acceleration voltage, this signal cannot be used to provide a precise value for the beam current. Furthermore, the dead time, which is in general approximately 10 ns for each channel, can result in saturation for intense beams, where a further increase in intensity would not contribute to a higher signal or might even damage the detector [75, 164].

In their standard configuration, these MCP detectors are mounted within a diagnostic chamber and can be moved into the beam axis such that the detector is perpendicular to the beam axis. However, this concept has two major disadvantages, which are particularly relevant for the specific requirements of HITRAP:

- The first disadvantage is related to the linear decelerator. As previously described (Sec. 3.2.4), following deceleration, the beam after the RFQ contains not only decelerated ions with energies of about 6 keV/u, but also non- or partly decelerated components. Simulations suggest that a clear separation by time-of-flight is not possible due to the short distance between the RFQ and Cooling Trap. Transporting decelerated ions through this beam line would then present an even more complex challenge as is, given the limitation of detection capabilities.

- The second disadvantage arose during the offline commissioning of the Cooling Trap. For some of the tests that were performed during this work, it is necessary to send ions back into the direction of their source after capturing and storing them in the Cooling Trap. This requires a detector that is non-destructive while the ions are transported from source to
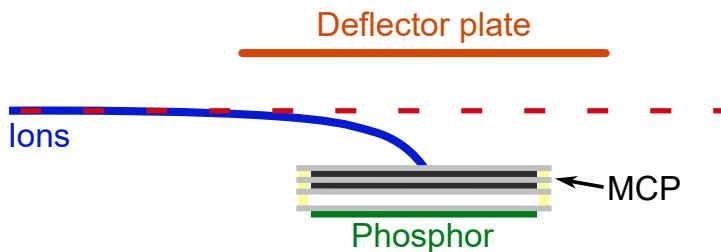
Figure 3.13: Schematic of an off-axis MCP detection unit. The ions (blue) are deflected by a copper deflector plate onto an MCP detector. If no potentials are applied to the plate or the MCP or if the ion energy is to high for the applied potentials, the ions will pass the detector undisturbed.

trap and at the same time capable of detecting the ions on their way back. Using on-axis MCP detectors would necessitate the detector moving at a sufficient speed in and out of the beam trajectory. While theoretically feasible, this is not the case at HITRAP.

In order to address both of these disadvantages simultaneously, an off-axis solution is employed. A schematic representation of this configuration is depicted in Fig. 3.13. The MCP detector is mounted parallel to the beam axis and the particles are deflected onto the detector by a deflection plate. On the one hand, this allows for the separation of the decelerated beam from the remaining high-energetic components. On the other hand, it provides the possibility of switching on and off the detector simply by changing potentials. If no potentials are applied at the MCP detector and the deflector plate, ions should not be affected by the setup.

**Phase Probes**

The operation of the HITRAP facility requires not only the detection of ions and their longitudinal and transversal distribution using the above described detectors, but also the measurement of their energy. In order to achieve this, several complementary measurement principles are employed. For ions coming from the ESR, the first energy measurement is conducted with phase probes. These non-destructive detectors comprise a set of at least two spatially separated pick-up electrodes, as described in Sec 2.2.5.

Ions passing through such a cylindrical electrode induce an electrical signal, which can be measured to determine the energy of the ions. This is achieved by measuring the time difference between the induced signal in two separated probes. When working with a bunched beam, as is commonly done in accelerators and also after the double-drift bunching system of HITRAP, the measurement becomes more complex. The phase probes then pick up a periodic signal with a frequency that is determined by the buncher.

A direct measurement of the time-of-flight for one single bunch becomes more challenging and instead, the phase shift $\triangle t$ between the two periodic signals is analysed. The measurement principle is illustrated in Fig. 3.14 on the basis of an idealised induced signal. As the two points selected for measuring the phase shift are not necessarily induced by the same ion bunch, it is essential to correct the measurement for this additional phase difference. Accordingly, an integer multiple $n$ of the signal's periodicity $T$, determined by the bunching frequency, is added to calculate the time-of-flight (TOF) as follows:

$$TOF = \triangle t + n \cdot T. \tag{3.1}$$
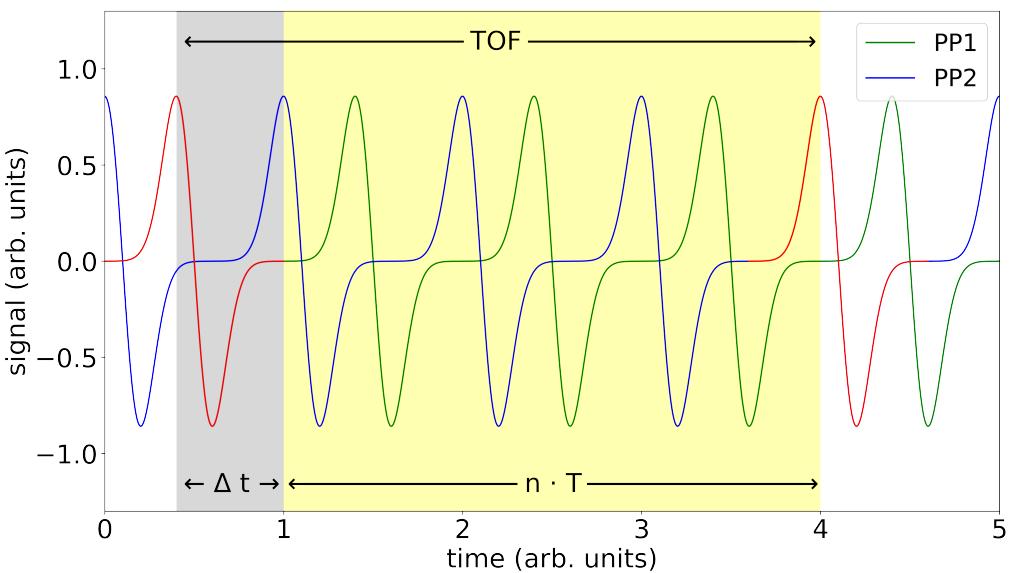
Figure 3.14: Measurement principle of a phase probe detector set for the determination of the time-of-flight (TOF) for a single bunch. At an arbitrary time, the signal of two spatially separated phase probes PP1 and PP2 is detected. The total TOF is then the sum of the phase shift $\triangle t$ (grey) between two neighbouring peaks and the correction $n \cdot T$ (yellow). Geometrically, $n$ describes the number of bunches between the two phase probe pick-ups at the time of the measurement. In this example, $n = 3$ for a given distance between the detectors and ion energy. The signals induced by the same ion bunch are highlighted in red.

In a geometrical sense, $n$ denotes the number of longitudinal bunches that fit into the distance between two separate phase probes. If the kinetic energy of the ions is completely unknown, the determination of $n$ requires a third phase probe. Measuring then the phase shift $\triangle t$ for all three combinations $i$ of two phase probes each, yields a system of equation that only allows for only one single combination of integers $n_i$. In the context of HITRAP, the necessity for a third phase probe is obviated by the fact that the energy is already well defined by the ESR. Consequently, only one potential value of $n$ will yield an energy within the uncertainty margin of the ESR [165].

**One-Shot Energy Analyser**

In order to optimise the deceleration of ions in the IH-structure or the RFQ, it is necessary to resolve the energy components of the decelerated beam. As the deceleration process never reaches 100% efficiency, there will always be considerable amounts of non-decelerated ions present with the original or an intermediate energy. Consequently, the application of phase probes detectors, which are employed to determine the energy of the extracted beam subsequent to the ESR, is not feasible. This technique is only viable for detecting a beam with one single energy component [66]. Furthermore, the separation by time-of-flight is also not a viable option, as a clean separation would necessitate a distance of several tens of metres. Consequently, one-shot energy analysers are installed in close proximity to the IH-structure and RFQ, achieving separation by permanent magnets.
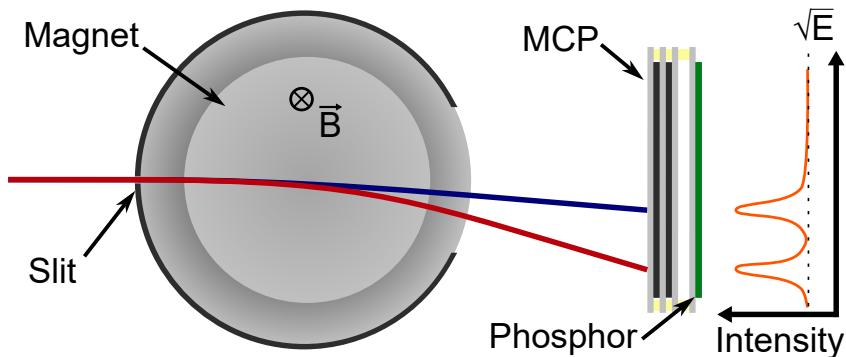
Figure 3.15: Illustration of the working principle of the one-shot energy analysers installed at HITRAP. The incoming ions are deflected by the magnetic field coming out of the plane, which separates the energy components as ions with less kinetic energy (red) are deflected more than ions with greater energy (blue). This separation can be visualized by an MCP detector with a phosphor screen. From the resulting intensity distribution, i.e., the distance between the observed peaks, the energy of the ions can be determined, since the deflection is proportional to the square root of the energy.

A schematic representation of the setup is depicted in Fig. 3.15. After passing a 0.1 mm wide slit, the ions are deflected by a dipole magnet and hit an MCP detector with phosphor screen, enabling visualisation of the displacement of the energy components [166]. The fluorescence of the screen is captured by a CCD camera, allowing for an energy-sensitive measurement of the beam components with a resolution of approximately 1 % at 500 keV/u, as the displacement is proportional to $\sqrt{E}$ [167]. After the IH-structure, the dipole magnet has a field strength of 0.5 T, while the one situated after the RFQ produces a field of 0.1 T. With regard to the RFQ energy analyser, the MCP is partially covered by a mesh that permits only for 5 % transmission of the high energy components, thereby enhancing the instrument's sensitivity for detecting the decelerated ions [21].

**Retarding Field Energy Analyser**

For energy measurements of locally produced ions or ions stored in the Cooling Trap, a retarding field energy analyzer was designed. The analyser comprises an MCP detector and three copper meshes, which allow the energy distribution of an ion beam to be measured by scanning the applied retarding field potential. A schematic view of the detector is shown in Fig. 3.16. The spacing of the meshes are designed such that total transmission through all three meshes is 60 %. The outermost mesh is at ground potential, as is the front electrode of the MCP detector. Both inner meshes are biased by a positive potential, creating a retarding field. To minimise potential penetration through the biased mesh, two meshes are employed instead of a single one, which reduces the penetration to 0.9 % instead of 3.7 %, thus increasing the detector's resolution.
Ions can only pass the retarding field and be detected by the MCP detector if their energy per charge in the motion component perpendicular to the mesh is higher than the applied potential. For lower energies, the ions are reflected and do not contribute to the measured signal. The dependency on the angle of the ion trajectory to the electric field limits the resolution of the detector and complicates the analysis process. It can, in principle, be eliminated by the introduction of two apertures in front of the detector. However, these apertures would also
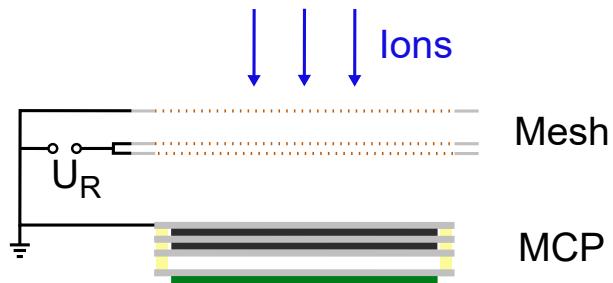
Figure 3.16: Schematic of a retarding field energy analyser. The second and third meshes are biased with a retarding field potential. In order to improve the homogeneity of the retarding field, these meshes are shifted such that the holes are not overlapping.

significantly reduce the intensity of the ion beam, and are therefore currently not implemented. The energy distribution of the ion beam can be determined by measuring the ion signal while scanning the applied potential and then calculating the derivative. This detector is placed in the first diagnostic chamber after the Cooling Trap setup (i.e. GTR5DF3, see Fig. A.6).

# 4 Deceleration of Accelerator-Produced Ions

First proposed in 1990, the HITRAP project comprised the construction of a small storage ring for deceleration after the ESR [168]. In the early 2000s, this design was replaced by a linear decelerator before construction could start in 2005 [169, 170]. The commissioning of the components commenced with the first experimental runs at HITRAP in 2007 and concluded for the time being with the successful deceleration in the RFQ in 2014 [21, 171]. As a result of a shortage of personnel and a reallocation of resources towards the recently arrived low-energy storage ring CRYRING@ESR in 2015, the development and commissioning of the HITRAP linear decelerator came to a halt.

After nearly eight years of stagnation, work on the decelerator recommenced in 2022 and the results of the final experimental run, conducted in 2014, were successfully replicated in a beamtime using $^{58}Ni^{28+}$. The ions were decelerated from the ESR extraction energy of 4 MeV/u down to a value of approximately 6 keV/u [30]. This experimental campaign, along with the subsequent two beamtimes scheduled for 2024, was prepared and conducted within the scope of this work. In the first beamtime in 2024, technical issues precluded a stable operation of the IH-structure and the successful deceleration of the ion species $^{12}C^{6+}$ and $^{18}O^{8+}$ within the RFQ. The second run constituted a significant advancement in the commissioning process, as it enabled for the first time not only the deceleration of the $^{36}Ar^{18+}$-ions in the RF-cavities but also their transportation along the subsequent low energy beam line to the Cooling Trap, followed by their capture, storage and re-extraction from the trap.

In the following, a detailed examination of the results and findings of these beamtimes will be presented, with a particular focus on the last and most successful campaign. Unless otherwise stated, all data presented and discussed in this chapter were obtained during the last aforementioned beamtimes, which took place in April 2024. After a brief overview of the ion production process in Sec. 4.1, the deceleration in the linear decelerator is described in Sec. 4.2. This is followed by the subsequent transport through the LEBT in Sec. 4.2.3 before the results of the first storage of accelerator-produced ions in a Penning trap are presented in Sec. 4.3.2. At the end of this chapter, future improvements and the next steps in the commissioning process of the HITRAP facility are discussed (Sec. 4.4).

## 4.1 Ion Production

During the three commissioning beamtimes described in the following sections, four different ion species were employed. Ranging from very light isotopes with $^{12}C^{6+}$ up to medium heavy $^{58}Ni^{28+}$, this also leads to four different production processes. In order to maintain clarity, this section will focus on $^{36}Ar^{18+}$, as the majority of the presented results were obtained from tests with this isotope.

The Ar ions are initially produced in an CAPRICE-type ECR ion source (ECRIS) from enriched

$^{36}$Ar gas. After acceleration in the UNILAC to 11.4 MeV/u, the ions are completely ionised to bare $^{36}$Ar$^{18+}$ by a gaseous stripper target. Following a brief acceleration within the heavy-ion synchrotron SIS18, they are ejected with an energy of now 45 MeV/u towards the ESR.

The incoming bunches of up to $2 \cdot 10^8$ ions then undergo the first deceleration step. Following injection, the ion beam is cooled by the electron cooler and subsequently the two RF-cavities reduce the kinetic energy down to $(4.02 \pm 0.01)$ MeV/u. The final energy is ultimately determined by the electron cooler during a brief final cooling period following the completion of the deceleration process. Even though the energy distribution after electron cooling is very narrow, with a width in the order $\triangle E/E \approx 10^{-4}$, the uncertainty of the mean energy is significantly higher. This is due to uncertainties in the set voltage of the coolers' electron acceleration potential, space-charge effects within the electron beam and the unknown contact potential between the emission cathode and the electron cooler drift tubes. The aforementioned effects result in a discrepancy between the prescribed and actual electron energy, which directly leads to a shift in the ions' kinetic energy.

The lifetime of the ions decreases during the deceleration, as the recombination rate of the highly charged ions with the residual gas increases at lower energies. A fast and efficient deceleration and cooling of the beam is therefore essential. The quantity of stored ions is nevertheless reduced by almost one order of magnitude down to approximately $3 \cdot 10^7$ during the deceleration cycle. The remaining ions are finally ejected towards the HITRAP linear decelerator.

The whole process to this point, including production, acceleration and the initial deceleration step in the ESR, takes about 43 seconds. The majority of this time is spent in the ESR, where the cooling and deceleration cycle takes approximately 32 seconds.

## 4.2 Deceleration in the Linear Decelerator

Subsequent to the initial deceleration phase in the ESR, the ions are ejected in a single bunch towards the HITRAP linear decelerator, exhibiting a narrow energy distribution centered around the target energy of approximately 4 MeV/u. After a comparatively trivial transport of the beam through the transport line between the ESR and the linear decelerator, beam properties such as horizontal distribution and number of ions are measured at the designated diagnostic chamber GTR2DK3 (see Fig A.5). At this point, about $10^7$ ions are detected by a Faraday cup.

In order to meet the longitudinal acceptance of the IH-structure, the beam is bunched by the double-drift bunching system (DDB) into microbunches. The separation of the bunches in the time domain is determined by the bunching frequency of 108.408 MHz, which corresponds to a time interval of approximately $T = 9.2$ ns. The first buncher of the system, GTR2BB1, establishes the phase reference for all subsequent RF-structures. The second buncher GTR2BB2 operates at twice the frequency of the first buncher. Its purpose is to improve the bunching efficiency, thereby maximising the deceleration efficiency in the IH-structure.

Following the bunching in the DDB, the energy of the beam can be measured by a set of phase probe detectors (see Sec. 3.2.8). The two ring pick-ups are separated by a distance of $d = (3167.65 \pm 0.50)$ mm of beam line, with the second one being situated in close proximity to the IH-structure. The signal induced in the phase probes is illustrated in Fig. 4.1 and the phase shift $\triangle t$ is determined by a software implemented in the control system to be $(3.385 \pm 0.050)$ ns. By employing Eq. 3.1 and the relativistic relation between kinetic energy $E_{\text{kin}}$ and velocity $v$

$$E_{\text{kin}} = \sqrt{(\gamma m_0 v c)^2 + (m_0 c^2)^2} - m_0 c^2, \tag{4.1}$$
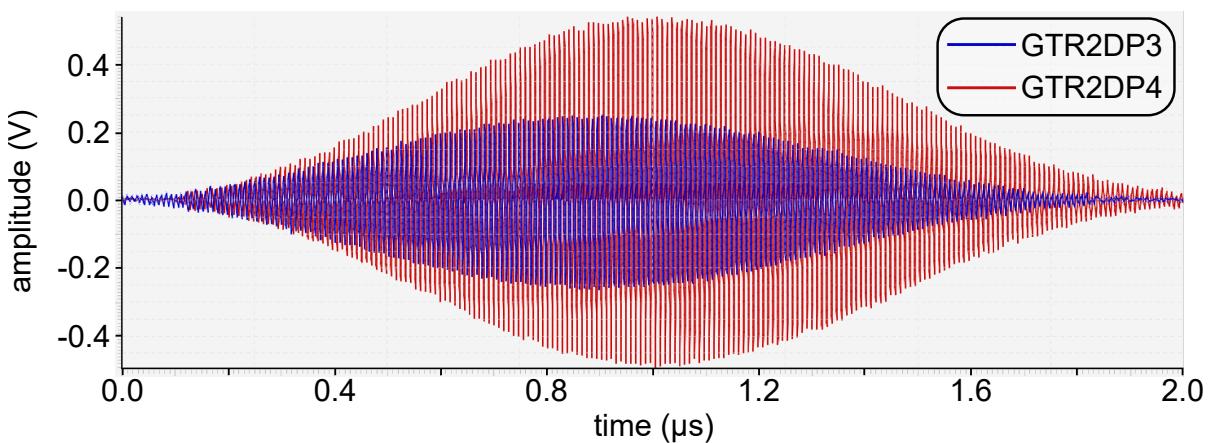
Figure 4.1: Signal induced in the phase probe detectors GTR2DP3 (blue) and GTR2DP4 (red) plotted over time. From the phase shift $\triangle t = (3.385 \pm 0.050)$ ns between the two signals, the ion energy can be determined to be $E_{\text{kin}} = (4021.5 \pm 3.8)$ keV/u.

with the rest mass $m_0$, speed of light in vacuum $c$ and Lorentz factor

$$\gamma = \frac{1}{\sqrt{1 - (v/c)^2}}, \tag{4.2}$$

the kinetic energy of the ions can be calculated. This yields a set of potential solutions for various integer values of $n$ as listed in Tab. 4.1. As only the energy for $n = 12$ provides a result within the margin of error for the kinetic energy determined by the ESR, the ion energy is determined to be $E_{\text{kin}} = 4021.5 \pm 3.8$ keV/u. The given uncertainty is predominantly determined by electrical noise disturbing the measurement of $\triangle t$. Previous commissioning beamtimes have demonstrated that this result aligns with the longitudinal requirements of the IH-structure.

Table 4.1: Possible values for the kinetic energies corresponding to a measured phase shift of (3.385±0.050) ns and various integer $n$. Only the value $n = 12$ yields a result that is physically meaningful and within the uncertainty of the ESR electron cooler.

| n | 10 | 11 | **12** | 13 | 14 |
|---|---|---|---|---|---|
| energy (keV/u) | 5738.5±6.3 | 4765.8±4.8 | **4021.5±3.8** | 3439.1±3.0 | 2974.8±2.4 |

### 4.2.1 IH-structure

In the next step, the ion beam is transported through the IH-structure, while the RF-cavity is in a paused state. In order to ensure a reproducible operation of the RF machines, the RF signal of 108.408 MHz is consistently transmitted for periods of 1 ms to the cavities with a repetition rate of 15 Hz. This maintains a constant temperature and mitigates fluctuations in efficiency due to thermal effects. The signal is only synchronised with the incoming ion beam for a duration of 1 ms around the arrival time of the ion bunch.

In some instances, it is essential to place certain RF-cavities in a paused state, e.g. for the above described energy determination by phase probes. In this case, the synchronisation to the ion

beam is deactivated and the ions can pass the cavity unaffected. Operating the IH-structure produces a large amount of electrical noise, which would consequently compromise the results and prevent an accurate measurement. Furthermore, the initial transport through a cavity is facilitated if the machine is paused.

In order to align the ion beam in the centre of the IH-structure, a pair of movable slits is available for use. It is imperative that the beam position is precisely adjusted prior to deceleration in order to allow for an optimal result. Minor deviations from the ideal trajectory or deflections within the first part of the cavity can be rectified by utilising the integrated quadrupole triplet and steerer pair that is located after the first 15 gaps (see Fig. 3.4).

Once the beam alignment process is complete, the IH-structure is activated, and the RF signal is synchronised with the ion beam. The set value of the RF power is a crucial parameter for the commissioning of the decelerator, as is its phase with respect to the DDB. In normal operation, the ions are located within a drift tube of the cavity when an accelerating voltage is applied between the drift tubes, and they are situated between two drift tubes for a decelerating voltage. In the event of a phase mismatch, this no longer applies to the entire ion bunch. Subsequently, the ion bunches undergo partial deceleration and acceleration. Should the phase be shifted by 180° the ions will even be completely accelerated upon passing the first gap. However, the declining drift tube sizes have been designed with deceleration in mind, which will result in an inefficient acceleration across the entire length of the cavity.

The second crucial parameter for the RF input is the power $P_{\text{in}}$, that is correlated to the applied effective deceleration voltage $U_{\text{eff}}$ by the equation

$$P_{\text{in}} = \frac{U_{\text{eff}}^2}{Z_{\text{eff}} T l}. \tag{4.3}$$

Here, $Z_{\text{eff}} = 220\,\text{M}\Omega/\text{m}$ denotes the effective shunt resistance and $l = 2.613\,\text{m}$ the length of the cavity, while the transit-time factor $T = 0.85$ accounts for the change of the RF field, while the ions traverse through the gap [137, 172]. Given that the energy reduction per mass is proportional to the ions' charge for a given electrical field, the optimal setting is also contingent upon the mass-to-charge ratio of the ions. As the ratio increases, the required RF power to achieve a given deceleration also rises. Example values are provided in Tab. 4.2. The calculated required power for the isotopes of interest is presented in addition to the effective deceleration voltage over the entire length of the cavity. An excessive or insufficient level of applied power will reduce in the efficiency of the deceleration process.

The successful deceleration of ions from 4 MeV/u to approximately 0.5 MeV/u can be achieved through the precise selection of RF amplitude and phase. In order to determine the energy of the decelerated beam and the efficiency of the deceleration process, a one-shot energy analyser (see Sec. 3.2.8) is installed after the IH-structure in GTR3DK5. The ions pass through a slit situated in front of a permanent dipole magnet with a field of 500 mT, whereupon they are deflected within this magnet by an amount that depends on their energy. Subsequently, the ions are detected by an MCP detector and the fluorescence of the screen is observed with a camera.

An exemplary image produced by the detector is provided on the left-hand side of Fig. 4.2. The figure on the right depicts the projection of the detected signal onto the vertical axis, wherein the ion signal is plotted in relation to the position, with reference to the signal's maximum. The vertical position of the signal can be translated into the ions' kinetic energy, with the high-energy part being located at the top and the parts with less energy towards the bottom. This enables the data to be separated into two distinct categories: those ions that have undergone complete

Table 4.2: Effective deceleration voltages $U_{\text{eff}}$ and the corresponding required RF power $P_{\text{in}}$ for deceleration from 4 MeV/u to 0.5 MeV/u of various isotopes within the IH-structure.

| isotope | $m/q$ (u/e) | $U_{\text{eff}}$ (MV) | $P_{\text{in}}$ (kW) |
|---------|-------------|----------------------|----------------------|
| $^{12}\text{C}^{6+}$ | 2.00 | 7.00 | 100.3 |
| $^{36}\text{Ar}^{18+}$ | 2.00 | 7.00 | 100.3 |
| $^{58}\text{Ni}^{28+}$ | 2.07 | 7.25 | 107.6 |
| $^{18}\text{O}^{8+}$ | 2.25 | 7.88 | 126.9 |
| $^{238}\text{U}^{92+}$ | 2.59 | 9.07 | 167.8 |

deceleration at the bottom and those that have not. The signal's maximum corresponds to ions with an energy of approximately 4 MeV/u. Ions that are accelerated within the IH-structure, due to a mismatch in phase, should be located on top of the undecelerated ions but cannot be clearly distinguished. Below of the primary peak, mainly in the region from 0 to -5 mm one can discern intermediate energies, resulting from ions entering the cavity with a slight deviation from the ideal phase or trajectory.

As a consequence of the narrow energy acceptance of the subsequent deceleration step in the RFQ, only fully decelerated ions are relevant for the commissioning process and are thus marked green in the vertical projection. The remaining ions, both those that have not been decelerated and those that have only been partially decelerated, can be considered lost and are marked red. Integration over the marked area, allows derivation of the deceleration efficiency. In the example of Fig. 4.2, the proportion of decelerated ions is calculated to be approximately 23 %. This result is considerably below the theoretical limit of 60% and also well below the previously achieved 50% during beamtimes in 2014 [21]. Although, the IH-structure could be at least partially successfully operated in all three machine runs conducted as part of this work, at no point could these earlier results be reproduced.

During the commissioning phase, a number of minor and major issues arose, that hindered the reliable operation of the cavity. In addition to a leak in the water cooling system of the built-in quadrupole triplet and steerer, the majority of these errors are likely associated with the RF electronics. A notable impediment to the commissioning process was the malfunction of a plunger. This metallic device serves to accommodate minor fluctuations in the cavity's resonance frequency by changing position, thereby neutralising the impact of temperature-related deformations. In normal operation, the position of the plunger is regulated automatically; however, this automation failed when higher RF powers were required. Additionally, an issue related to the shape of the radio frequency signal arises predominantly at higher powers. In ideal conditions, a perfect sinusoidal signal is transmitted into the cavity. If the frequency of the signal does not perfectly match the resonance frequency of the cavity, a portion of the transmitted power is reflected back, thereby reducing the effective field applied between the drift tubes. With the defective plunger, higher harmonics became visible on the RF signal, which is indicative of the aforementioned reflection of power. Alternatively, these higher harmonics can occur if a proportion of the RF power is directed into these higher harmonics as a result of an imperfect configuration of the setup. The cause of the error-prone plunger regulation remains uncertain. It is possible that the
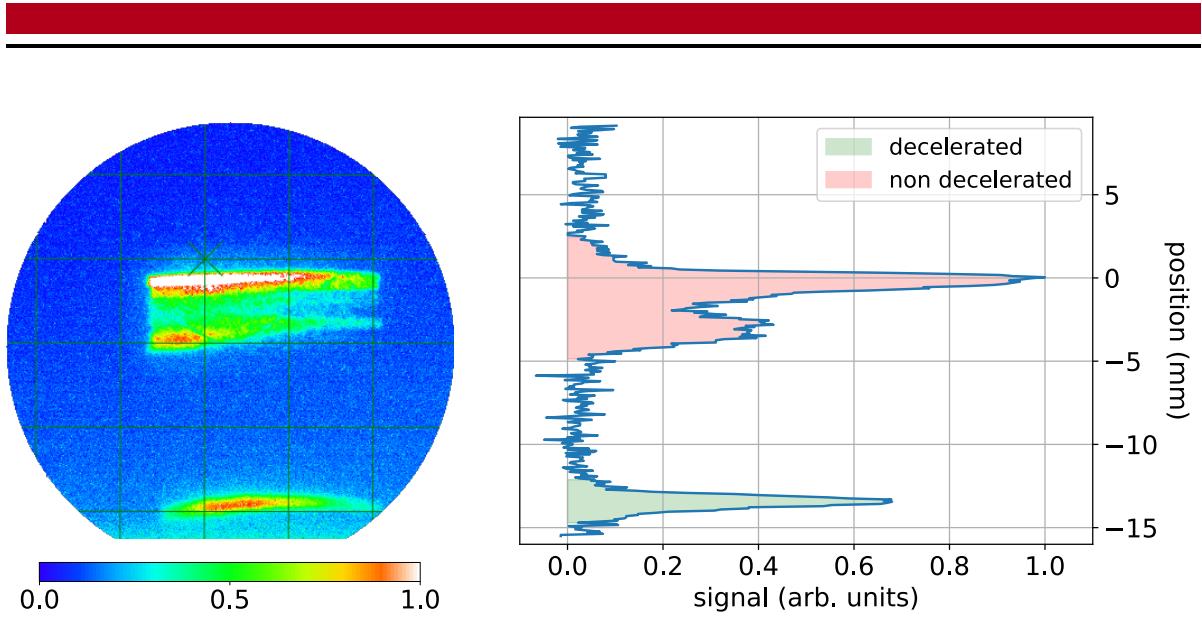
Figure 4.2: Left: exemplary result from the one-shot energy analyser in GTR3DK5 after the IH-structure. The ions are deflected by a magnet depending on their kinetic energy. The closer the signal is to the bottom of the image, the lower the ions' kinetic energy. The colour scale indicates the relative intensity. Right: intensity projected onto the vertical axis. The decelerated components are marked green, while the signal from non-decelerated ions is marked red.

malfunction of the plunger is due to a defect in the power supply or RF-amplifier, which prevents a proper functioning of the plunger.

In addition to the issues with the RF signal generation, also the power required for successful deceleration is significantly higher than expected from the values in Tab. 4.2. In the case of the isotopes employed in the commissioning runs described here, the generated RF power was observed to be approximately 10 % higher than those expected to achieve deceleration in the cavity. A number of potential explanations for this are conceivable:

- It is possible that the issues with the RF-electronics are the cause for this behaviour. The aforementioned higher harmonics visible in the RF signal provide compelling evidence that not the full power is transmitted into the cavity but rather it is being partially reflected or directed into higher harmonics.

- Since the last beamtime in 2014, the IH-structure, despite being under vacuum for the majority of the time, has not been in use. Even minor alterations to the internal surface can cause perturbations in the cavity, impeding interference-free operation, particularly in the presence of a potential water leak towards the vacuum chamber.

- In preparation for the beamtime in 2022, a broken power coupler was also replaced. However, it is conceivable that the replacement does not function as intended.

Currently the issues with the IH-structure are under extensive investigation in the frame of the preparations for upcoming beamtimes at HITRAP in 2025. Given that these campaigns are scheduled with heavy ions of higher $m/q$-ratios, a considerable increase in power will be required for deceleration, rendering a repair of the cavity and accompanying electronics imperative.
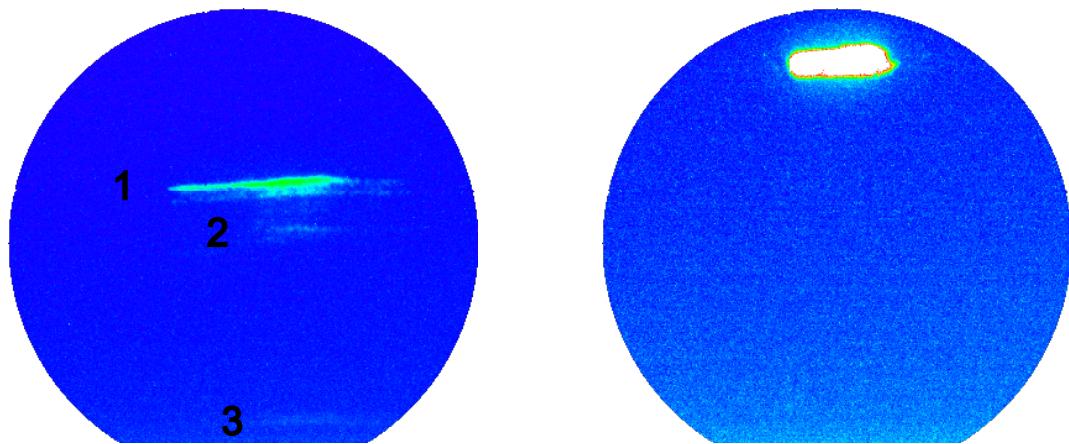
Figure 4.3: The image on the left depicts the signal produced by the energy analyser following the IH-structure in GTR3DK5 with slits closed to 0.3 mm. It can be observed that three distinct components are present, each corresponding to a different ion energy. The image on the right illustrates the offset position of the ion beam, with the deflector magnet and IH-structure in a paused state. By measuring the distance between the offset and the signal components, it is possible to ascertain the ions' kinetic energy.

Table 4.3: Positions of the three marked energy components in Fig. 4.3 relative to the offset position. The corresponding kinetic energies $E_{\text{kin}}$ are calculated using Eq. 4.4, where $y - y_0 = d$.

| component | distance $d$ (mm) | kinetic energy $E_{\text{kin}}$ (keV/u) |
|:---:|:---:|:---:|
| 1 | 6.78±0.04 | 4026±39 |
| 2 | 9.00±0.20 | 2302±96 |
| 3 | 19.74±0.09 | 489±3 |

**Energy Calibration**

The indications of an anomalous behaviour of the IH-structure may suggest that the output energy also differs from the design value of 490 keV/u, which was previously confirmed in other beamtimes. It is therefore necessary to undertake a revised determination of the kinetic energy of the decelerated component. Given that the deflection within the magnet is inversely proportional to the ions momentum and, thus, approximately to the square root of the ions' kinetic energy, it is possible to determine the energy of the ions by analysing the vertical intensity distribution.

In order to achieve an accurate energy calibration and calculate the precise energy of the decelerated component, it is essential to ensure that the incoming ions pass through the slit of the energy analyser perpendicularly. To this end, the slit situated after the IH-structure is narrowed down to a width of 0.3 mm. Thus, only ions that deviate negligibly from the ideal trajectory pass both slits and contribute to the signal on the energy analyser. This results in a strong reduction of the signal intensity, but also allows for a higher resolution of the measurement.

Once the beam is aligned through both slits, the position of the energy components is determined (Fig. 4.3 left). As a point of reference, the offset position $y_0$ is measured by removing the magnet and setting the IH-structure in paused mode. The result is shown in the right part of Fig. 4.3.

Employing the relation between kinetic energy $E_{\text{kin}}$ and screen position $y$

$$E[\text{keV/u}] = 300.83 + 13822.756 \cdot \exp\left(-\frac{y - y_0}{4.594\,\text{mm}}\right) - 788204.5 \cdot \exp\left(-\frac{y - y_0}{0.9364\,\text{mm}}\right), \quad (4.4)$$

the vertical axis can be translated to an energy axis. This formula is derived from simulations combined with an initial calibration of the detector using well-known ion energies [66, 166]. In Tab 4.3, the distances of the energy components marked on the left side of Fig. 4.3 to the offset position are listed, as well as their corresponding energies. All positions and distances are derived by extracting the vertical projection of the left measurement in Fig. 4.3 and subsequent fitting of the peaks. With the resulting positions of the peaks, the vertical axis can be calibrated to an energy axis by employing Eq. 4.4. The given uncertainties are composed of uncertainties stemming from the fitting routine and calibration process.

Non-decelerated ions create the signal labeled as 1, as the measured energy of 4026±39 keV/u is in very good agreement with the energy measured in front of the IH-structure by the phase probe. The second energy component exhibits a kinetic energy of 2302±96 keV/u, which is likely correspondent to an intermediate energy state of the decelerator that is still outside the acceptance range of the RFQ. Only ions that contribute to the signal at position 3 can be further decelerated, as their energy of 489±3 keV/u falls within the accepted range of the RFQ, which is 485±10 keV/u. The issues of the IH-structure discussed above, appear to only reduce the deceleration efficiency, yet do not influence the final output energy. Consequently, the possibility of further transport along the beam line and deceleration within the RFQ remains viable.

### 4.2.2 RFQ

Following a successful deceleration in the IH-structure, the ions are transported further along the beam line with an energy of approximately 0.5 MeV/u towards the second deceleration step in the RFQ. In order to enhance the efficiency of the RFQ, a third single buncher (GTR5BB3) is employed to reshape the ion bunches. In order to ascertain the optimal configuration of the buncher, the signal on the energy analyser subsequent to the IH-structure is observed while simultaneously scanning the phase of the buncher. The outcome of this measurement is illustrated in Fig. 4.4, where the energy of the decelerated beam is plotted over the bunching phase of GTR3BB3.
A deviation from the optimal phase of the bunching RF signal may result in the acceleration or deceleration of the ions by up to 30 keV/u in the buncher. This is evidenced by a shift in the position of the decelerated ions, that can be observed on the energy analyser. Two distinct phases, 0° and 180°, are observed to result in no change in energy. One of these two phases corresponds to the bunching mode, and the other to the debunching mode. In order to achieve deceleration in the RFQ, it is evident that the appropriate configuration would be the bunching mode. However, at this point, it is not feasible to distinguish between the two potential options, as the deceleration efficiency in the RFQ must be monitored for this purpose.
As with the IH-structure, the first step towards deceleration in the RFQ is a precise alignment of the ion beam through the centre of the cavity. In this case, the process is more challenging due to the residual high-energety beam components that remain present in the beam line. The short distance and minimal disparity in velocity preclude the possibility of temporal separation by time-of-flight thereby rendering the utilisation of conventional Faraday cups or MCP detectors unfeasible. This is due to the fact that the primary beam will inevitably exert a dominant influence
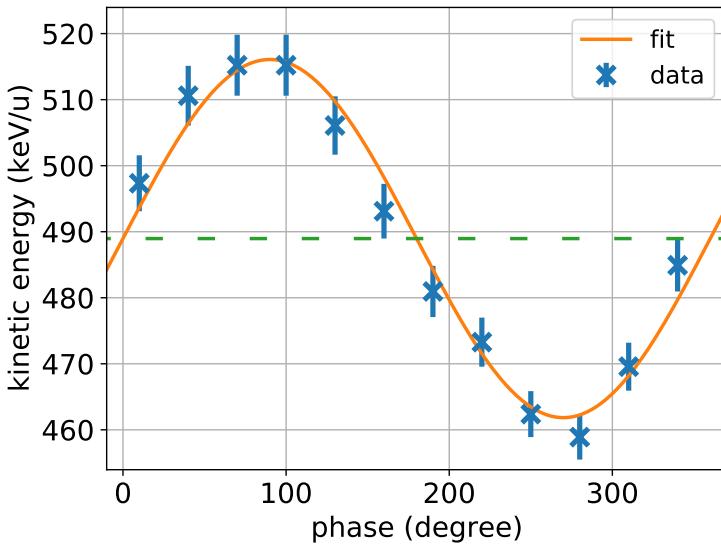
Figure 4.4: Phase scan of the rebuncher between the IH-structure and the RFQ to ascertain the ideal phase setting. The phase of GTR3BB3 is plotted against the energy of the decelerated beam on the energy analyser after the IH-structure. A sine function (orange) is fitted to the data to extract the values which do not lead to any acceleration by the buncher, that is, the crossing points with the green dashed line.

over the signal emanating from of the 0.5 MeV/u-ions.

In order to separate the energy components, the magnet of the energy analyser, situated after the RFQ in GTR4DK1, is employed. This energy analyser is originally designed to separate the completely decelerated ions with an energy of about 6 keV/u from higher energies (0.5 and 4 MeV/u). Consequently, a weaker magnet, with a magnetic field of only 100 mT, is installed. This prevents a conventional use of this energy analyser with the accompanying MCP detector in the same diagnostic chamber. Instead, the magnet is combined with the on-axis MCP detector GTR5DF1 in the subsequent diagnostic chamber (GTR5DK1). The longer flight path towards this detector allows for the separation of the 0.5 MeV/u component from the primary beam, even with a comparatively weak deflector magnet. This setup is visualised in Fig. 4.5.

The observed signal is depicted in the left frame of Fig. 4.6. Again, the vertical position is inversely proportional to the square root of the ion's kinetic energy, with the higher energy being located at the top of the screen. A calibration of the detector to extract the kinetic energy from the vertical position has been omitted in this case, as the objective is solely to facilitate detection and alignment through the RFQ of the ions decelerated within the IH-structure. There are three separate energy components visible, that represent, from top to bottom, the primary beam, an intermediate energy for partially decelerated ions and the completely decelerated ions with an energy of approximately 0.5 MeV/u. In order to align the decelerated ions through the RFQ, two iris diaphragms are installed at the entrance and exit of the cavity. With the diaphragms closed to about 3 mm diameter, the ion signal is optimised.

Once the ion beam is aligned to the centre of the RFQ, deceleration of the ions can commence. In a similar manner to the IH-structure, the RF phase and amplitude must be optimised, although former commissioning campaigns indicate that the amplitude is relatively insensitive and decel-
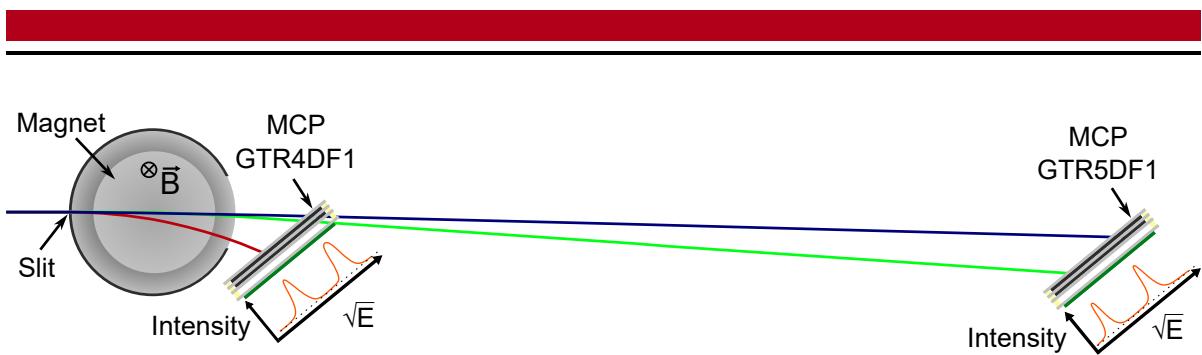
Figure 4.5: Separation of the energy components after the RFQ. The magnet of the energy analyser (GTR4EF1) inside the diagnostic chamber GTR4DK1 is combined with the MCP detector in the same vacuum chamber (GTR4DF1) to separate the fully decelerated ions (red). To distinguish between the ions coming from the IH with 4 MeV/u (blue) and 0.5 MeV/u (green), the magnet is combined with the on-axis MCP detector (GTR5DF1) in the next diagnostic chamber. This allows for guiding the 0.5 MeV/u beam through the RFQ prior to deceleration.

eration is feasible across a broad range of settings [140].

Following the RFQ, the ion signal is observed with the energy analyser in GTR4DK1 in order to separate the decelerated ions from the primary beam. The signal obtained from this detector is shown in the right frame of Fig. 4.6. On the top of the detector, a portion of the primary beam is visible, although the majority of the primary beam hits the frame of the detector. Only the thin line situated in the centre of the detector is indicative of ions that have undergone complete deceleration. It is important to note, that the signal of the decelerated ions is highly unstable at this point and is likely created by only a few ions. The substantial background signal observed across the entire detector is a consequence of the exceedingly high amplification voltage of 1.7 kV applied to the microchannel plates. This value approaches the breakdown voltage of the detector. In the small region on the bottom-left side of the detector, the frame blocks the camera's view, causing the impression of a background-free area. In comparison to the results from the last beamtime in 2014 presented in [21], both the stability and amplitude of the signal are significantly reduced. It is unclear whether this is due to a reduction in deceleration efficiency or to issues with the energy analyser. In preparation for the forthcoming beamtime, plans are in place to redesign both the diagnostic chamber and the energy analyser. This will include the commissioning and calibration with the local EBIT as an ion source, which will allow for more extensive testing of the setup aside from the very limited beamtime with ions provided from the ESR. Additionally, the rebuncher attached to the exit of the RFQ will be temporarily removed, as it has so far not been required for further transport and storage following the RFQ. This will free more space in the newly designed diagnostic chamber, allowing for more flexibility in positioning the currently installed magnet, MCP detector and einzel lens.

### 4.2.3 LEBT

Given the weak signal from the energy analyser, it is not possible to achieve a precise optimisation of the RFQ. Consequently, the ions are transported further along the beam line. It is noteworthy, that this step was never attained in any of the preceding 19 beamtimes before the one in April 2024.

In a first attempt, the decelerated ions were searched for in the first diagnostic chamber of
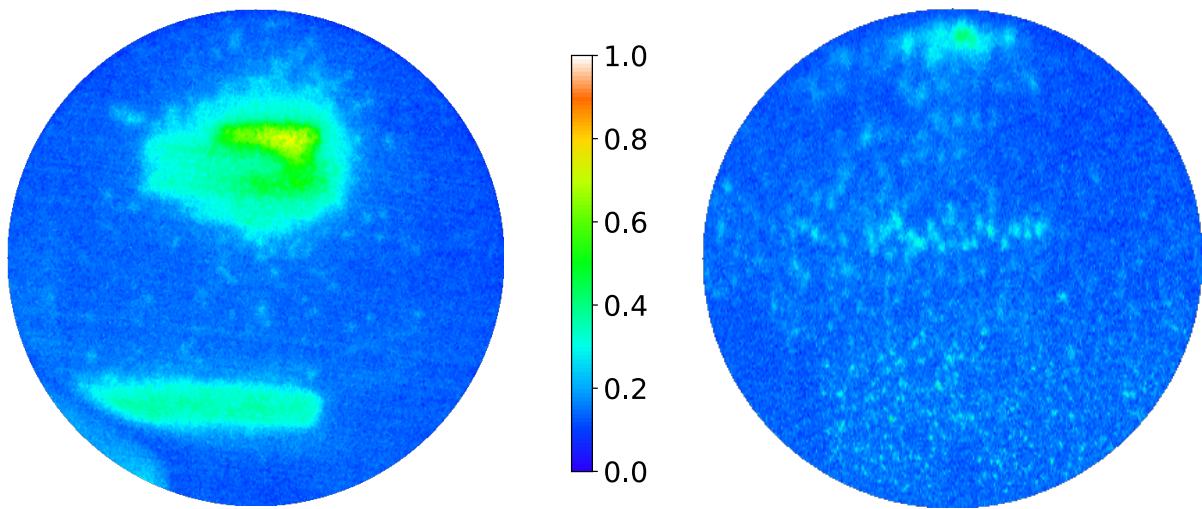
Figure 4.6: Left: energy separation of the IH-structure output subsequent to the RFQ. The ions are separated by the energy analyser magnet situated behind the RFQ (GTR4EF1) and detected by the on-axis MCP detector GTR5DF1 in the subsequent diagnostic chamber. At the bottom of the image, ions with an energy of approximately 0.5 MeV/u are visible. This signal is employed to align the beam through the RFQ. Right: energy separation of the RFQ output separated by the energy analyser magnet and observed with the MCP detector in the the same chamber (GTR4DF1). On the top of the screen, a small part of the primary beam is detected, and in the central region a faint horizontal line of decelerated ions is discernible. The colour scale indicates the relative intensity.

the low-energy beam transport line (GTR5DK1). For this purpose, an off-axis MCP detector is installed, which is designed to deflect the ions with an energy about 6 keV/u by an electrostatic potential onto an MCP detector that is mounted parallel to the beam axis (see Sec. 3.2.8 for details), while the primary beam passes the setup without being affected. It was found that this design was ineffective for the detection of decelerated ions due to the presence of a high background induced by the primary beam.

The next possibility of separating the low-energetic ions from the primary beam is in the subsequent diagnostic chamber GTR5DK2, where also an off-axis MCP detector is installed. At this point, the background signal induced by the primary beam is negligible. These enhanced conditions allow for the identification of a signal that corresponds to ions with a kinetic energy of some few keV/u. Both the time-of-flight towards the detector and the sensitivity to parameters such as the RFQ's phase and amplitude exclude the possibility of a signal induced by non-decelerated ions. Nevertheless, even after optimisation of the beam-guiding elements, the signal remains significantly fluctuating in strength. This behaviour is visualized in Fig. 4.7, where the measured ion signal is plotted over several subsequent injections.

For the first eight injections, the observed instabilities are of the order of about ±25 %. It appears that an unidentified event may have occurred between injections eight and nine, resulting in a sudden increase in signal strength by approximately a factor of two. From there on, the fluctuations between consecutive injections are similar to those observed prior to the event but at a higher baseline level. Monitoring of the beam-guiding elements along the HITRAP beam line, revealed no significant instabilities, indicating that the observed fluctuations are likely at-
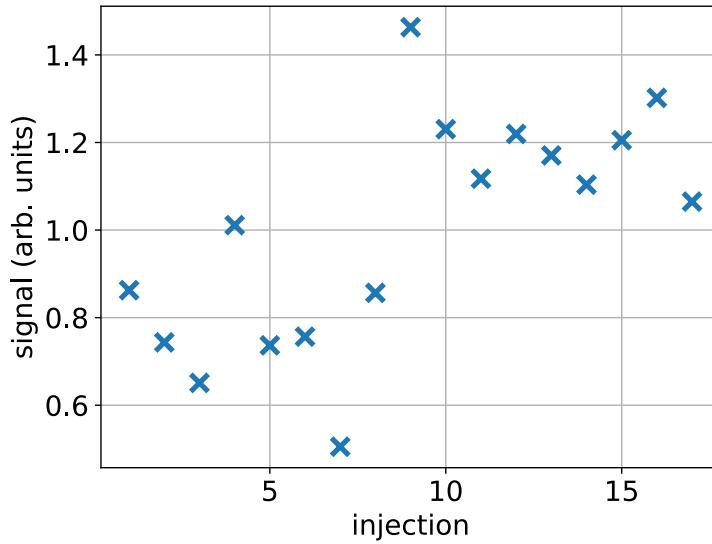
Figure 4.7: Signal of decelerated ions, as measured at the off-axis MCP detector in GTR5DK2, plotted against the number of injections.

tributable to the RF-machines. It seems probable that either the deceleration efficiency inside the RFQ is unstable or that the already discussed issues of the IH-structure are causing minor fluctuations in either the output energy or trajectory, thereby preventing a reliable operation of the RFQ.

Although the signal detected at GTR5EF2 is not perfectly stable, it can be employed for the optimisation and characterisation of both the rebuncher GTR3BB3 and the RFQ. In a first measurement, the phase and power of the buncher is scanned while monitoring the signal on the MCP detector. In order to compensate for the aforementioned signal fluctuations, the signal is averaged over seven consecutive injections for each data point.

The results of this measurement are presented in Fig. 4.8, where the averaged signal is plotted over the phase (left) and power (right) of GTR3BB3. In the phase scan, conducted at a power of 1.0 kW, a plateau is observed in the region between 350° and 15°, where the signal remains constant within the error margins, with the exception of 10°. It is probable that this outlier is of a statistical nature and not indicative of an optimal setting of the bunching phase. A comparison of these results with those presented in Sec. 4.2.2, in which the phase without acceleration is observed to be 0°, demonstrate a good agreement with a slight shift towards a phase that causes a small deceleration of the ions. As the output energy of the IH-structure (489±3 keV/u), determined in Sec. 4.2.1, is also slightly higher than the centre of the energy distribution accepted by the RFQ (485±10 keV/u), a small amount of deceleration within the buncher might indeed increase the deceleration efficiency in the RFQ as indicated by the measured data.

The efficiency of the buncher exhibits a maximum at a power of 0.8 kW, although it is also possible that this maximum can again be attributed to statistical fluctuations. The data indicate that the buncher operates effectively at power settings between 0.5 and 0.95 kW. This finding aligns with expectations, as a buncher of this scale is likely to have a minimal impact on the ion beam. However, it serves as a valuable tool for enhancing the deceleration efficiency in the RFQ, as intended.
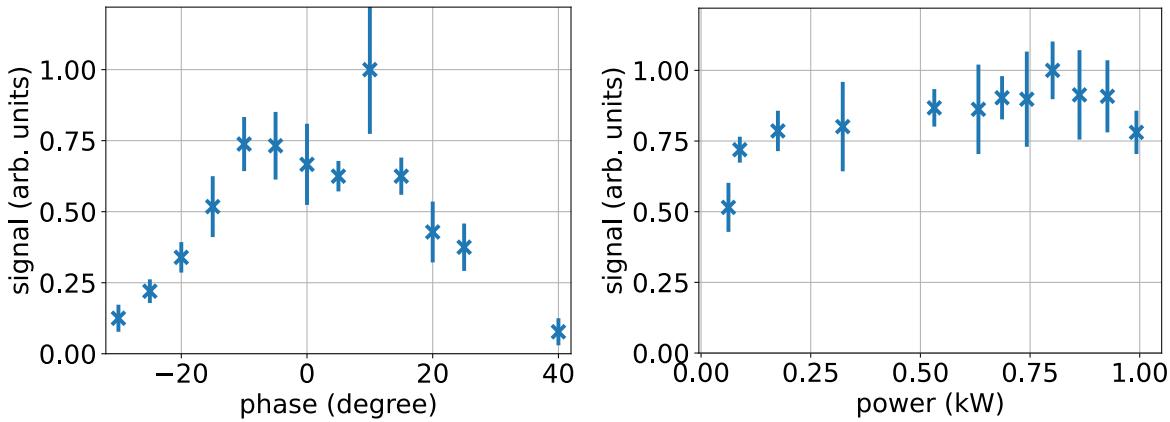
Figure 4.8: Left: ion signal after deceleration in the RFQ plotted over the phase of the rebuncher GTR3BB3 at a power of 1 kW. Right: ion signal after deceleration in the RFQ plotted over the power of the rebuncher GTR3BB3 at a phase of 5°.

Similar measurements are conducted for the RF settings of the RFQ, whereby the phase and power are also scanned, with the buncher set to 0.8 kW and 5°. In Fig. 4.9, the observed signal, again averaged over seven injections, is plotted over the RFQ's phase (left) and power (right). In the phase scan, a plateau of constant signal, within the limits of the measurement uncertainty, is observed in the region between 70° to 90°. The signal exhibits a rapid decline on either side of the plateau. This behaviour was also observed in previous beamtimes in 2022 and 2014, where decelerated ions could only be observed at the energy analyser for a narrow range of phase values.

The scan of the RF power demonstrates a consistent increase in signal strength with rising power, reaching a maximum at 59 kW. Upon further increase of the power, a slight decrease in signal intensity is observed. However, this can also be interpreted as a constant behaviour within the measurement uncertainties. At a power setting of 32 kW and below, deceleration of the ions is no longer possible. These results are in excellent agreement with the data obtained during the initial commissioning of the cavity at the Max Planck Institute for Nuclear Physics (MPIK) in Heidelberg, where a very similar progression was observed [140].

Despite the fluctuating signal, the data acquired with the MCP detector at the second diagnostic chamber in the low-energy transport line allows for a first characterisation of the buncher GTR3BB3 and RFQ. As this point of the beam line could not be reached in previous experimental runs, this is the first extensive investigation of these RF-structures when operating at their designated task with ions from the GSI accelerator. However, it should be noted that the extracted values can only serve as a reference point for further commissioning in future beamtimes. Given the very limited time available for data acquisition and the low repetition rate of ion injection, the statistical significance of the results remains relatively low for a signal exhibiting such pronounced fluctuations. Further investigations of these crucial parameters for the commissioning of the HITRAP decelerator are subject of the campaigns planned for 2025.
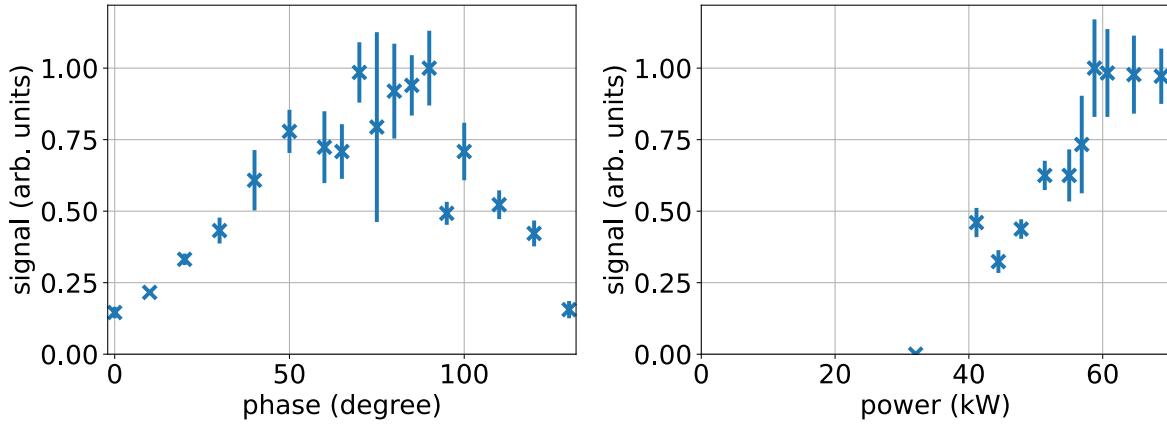
Figure 4.9: Left: ion signal after deceleration in the RFQ plotted over the RF phase at a power of 61 kW. Right: ion signal after deceleration in the RFQ plotted over the RF power at a phase of 89°.

## 4.3 Storage in the Cooling Trap

Following the successful deceleration in the HITRAP linear decelerator, the next and final step for highly charged ions on their way towards experiments is the storage and preparation within the Cooling Trap. There, the ions are supposed to be cooled by a simultaneously stored cold electron plasma, before they can be provided to subsequent experiments.

In order to capture the decelerated ion bunch, first, the ions must be transported through the setup and detected at the first MCP detector after the trap in GTR6DK1. The resulting signal over time is depicted in Fig. 4.10 in green. The time-value is related to a trigger transmitted from the GSI internal timing system, White Rabbit [173], during the extraction process in the ESR. The precise timing of the trigger is inconsequential, only the fact that its jitter is negligible small is essential, allowing for the capture process to be reproducibly timed.

Two distinct peaks are discernible, clearly separated in time. Significantly more dominant is the signal induced by ions that are either not at all or only partially decelerated by the IH-structure and RFQ (light green). The second and weaker peak (dark green) comprises ions with the desired energy of approximately 6 keV/u, which arrive about $4.5\,\mu$s later than the primary beam. The signal acquired by GTR5EF2 in front of the trap (blue) is also included in Fig. 4.10 in order to extract more detailed information about the timing and energy of the decelerated ions. As only the low energy components are deflected by the electrostatic potential onto the off-axis MCP, the primary beam is not visible here. The two peaks of decelerated ions are fitted with a Gaussian distribution (red) in order to extract their centre positions, which are listed in Tab. 4.4 together with their Gaussian widths $\sigma$, which corresponds to the full width at the point where the signal is reduced by $1/\sqrt{e}$.

A comparison of the positions of the decelerated ions provides valuable information for capturing the ion bunch in the Penning trap. On the one hand, the timing can be roughly extracted, given that the trap is situated in the middle of the two detectors. Therefore, the ions will be inside the Penning trap at the time $t \approx 9.2\,\mu$s and the switching of the capture electrode can be adjusted accordingly. The trapping scheme will be discussed in the next section in greater detail.

Moreover, the mean kinetic energy of the ion bunch can also be extracted. The distance between the two detectors, GTR5EF2 and GTR6EF1, is $(3033\pm20)$ mm. Neglecting effects like deviations
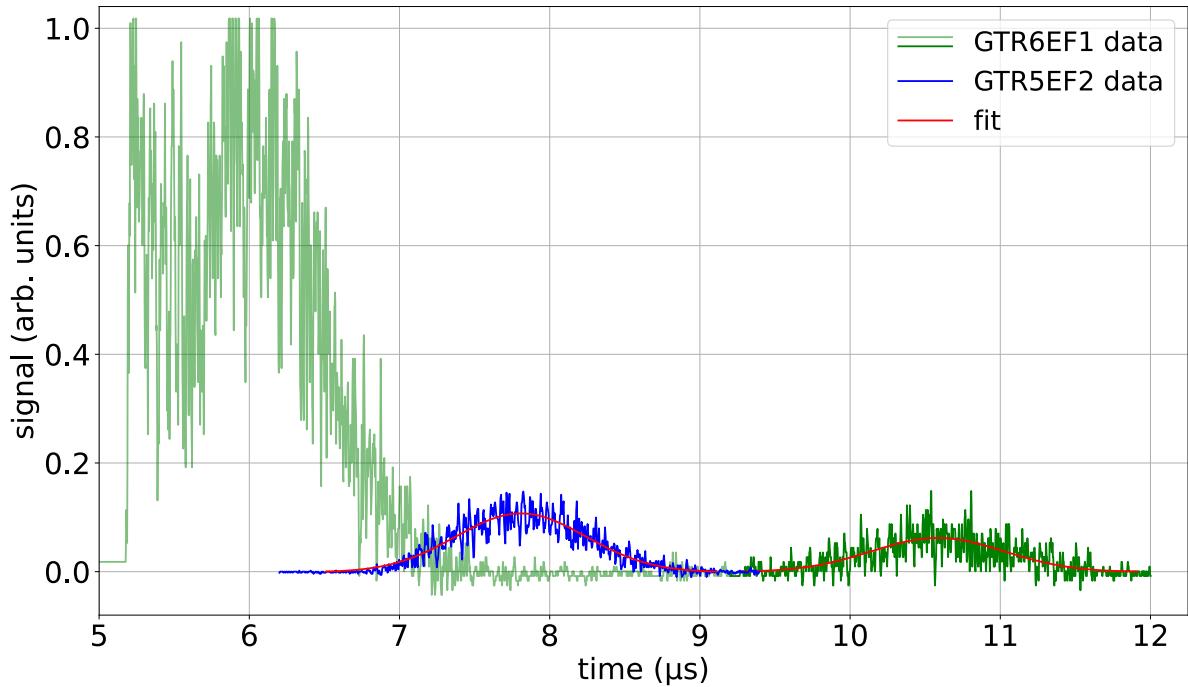
Figure 4.10: Detected ion signal in front (GTR5EF2, blue), superimposed with the signal observed behind (GTR6EF1, green) the Cooling Trap, plotted over time. The signal induced by the primary beam is displayed in a lighter colour to separate it from the signal of interest, corresponding to the decelerated ion bunch. The two peaks of decelerated ions are fitted by a Gaussian distribution, and the timing information extracted from these fits is listed in Tab 4.4. Shape and length of the peaks correspond to those of the bunch coming from the ESR.

Table 4.4: Timing information of the decelerated ion beam in front of (GTR5EF2) and after (GTR6EF1) the Cooling Trap. The values are extracted from the Gaussian fit displayed in Fig. 4.10

| detector | position (µs) | $\sigma$ (µs) |
|---|---|---|
| **GTR5EF2** | 7.818±0.002 | 0.433±0.002 |
| **GTR6EF1** | 10.583±0.006 | 0.443±0.006 |

from the ideal path due to deflections by the beam guiding elements or the radial motion of the ions inside the strong magnetic field of the Cooling Trap, this distance, combined with the time-of-flight of $t = (2.765\pm0.006)$ µs between the detectors, yields the velocity of the ions. Accordingly, the centre of the energy distribution can be calculated using Eq. 4.1 to $(6.28\pm0.09)$ keV/u or $(12.57\pm0.17)$ keV/$q$ for the employed isotope $^{36}\text{Ar}^{18+}$ with a mass to charge ratio of 2.

This result aligns with a qualitative measurement conducted during the beamtime, in which the potential of a capture electrode is gradually increased until the ions are reflected by the retarding field. During this measurement, the signal begins to decline at a potential of 12 kV and is almost entirely blocked with 14 kV applied, corresponding to an energy distribution of 12-14 keV/$q$ or 6-7 keV/u, respectively. These results also agree with those of earlier measurements employing a spherical electrostatic energy analyser, which also yielded an energy of 6-7 keV/u [21].

### 4.3.1 Trapping scheme

With the ions guided through the Cooling Trap, the next step is to capture the ion bunch, taking into account the estimated timing and energy. In order to reflect ions with a kinetic energy $E_{\text{kin,i}}$ of up to $14\,\text{keV}/q$, a capture potential of at least $14\,\text{kV}$ is required. An operation with a potential so close to the ions' energy would likely result in unstable trapping conditions; therefore, the availability of even higher potentials is desired. As outlined in Sec. 3.2.5, it is imperative that the maximum potential difference between two neighbouring trap electrodes does not exceed $10\,\text{kV}$. It is thus also necessary to apply a potential $U_{\text{ref,i}}$ to the trap ground, thereby simultaneously applying it to all trap electrodes and mounting structures. In this configuration, the ions are decelerated upon entering the trap as they must overcome the positive potential. Consequently, within the trap, ions with charge $q$ possess a diminished kinetic energy and propagate at a reduced velocity. The kinetic energy $E_{\text{kin,t}}$ of the trapped ions can then be calculated using the equation

$$E_{\text{kin,t}} = E_{\text{kin,i}} - qU_{\text{ref,i}}. \tag{4.5}$$

In addition to fulfilling an electrical restriction of the setup, the technique of decelerating the ions upon entering the trap also has the advantage of compressing the ion bunch in the longitudinal direction. This results in a higher ion density, thereby facilitating the capture of additional ions, that would otherwise exceed the volume of the trap. If the remaining kinetic energy per charge is less than the potential applied to the capture electrode, the ions can now be captured by also switching the second capture electrode to a confining potential.

In a next step, the kinetic energy of the ions can be manipulated. While the width of the energy distribution can only be reduced during the storage process by applying cooling techniques such as electron cooling, the mean kinetic energy of the captured ions can be adjusted during the injection process as described above. By modifying the offset potential during the storage period, the kinetic energy after extraction can also be arbitrarily chosen. The final kinetic energy $E_{\text{kin,f}}$ is then given by

$$E_{\text{kin,f}} = E_{\text{kin,t}} + qU_{\text{ref,f}} = E_{\text{kin,i}} - q(U_{\text{ref,i}} - U_{\text{ref,f}}), \tag{4.6}$$

with the reference potential at time of extraction $U_{\text{ref,f}}$. An increase in potential results in a higher kinetic energy, whereas a decrease leads to an effective reduction in energy.

The optimal approach would be to simultaneously ramp down both power supplies with the same ramp rate. At this point, this is not yet technically feasible with the current setup, although the therefore required upgrade of the electrical setup is foreseen. For the last beamtime this means a step-wise ramping of both the capture and reference potentials in order to guarantee that neither the maximum potential difference is exceeded nor that the ions are lost during the process.

In Fig. 4.11 the trapping scheme is schematically visualised and the therein depicted steps are described in the following in more detail:

- In preparation for the arrival of the ion bunch, all trap electrodes are set to a reference potential, and the far side capture electrode is additionally set to a reflective potential $U_{\text{cap}}$.

- The ions enter the trap and are reflected at the capture electrode (step 1).

- Before they can leave the trap volume again, the second capture electrode is also switched to a high potential (step 2).
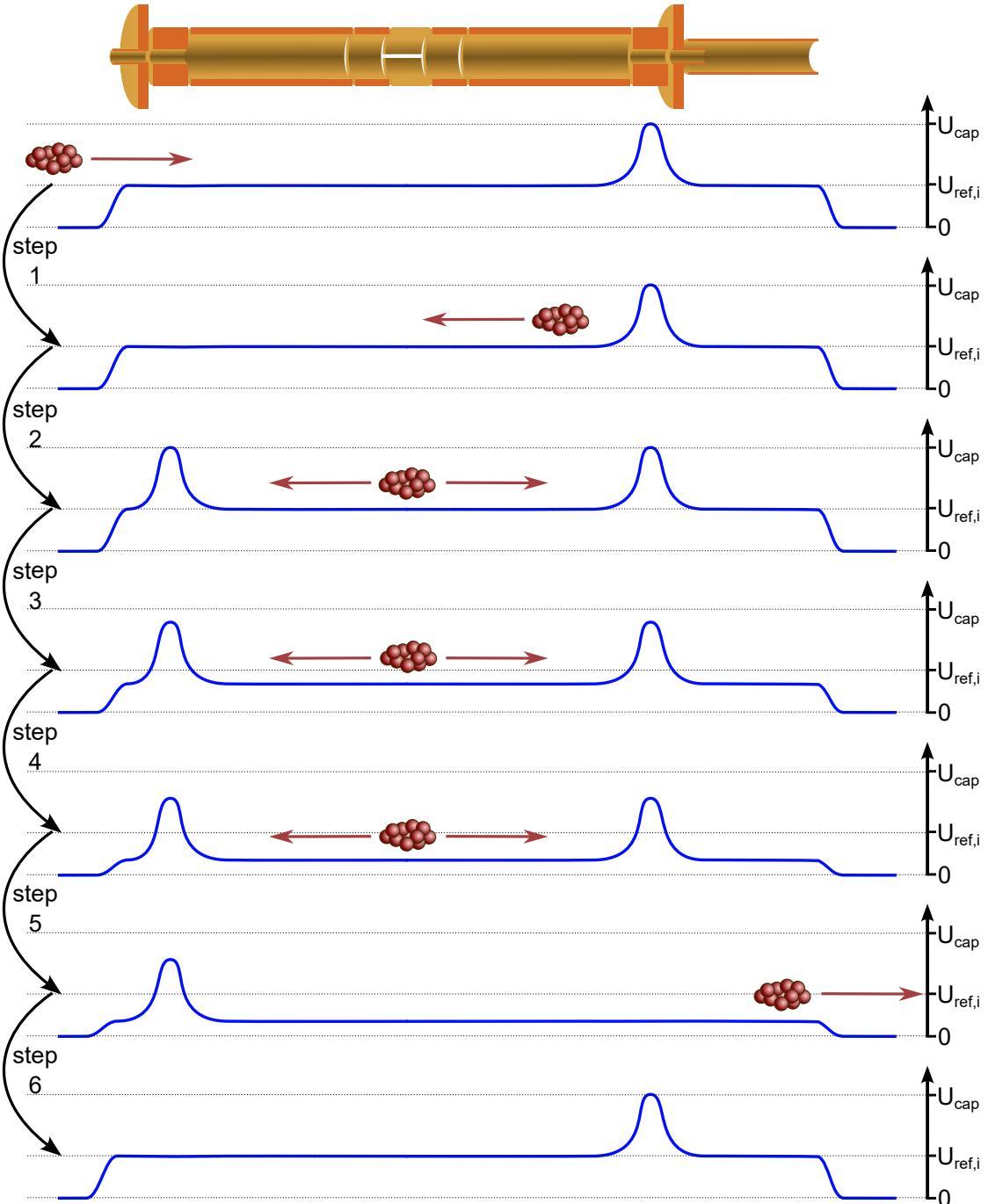
Figure 4.11: Trapping scheme for the capture process of accelerator-produced ions. The ions are arriving from the ESR and are captured between the capture electrodes of the Penning trap (step 1 and 2). While the ions are trapped, the extraction energy can be set by changing the reference potential (step 3 and 4). After the storage time, the ions are ejected towards the experiment (step 5) and the trap is prepared for the next ion injection (step 6).

- Both the capture and the reference potentials are reduced by the same amount in a step-wise manner, the kinetic energy of the stored ions remaining unchanged throughout this process (step 3 and 4). The interval between two successive stages of potential ramping is dominantly determined by the ramping speed of the power supplies and switches. In contrast to the fast switches connected to the capture electrode, which change the potential in a negligible time of about 100 ns, the ramping of the power supply for setting the reference potential takes about 1 s per step, depending on the potential difference. For tests and measurements, that do not require a change of the extraction energy, steps 3 and 4 can be omitted, thereby allowing for a reduction of the minimum storage time that is otherwise limited to 2 s.

- To eject the ions, the far side capture potential is lowered and the ions are no longer confined and can leave the trap volume (step 5). In this example, a small reference potential is still applied, resulting in an acceleration of the ion bunch.

- Finally, the initial values are restored in preparation for the next injection of ions (step 6).

### 4.3.2 Storage Results

In the initial attempt to capture and eject the decelerated ion bunch, a simplified version of the above presented trapping scheme is employed. The kinetic energy of the ions is not changed in this case, therefore step 3 and 4 in Fig. 4.11 can be skipped, allowing for the storage time to be set to only 100 ms. In accordance with the results of the energy measurement presented in Sec. 4.3, which yields a kinetic energy in the range of 12-14 keV/$q$, the potential of the capture electrode is set to 15 kV above ground potential. This necessitates that a reference potential of at least 5 kV is applied, in order to ensure that the limitation for the maximum voltage between two neighboring electrode is not exceeded. To leave a greater safety margin towards this limit, and also to benefit from additional longitudinal compression of the ion bunch, the reference potential is set to 9 kV.

The trigger for the fast high-voltage switch of the left capture electrode is set for this first test to be $9.5 \mu s$ after the extraction trigger from the ESR. This is $0.3 \mu s$ after the above calculated time, which corresponds to the expected arrival time of the ion bunch at the trap centre. This time shift is intended to account for the deceleration of the ions within the trap and the time required for the ion bunch to reach the far side capture electrode, which represent the theoretically ideal point for switching the other capture electrode.

In Fig. 4.12, the result of this first attempt at trapping accelerator-produced highly charged ions within the HITRAP Cooling Trap is presented. The signal from the on-axis MCP detector situated after the trap (GTR6EF1) is plotted over time. The time axis is relative to the trigger sent to the right capture electrode, which corresponds to the time of extraction. After $0.5 \mu s$, electrical noise is visible induced by the rapid switching of the electrode from 15 to 9 kV. The ion signal is observed to commence after a time-of-flight of $1.90 \mu s$, subsequently declining to a level approaching that of background after $3.26 \mu s$. In subsequent tests, the reference potential is modified during the storage period, thereby reducing the kinetic energy of the extracted ions. This becomes observable in the ion signal, as the arrival time is delayed when reducing the kinetic energy, proving that the energy of the ejected ions can be arbitrarily chosen by the operator.

The bunch length of $(1.36 \pm 0.02) \mu s$ is determined by the velocity of the ions inside the trap, i.e., their kinetic energy, and the length of the Penning trap, and is therefore independent of any
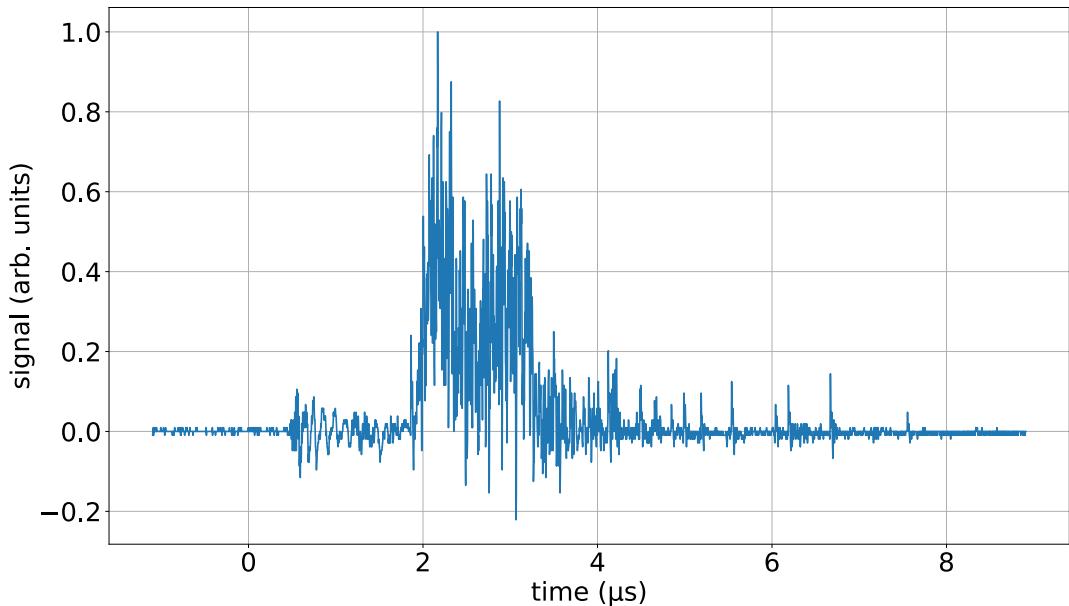
Figure 4.12: First signal of trapped accelerator-produced ions after ejection from the Cooling Trap. The ions are stored for 100 ms and detected by the MCP detector in GTR6DK1.

changes in the reference potential. During the storage time, the ions interact with one another via Coulomb interaction and elastic scattering, which causes the initial bunch shape to transform into an equal distribution across the entire length of the trap. The first ions leaving the trap during the ejection process are located in close proximity to the right capture electrode at the moment of switching and are moving towards the detector. Conversely, the last ions are also located in close proximity to that electrode, but are moving in opposite direction, away from the detector. It thus follows that these ions must traverse an additional distance of twice the trap length. With the calculated centre value of the energy distribution, $(12.57\pm0.17)$ keV/$q$, and taking into the account the reduction of kinetic energy by $9$ keV/$q$ during the capture process, this yields an expected bunch length of $(1.32\pm0.04)$μs, which is in excellent agreement with the measured value.

As the ion signal is acquired by an MCP detector, it is not possible to provide an exact number of stored and detected ions. A comparison of the signal with measurements performed with the local EBIT ion source yields an estimated $10^4$ ions. Following the main signal, a residual, gradually diminishing signal persists, which is also likely attributable to trapped ions. The reason for this unusually long 'tail' is, as yet, unclear. One potential explanation is that the remaining signal is composed of single argon ions that have transferred the majority of their kinetic energy to other ions or to the residual gas via Coulomb interaction or elastic scattering. Alternatively, the signal is produced by ionised residual gas particles that are created at a low kinetic energy inside the trap and then accelerated by the reference potential upon leaving the trap.

This naturally gives rise to the question of whether the observed signal is in fact induced by argon ions in the first place or whether it is entirely composed of ionised residual gas. In this case, it could be attributed to one of two potential causes. Firstly, the rapid switching of the
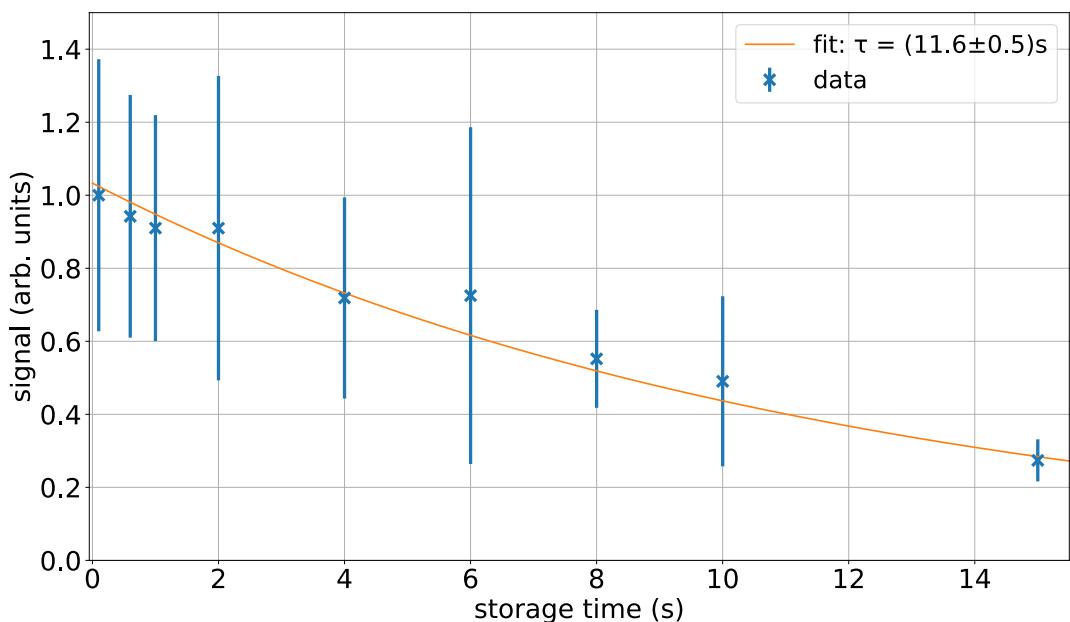
Figure 4.13: Ion signal plotted over various storage times. By fitting an exponential decay to the data points, the particle lifetime of the $^{36}$Ar-ions in the trap is calculated to (11.6±0.5) s.

capture electrodes over a potential difference of 6 kV can result in the ionisation of residual gas particles, which are subsequently captured within the trap. This hypothesis can be discarded, as the blocking of the argon beam by a Faraday cup prior to reaching the trap while maintaining the same trapping scheme with the capture electrodes, resulted in a complete disappearance of the signal.

Alternatively, the residual gas is ionised by the passing high-energy primary beam. In this case, the width of the signal's main part should not align with the geometrical expectations for ions at the given energy, stored in a volume with the length of the Penning trap, as discussed above. Furthermore, the signal should then be relatively independent of trap settings, such as the applied potentials or the timing delay for switching the capture electrode, particularly if the delay is reduced. Additionally, when the ionisation of residual gas was observed during the commissioning of the HITRAP Cooling Trap with locally produced ions, the signal consistently increased with the storage time, i.e., the longer the ions are stored, the higher the detected signal becomes.

Subsequently, further measurements are conducted to substantiate the hypothesis that the signal is constituted by argon ions. Furthermore, following this first proof of principle, the capture and storage process is further investigated by measuring the lifetime of the stored ions and optimising the dependencies on the applied potentials and switching time for the capture electrode.

The lifetime inside the Penning trap, as defined in Eq. 2.62, is also an important indicator of the stability of the setup and the vacuum conditions inside the trap. It can be measured by varying the storage time while observing the ion signal after the trap. The result of such a series of measurements is depicted in Fig. 4.13, in which the integrated ion signal is plotted against the storage time. For each data point, the ion signal of ten consecutive injections is
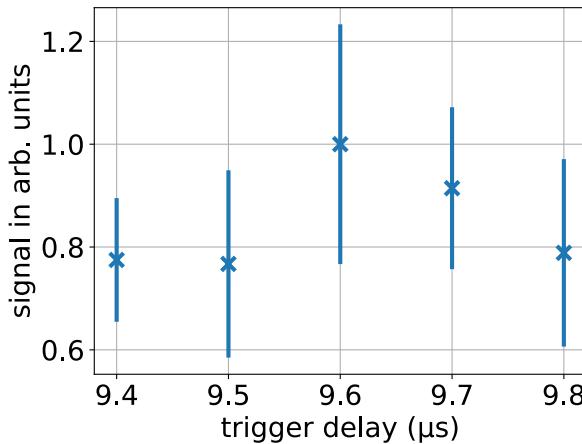
Figure 4.14: Signal of stored and then ejected ions plotted over various trigger delays for switching the left capture electrode. The settings for the reference and capture potentials are 9 kV and 15 kV, respectively.

averaged and then integrated over the length of the main part in order to extract a value that is, in first approximation, proportional to the number of ions. The provided error bars represent the 1-sigma statistical uncertainty of each data set.

As anticipated for the storage of externally produced ions without ionisation of the residual gas, the measured signal declines with increasing storage time. By fitting an exponential decay function to the data, the lifetime $\tau = (11.6\pm0.5)$ s can be extracted from the fit parameters. It is important to highlight, that this lifetime represents the lifetime of a particle, and that the detected ion signal comprises a mixture of various charge states. As discussed in Sec. 2.2.6, it is necessary to differentiate between this lifetime and the lifetime of a charge state. The majority of experiments require a specific charge state; therefore an ion is already considered lost if it undergoes charge exchange. Given the available data, it is not possible to separate individual charge states in the signal, thereby precluding a determination of the charge state lifetime. Nevertheless, these results demonstrate that it is feasible to maintain the stable storage of accelerator produced ions over an extended period of time.

In order to prepare further measurements and to investigate the dependencies of the trapping process on potential settings or the timing, these parameters are varied while the ion signal is observed after a constant storage time of 1 s. In order to enhance the statistical reliability of the results, the signal is integrated after averaging five consecutive injections. Firstly, the optimal time for switching the left capture electrode is determined, as visualised in Fig. 4.14. For unchanged capture and reference potentials of 15 and 9 kV, respectively, the delay for the trigger, which is sent to the switching unit connected to the left capture electrode, is varied. The data indicate a maximum at a delay of $9.6\,\mu$s. This agrees with the results of the discussion presented in the beginning of this section, wherein the calculated delay is expected only marginally lower, at $9.5\,\mu$s.

Similar measurements are performed, in order to optimise the capture and reference potentials. In the left panel of Fig. 4.15, the capture potential is varied while maintaining a fixed switching delay of $9.6\,\mu$s and a reference potential of 9 kV. On the right-hand side of the figure, the reference potential is the variable, with the switching delay remaining unaltered and a capture potential
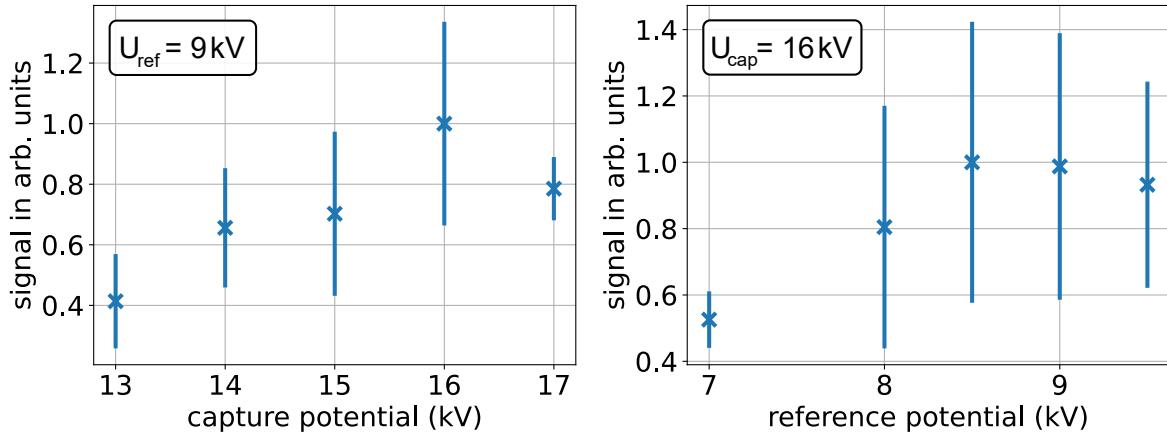
Figure 4.15: Optimisation of the reference and capture potential. Left: signal of stored ions over the potential applied to the capture electrodes for a reference potential of 9 kV. Right: signal of stored ions over the reference potential of the trap, while the capture potentials are set to 16 kV. The trigger delay for switching the left capture electrode is fixed for both measurements at $9.6\,\mu s$ as determined in Fig. 4.14.

of 16 kV. With regard to the capture potential, a maximum at 16 kV is observed, whereas the reference potential exhibits a plateau for values between 8.5 and 9.5 kV. In the case of the reference potential, the data can be explained, at least in part, by the constant trigger delay. The velocity of the ions within the trap setup is affected by the reference potential, which in turn necessitates an adjustment of the trigger delay for optimal capture conditions. While the increased longitudinal compression for higher reference potentials reduces the sensitivity of the ion signal to the trigger delay, for lower potentials an optimised setting of the delay becomes more important. This is also supported by the data, as the signal intensity is significantly reduced for the lowest reference potential of 7 kV.

Given the considerable fluctuations in the ion signal, the limited number of measurements, and the therefrom emerging large uncertainties, these results must be treated with caution. This is particularly the case with regard to the measurement concerning the trigger delay for switching the capture electrode, where all values lie within the given uncertainties of each other. Conversely, these findings demonstrate the robustness of the apparatus, as the initial capture of ions is feasible across a broad range of settings, thereby facilitating the capture process and subsequent optimisation. In order to make a definitive statement regarding the optimal settings for capturing the ion bunch, it is necessary to collect more data in future beamtimes.

## 4.4 Conclusion

After an eight-year long period of standstill, the HITRAP linear decelerator could be recommissioned in 2022 to the same point as in the last campaign in 2014. This involved the deceleration of highly charged ions from 4 MeV/u down to approximately 6 keV/u. While the progress of the first of the following two commissioning campaigns in 2024 was limited due to an unsatisfactory performing IH-structure, the second run proved highly successful, marking the first significant advancement in the last ten years.

A preliminary qualitative investigation was conducted to assess the of impact the rebuncher between the IH-structure and the RFQ on the deceleration efficiency. Although the value of the RF power appears to be relatively insensitive, a careful optimisation of the phase is imperative for an efficient deceleration in the RFQ, as a mismatch leads to a change in the ions' kinetic energy and consequently results in the ions falling outside the acceptance range of the RFQ. Similar measurements were conducted regarding the RF settings of the RFQ, confirming the initial tests performed at the MPIK, where the RF-cavity was redesigned and tested in 2012 [140].

Despite some time-costing difficulties in detecting completely decelerated $^{36}$Ar$^{18+}$-ions after the RFQ, within the short remaining period of only three days, the ions were not only transported further along the beam line. For the first time it was possible to capture and eject accelerator-produced highly charged ions in a Penning trap, a world-wide unique achievement. Some preliminary measurements were conducted, which contributed to a deeper comprehension of the capture process, facilitating this step in future campaigns. Ultimately, a hardware failure in the form of a leaking vacuum bore in the Cooling Trap and what is assumed to be an unidentified disturbance by the off-axis MCP detector design, prevented an even bigger leap forward, as electron cooling could unfortunately not be tested in the last beamtime and remains as the next major objective for future runs.

These last three commissioning campaigns not only demonstrated a significant progress in the commissioning process, but also revealed several issues that must be addressed to fully utilise the capabilities of the HITRAP facility. The two principal construction sites are of course the IH-structure and the Cooling Trap. During the second of three beamtimes presented here, in February 2024, it was not possible to achieve a reliable deceleration of $^{18}$O$^{8+}$ with a mass-to-charge ratio of 2.25, as the required power could not be delivered on a stable basis. The deceleration of heavy HCI, which HITRAP was originally designed for, is in this state far out of reach due to the fact that significantly higher RF power is needed for deceleration of isotopes with larger $m/q$ ratios, like bare uranium with a ratio of 2.55. Furthermore, the observed maximum deceleration efficiency of only 23 % is unsatisfactory in comparison to the previously achieved 50 % in 2014 [21]. At the time of writing this work, it remains unclear whether the issues stem from the cavity itself or the accompanying RF-source and amplifier.

As the second significant obstacle to the operation of the HITRAP facility, the leakage in the Cooling Trap was already identified and fixed in the months following the last beamtime. The setup is again in operation with ions produced by the local ion source. In addition to the afore-mentioned major hardware failures, there are several improvements under discussion or already in construction. The most important of these are a redesign of the diagnostic chamber following the RFQ to facilitate the detection of decelerated ions and an extensive investigation into the potentially problematic design of the off-axis MCP detectors.

In the event of a successful repair and operation of the IH-structure, three beamtimes are sched-uled for 2025, including the very first experiment, which will investigate the surface ionisation capabilities of gold ions with a kinetic energy of 6 keV/u. The two additional commissioning cam-paigns will be primarily concerned with demonstrating electron cooling of accelerator-produced HCI and the subsequent transport of decelerated and cooled ions along the beam line. This will also include the transport through a magnetic bender, allowing for charge separation and therefore a lifetime measurement of a certain charge state within the beamtime.

# 5  Electron Cooling of Highly Charged Ions

After the development of the first Penning trap design in 1959, the cooling of stored particles rapidly became a widely used technique to enhance the precision of experimental results [174–176]. The first employed cooling techniques included resistive cooling [177] and laser cooling [178], both of which remain in use in high-precision experiments on a regular basis. However, given the characteristics of the ions present at HITRAP, namely their high kinetic energy and its broad distribution, neither resistive cooling nor direct laser cooling are viable as an initial step in the Cooling Trap. Instead, sympathetic cooling remains as the only eligible alternative as HITRAP is designed for highly charged ions. This technique was already established with $Mg^+$ ions at the SPECTRAP experiment located at HITRAP [17, 89]. For sympathetic cooling with ions, a laser cooling system is required, so an alternative approach with electrons is selected for the Cooling Trap.

Thus far, sympathetic cooling with co-trapped electrons in a Penning trap has only been observed on either very light [95] or singly charged ions [96]. At HITRAP, the development of the Cooling Trap towards the application of electron cooling on highly charged ions commenced with the first design in 2005. In 2011, the independent storage of locally produced ions and electrons, respectively, was achieved for the first time in the setup. At this time, the lifetime of the trapped particles was observed to be only in the order of $100\,\mu s$. Only after an improved alignment of the magnetic field, this value could be significantly increased to more than 1 second. [33, 167]. Shortly after that, a shift in priorities towards the newly established CRYRING@ESR storage ring slowed the commissioning process down. The only significant advancement in the following years was a complete redesign of the Penning trap, in order to replace the original electrode stack, which was highly prone to errors [145].

This chapter presents the recent developments in the commissioning process of the new trap design, with the ultimate objective of electron cooling on highly charged ions. In order to demonstrate electron cooling, a deeper understanding of both ingredients, i.e., the electron plasma and the ion bunch is required.

In Sec. 5.1, the creation and properties of the electron plasma are discussed, as well as a technique that employs the stored electrons to improve the alignment of the magnetic and electric fields in the Penning trap. This is followed by Sec. 5.2 in which the trapping and characterisation of highly charged ions produced by a local EBIT ion source is presented. These two sections prepare for a final discussion of the observations from simultaneously storing electrons and ions within the HITRAP Cooling Trap in Sec. 5.3, which includes the world-wide first proof of electron cooling of highly charged ions. The chapter then concludes with an overview of the remaining steps in commissioning the setup.

## 5.1 Electron Plasma

The key ingredient for an effective application of electron cooling is the presence of a well-defined cold electron plasma. Simulations suggest, that a plasma comprising approximately $10^9$ electrons with a density of $10^7$ electrons per cubic centimetre is necessary for a fast cooling process within a few seconds and minimal ion loss due to ion-electron recombination [96, 97]. The following sections will provide a detailed analysis of the production, storage process and properties of the electron plasma at HITRAP.

### 5.1.1 Production and Preparation

At HITRAP, the electrons are produced by a compact photo-ionization source, which is described in detail in Sec. 3.2.6. In order to maximise the electron output, the cathode is coated with a layer of cesium, which can be applied and replenished by heating the installed cesium dispensers. The thickness of the layer is of great consequence, as it determines the electron affinity of the cathode and, in turn, the efficiency of electron production. If the monolayer does not cover the entire cathode, the effective surface area available for electron production is reduced, as the probability of releasing electrons from uncoated GaAs is significantly smaller for the photons' given spectral distribution. Conversely, if the layer is excessively thick, the probability of electron tunnelling through the potential wall of the cesium layer rapidly decreases. It is therefore essential to conduct a careful optimisation of the coating process [149, 150].
In addition to the cesium coating, the purity of the GaAs surface is also an important factor. If the cathode is contaminated by other substances, for instance when the source is exposed to air, the setup must be cleaned. To some extent, this can be achieved by heating the cathode with the installed halogen lamp. If the cathode is mounted under high-vacuum conditions, it can be used for years at a time by cleaning and reapplying the cesium coating on a regular basis, every few months. For more intense contamination, for instance following a prolonged period of exposure to air, this method is no longer sufficient to reinstate the original conditions. In this case, a more effective cleaning process is required, whereby the source is cleaned in a solution of hydrochloric acid.

Following the preparation of the photocathode, a flash of ultraviolet light is focused on the GaAs photocathode to produce an intense electron bunch. A potential of -200 V is applied to the cathode, in order to accelerate the electrons towards the beam line. After an initial focusing of the beam by an electrostatic einzel lens installed in close proximity to the cathode, the electrons are guided towards the HITRAP Cooling Trap by a set of magnetic coils. A Faraday cup is employed in front of the trap to detect the electron bunch and assess its properties.
Figure 5.1 depicts the deposited charge, amplified by a factor $\alpha = 10^3$ V/A, plotted over time. The bunch length and longitudinal shape are consistent with those of the emission pulse of the flash lamp. By integrating the signal $U(t)$ over time $t$, the number of electrons $N_e$ can be calculated using the equation

$$N_e = \frac{\int U(t)\, \mathrm{d}t}{\alpha e},$$

(5.1)

where $e$ denotes the charge of an electron. This yields a total of $5.7 \cdot 10^9$ electrons in the bunch. It should be noted that not the entire bunch can be captured by the Penning trap. For the task of electron cooling, it is necessary to implement a nested-trap configuration for the potential shape,
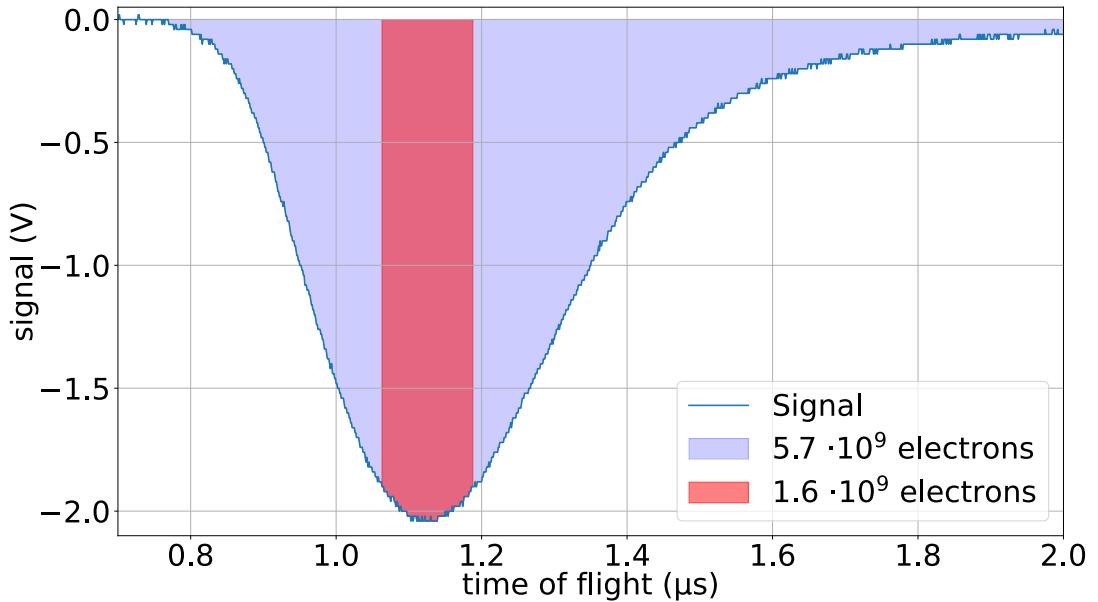
Figure 5.1: Electron signal measured with a Faraday cup positioned directly in front of the Cooling Trap (GTR6DC0). The results demonstrate that a total of $5.7 \cdot 10^9$ electrons (blue) are produced and transported towards the trap. However, only $1.6 \cdot 10^9$ electrons (red) can be captured in a nested trap configuration between the long end-cap electrodes.

to allow for the simultaneous storage of ions and electrons (see Fig. 2.6). This leaves only the volume between the two long end-cap electrodes available for electron storage, thereby limiting the longitudinal acceptance of the trap.

It is difficult to determine a precise value for the accepted length of the electron bunch, as the longitudinal component of the electrons' velocity through the trap is unknown. The electrons are produced with a kinetic energy of 200 eV, but upon entering the magnetic field of the trap, they will transfer some of this energy into a radial motion perpendicular to the trap axis. By measuring the electron signal in front of and behind the setup and scaling the difference in time-of-flight $\triangle t$ to the available length $l$, the longitudinal acceptance $t_{lon}$ can be determined by

$$t_{lon} = \frac{2l}{d} \triangle t, \tag{5.2}$$

with distance between the detectors $d$, to be approximately 130 ns. This corresponds to $1.6 \cdot 10^9$ electrons that can be captured between the two long end-cap electrodes. This estimation is based on the assumption of a constant longitudinal velocity throughout the entire setup. As the energy in the radial motion increases with the strength of the magnetic field, the longitudinal velocity is minimal within the homogeneous trapping region of the magnetic field. It can be reasonably assumed that the result of $1.6 \cdot 10^9$ electrons represents a conservative estimation of the actual number of electrons that can be captured.

The capture process is analogous to the one discussed in Sec. 4.3.1 for the capture of accelerator-produced ions. In the case of electron capture, the far side (left) long end-cap electrode is set to a reflective negative potential. The electrons are unable to pass this potential barrier and are reflected back towards the source. Before they can leave the trap again, the right long end-cap electrode is also switched to the same potential. The experimental optimisation of the potential
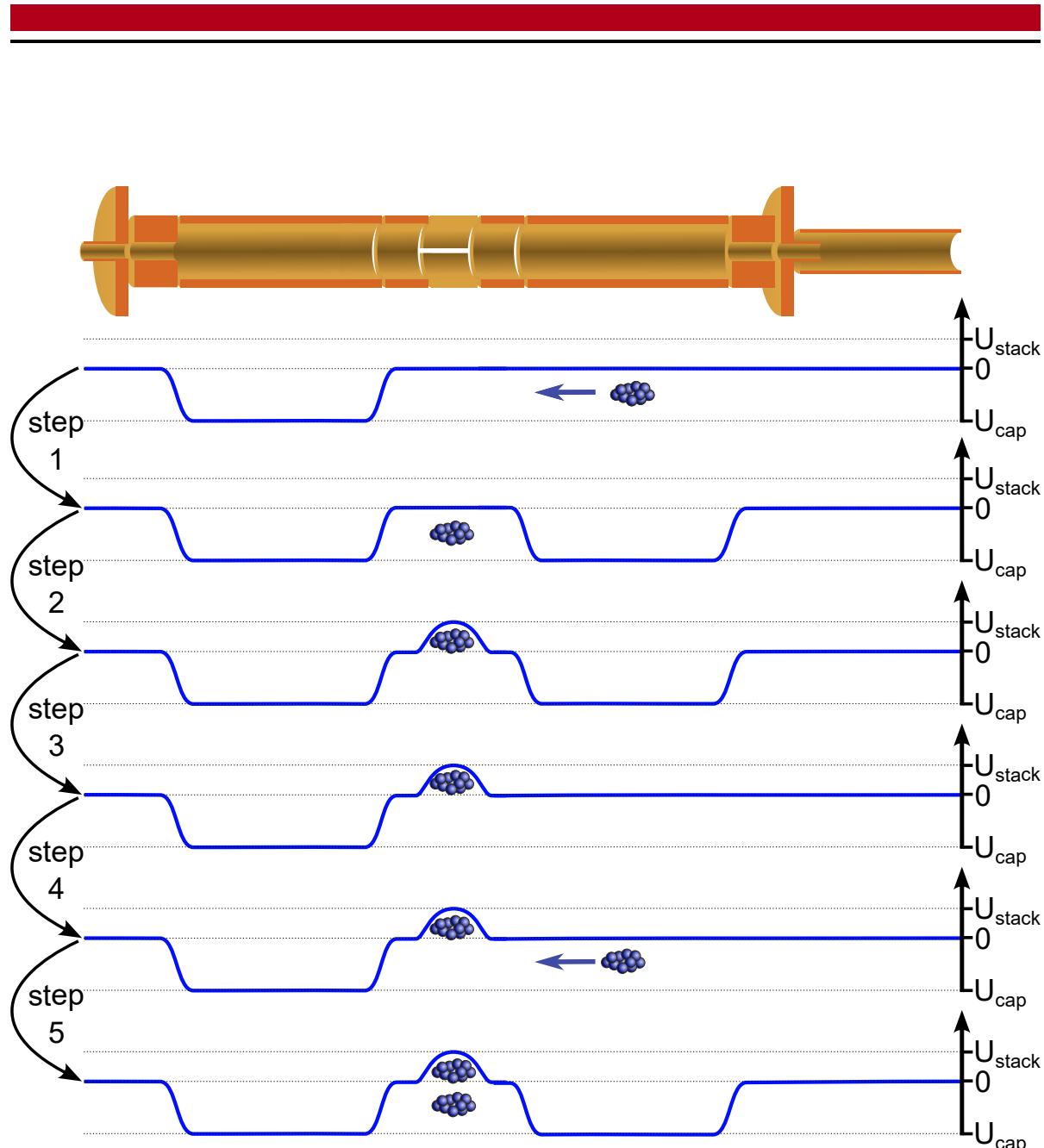
Figure 5.2: Trapping scheme for the capture of multiple injections of electrons. The electrons are produced and injected by the photo-ionisation source, which is situated on the right-hand side of the trap. A negative potential $U_{\mathrm{cap}}$ is applied to the left long end-cap electrode to reflect the electrons. By switching the right long end cap also to a reflective potential, the electrons are captured (step 1). A positive potential $U_{\mathrm{stack}}$ at the ring electrodes prevents the electrons from exiting the trap volume when the capture potential is reduced again (step 2 and 3). The next bunch of electrons is injected and can be captured by the long end caps (steps 4 and 5). Steps 3-5 can be repeated as often as required in order to increase the quantity of stored electrons.

yields -900 V as an optimal capture potential, which is significantly higher than what could be expected solely from the electrons' kinetic energy of 200 eV. Evidently, the high space-charge of the intense electron bunch prevents an effective capturing process for lower potentials.

While the above discussed results meet the requirement of $10^9$ electrons, as predicted by simulations for effective electron cooling, it is possible that even higher numbers may be necessary. In order to achieve this, multiple injections of electrons can be stacked in the Penning trap. This requires the implementation of a slightly more sophisticated trapping scheme, which is schematically illustrated in Fig. 5.2. The first bunch of electrons is captured between the two long end-cap electrodes in the conventional manner.

Subsequently, a positive stacking potential is applied to all ring electrodes, thereby forming a potential well for the electrons. As the kinetic energy of the electrons is constantly reduced due to cyclotron cooling, they will eventually fall into the well and remain trapped between the short end-cap electrodes. By lowering the potential of the right long end cap back to zero, the trap is prepared for the injection and capture of the next electron bunch. The electrons fall into the positive well once again and by repeating this process, the amount of stored electrons can be increased until the space-charge limit of the positive well is approached. At this point, the loss of electrons due to unstable trapping conditions will eradicate the gain from additional injections and an equilibrium is reached. By varying the depth of the stacking potential, the point of equilibrium can be selected arbitrarily as the amount of stored electrons increases with the potential, allowing for reproducible measurements in this state.

## 5.1.2 Setup Alignment

The storage of electrons in the trap also provides the possibility to align the electric and magnetic fields of the Penning trap, as first proposed in [179]. In a perfectly aligned configuration, the magnetic field is parallel to the trap axis and therefore perpendicular to the electric field. When a charged particle is injected into the magnetic field of a Penning trap, it will follow the field which in turn causes radial confinement. The capture of the particle axially by an electric field results in the three modes of motion introduced in Sec. 2.2.2: axial, reduced cyclotron, and magnetron motion.

In the case of magnetron motion, the radius is dependent on the distance of the particle to the symmetry axis of the Penning trap during the injection process. The trajectory is around the centre of the magnetic field with a radius that is equal to the distance to the trap's symmetry axis. This behaviour can be exploited for the purpose of aligning the Penning trap. While the distance to the symmetry axis remains constant for a parallel magnetic field, it changes for an angular misalignment. Consequently, the radius of the magnetron motion also changes for particles that are confined in different regions of the Penning trap. This phenomenon is demonstrated in Fig. 5.3, which visualises in the top frame the consequences of a misalignment of the magnetic field with respect to the symmetry axis of the Penning trap.

A bunch of charged particles is injected into the apparatus, follows the magnetic field and is either captured on the right-hand-side of the trap or on the left side. Given that its distance to the symmetry axis is small on the right side, so is the magnetron radius. On the left side, the distance is larger, resulting also in a larger magnetron radius. If the stored particles are ejected onto a luminescent screen, the magnetron motion can be visualised as circles with a radius corresponding to the respective magnetron radius. For a perfectly aligned setup, the aforementioned
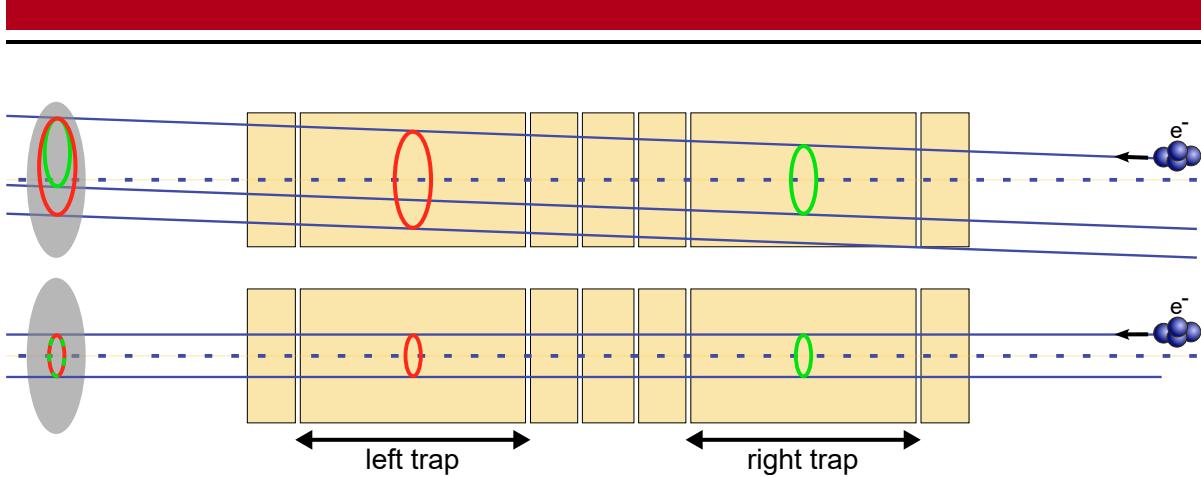
Figure 5.3: Technique to align the Penning trap setup. Electrons are injected into the magnetic field of the trap and captured in two different regions. If the magnetic field is not perpendicular to the electric field (top), the radius of the magnetron motion is dependent on the position of the electrons within the trap volume. Such a misalignment can be visualised using a fluorescence screen. After successful alignment of the fields (bottom) the magnetron motion is independent of the position of the electrons within the trap volume.

circles would overlap as illustrated on the bottom of Fig. 5.3. In all other cases, the signal can be used to align the magnetic field parallel to the symmetry axis of the trap until the circles overlap.

This technique is also applied to the HITRAP Cooling Trap with electrons captured either between the right short end cap and capture electrode or between the left short end cap and capture electrode, as it is also indicated in Fig. 5.3. The electrons are then stored for a short period of only a few microseconds and subsequently ejected onto the screen installed in close proximity to the left of the setup (GTR5DF3) that is monitored by a CCD camera. For each ejection, the electrons generate a signal comprising a single spot, with the position dependent on the phase of the magnetron motion during the time of ejection. For the same storage time, the spot therefore always appears at the same position of the detector. While scanning the storage time within one period of magnetron motion, which lasts approximately $100\,\mu\text{s}$, the observed position traces out a circle. This circle can be visualised with the aid of a 'peak-hold' function of the camera software, which displays the highest recorded value for each pixel over the course of multiple measurements.

The results of the initial measurement series is presented on the left-hand-side of Fig. 5.4, where parts of two intersecting circles are visible. The red circle represents electrons trapped on the left side of the Penning trap while the green circle corresponds to electrons that have been trapped on the right side. Three separate degrees of freedom can be described by the properties of the circles:

1. **Field alignment:** As the circles are not overlapping, this measurements proves that the magnetic field is not perpendicular to the electric field.

2. **Setup position:** The point of intersection corresponds to the injection trajectory and coincides with the offset position observed for electrons that pass the trap without being captured. It is evident that the trap setup is not centred to the surrounding beam line, as the offset position is not central on the screen.
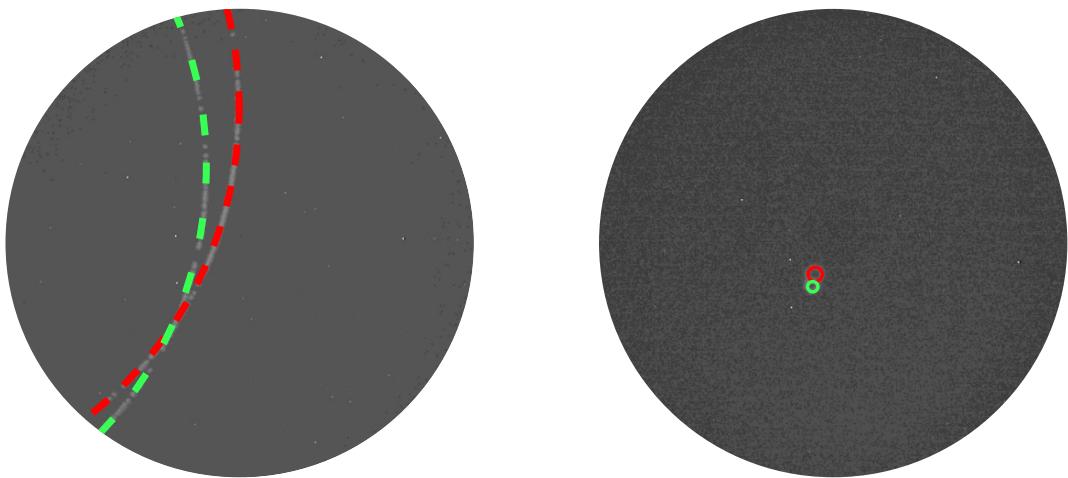
Figure 5.4: Visualisation of the magnetron radius for stored electrons. The electrons are captured in two different positions within the Cooling Trap, either between the right short end cap and right capture electrode (green) or between the left short end cap and left capture electrode (red, comp. Fig. 5.3). The left screen depicts the initial state prior to alignment corresponding to magnetron radii of (4.21±0.18) mm and (4.04±0.17) mm, respectively. After alignment of the setup (right screen), these radii are reduced to (74±10) µm and (55±10) µm.

3. **Injection trajectory:** The diameter of both circles is larger than that of the detector (42 mm), which results in only a partial visibility of the circles. As the magnetron radius depends on the distance of the electron bunch to the trap's symmetry axis, the large size of the circles demonstrate an imperfect injection trajectory.

Fitting two circles to the image yields the radii listed in the left column of Tab. 5.1. Given that the detector is not situated within the region of maximum magnetic field, the observed circles are, in comparison to the magnetron motion inside the trap, expanded by a factor

$$\alpha = \sqrt{\frac{B_0}{B_{\text{det}}}}, \tag{5.3}$$

with the magnetic flux density inside the Penning trap $B_0$ and at position of the detector $B_{\text{det}}$. With the given ratio of $B_0/B_{\text{det}} \approx 70$ for this setup, this results in an expansion factor of approximately 8.4, yielding magnetron radii of (4.21±0.18) mm for electrons in the left-hand section of the trap and (4.04±0.17) mm for those in the right section. This demonstrates that the electrons are not injected in close proximity to the symmetry axis of the Penning trap.

The results of this initial measurement serve as the starting point of the subsequent alignment process:

- In a first step, the entire Cooling Trap setup is centred to the beam line, thereby shifting the offset position for electrons passing the trap without being captured in the centre of the screen.

- Following this, the circles are overlapped and their radii reduced. The overlapping of the circles is accomplished by tilting the Penning trap in the horizontal and vertical planes.

Table 5.1: Radii of the circles presented in Fig. 5.4 resulting from confining electrons in two spatially separated regions of the Cooling Trap and subsequent extraction onto a phosphor screen. Due to the diverging magnetic field, the corresponding magnetron radii listed below are significantly smaller.

|  | before alignment | after alignment |
|---|---|---|
| **observed radius (left) in mm** | 35.19±1.44 | 0.62±0.08 |
| **observed radius (right) in mm** | 33.78±1.39 | 0.45±0.08 |
| **magneton radius (left) in mm** | 4.21±0.18 | 0.074±0.010 |
| **magneton radius (right) in mm** | 4.04±0.17 | 0.055±0.010 |

- In order to minimise the radius of the magnetron motion, it is necessary to ensure that the trajectory of the electrons coincides with the symmetry axis of the trap upon injection. It is not feasible to modify the injection trajectory into the Penning trap as this is completely determined by the strong magnetic field of the setup. Instead the electrode stack is moved in parallel towards the electrons' trajectory, until the magnetron radius is observed to be minimal.

The final state of the alignment process, as illustrated in Fig. 5.4 on the right, is limited by the precision of the available adjustment possibilities. Despite the fact that the circles still are not overlapping, the angular misalignment is now reduced to $< 1 \cdot 10^{-3}$ degree. The radii of the observed circles are listed in the right column of Tab. 5.1 together with the corresponding magnetron radii. After alignment, the radii are diminished by a factor of more than 50. This reduction of the magnetron radius effectively also increases the density of the stored electron cloud and consequently facilitates electron cooling as a higher electron density yields a higher cooling power.

### 5.1.3 Plasma Properties

A deeper understanding of the properties of a stored electron plasma is imperative for the implementation of electron cooling. For instance, both the electron number and the plasma density are important parameters that influence the efficiency of the cooling process.

It is not feasible to determine the number of electrons stored in the Penning trap through conventional methods, such as analysing a Faraday cup signal like in Sec. 5.1.1. The rapid switching of the confining electrode produces a considerable amount of electrical noise that impedes any detection method that relies on an external amplifier. As non-destructive detection methods are not yet implemented for the Cooling Trap, MCP detectors represent the sole viable option for electron detection. While these detectors yield a signal that is, in first approximation, proportional to the number of incoming particles, they are unable to provide an accurate count as the voltage-dependent amplification of the plates is unknown.

In order to extract at least an estimation of the amount of stored electrons, the space-charge produced by the electron plasma is exploited. The electrons are captured and stored between the two long end-cap electrodes, as described in Sec. 5.1.1. They are then ejected towards the left side, where they can be observed by the MCP detector installed in GTR5DK2. Upon extraction, a part of the electrons is accelerated towards the detector by the space-charge potential $V_{\mathrm{sc}}$. As the

first electrons exit the trap volume, the accelerating space-charge potential decreases, therefore not all electrons are accelerated to the same energy. The electrons' maximum kinetic energy $E_{\mathrm{kin,max}}$ is consequently given by

$$E_{\mathrm{kin,max}} = E_{\mathrm{kin,t}} + eV_{\mathrm{sc}}. \tag{5.4}$$

In this context, $E_{\mathrm{kin,t}}$ denotes the kinetic energy of the stored electrons at the time of extraction. This energy depends on the storage time as the electrons radiate off their kinetic energy via cyclotron cooling (see Sec. 2.3.2). In the presence of a strong magnetic field of 6 T, the cooling constant can be calculated with Eq. 2.63, resulting in a value of 72 ms. After a storage time of 500 ms, the initial kinetic energy of the electrons, which was 200 eV, is reduced to approximately 0.2 eV. The space-charge produced by the electron cloud can thus be determined by measuring the maximum kinetic energy of the ejected electron bunch.

To this end, a retarding field potential, $V_{\mathrm{r}}$, is applied to the left capture electrode. On their way to the detector, the electrons need to pass this electrode and overcome the retarding field. Only electrons with a kinetic energy of

$$E_{\mathrm{kin}} > eV_{\mathrm{r}} \tag{5.5}$$

will reach the detector and contribute to the observed signal. Scanning the applied retarding field potential will therefore yield the maximum kinetic energy of the ejected electron bunch, which is defined as the highest value that still allows some electrons to reach the detector.

The results of these measurements are presented in Fig. 5.5, which plots the integrated electron signal as a function of the applied retarding field potential. For each data point, the averaged signal of 50 consecutive injections is integrated to enhance statistical reliability. The data demonstrate, that even at a retarding field potential of -700 V, some electrons are still able to reach the detector. Consequently, the maximum observed kinetic energy is $> 700$ eV.

If the stored electron plasma is approximated as evenly distributed over a cylindrical volume of length $l_{\mathrm{p}}$ and radius $r_{\mathrm{p}}$, the on-axis space-charge potential can be calculated using Eq. 2.51. The length is given by the distance between the confining electrodes, which is (99.3±0.6) mm, while the radius of the electron plasma may be extracted in a manner analogous to that employed for the magnetron radius (see Sec. 5.1.2). For the on-axis space-charge potential experienced by a single electron, electrons located on the opposite side of the magnetron circle have a negligible effect compared to electrons in the same phase of the motion. Accordingly, the plasma radius is chosen as the radius of a single point produced on the phosphor screen by a single ejection of stored electrons, which is approximately 20 µm. As this value approaches the resolution limit of the detector setup, a rather high uncertainty of ±10 µm is considered. The radius of the trap is 20.50±0.05 mm. With the measured space-charge potential of (700±10) V, this yields a total of (3.4±0.2)·$10^9$ electrons, which agrees with the results of Sec. 5.1.1, where the conservative lower limit is observed to be 1.6·$10^9$ electrons.

Furthermore, this approach can be employed to estimate the effectiveness of the stacking technique introduced above. Here, a part of the stored electrons is concentrated in a positive potential well formed by the central ring electrode. Owing to the technical limitations of the current setup, this 'stacking potential' is limited to 200 V. Together with the length of the ring electrode, which is (36.2±0.4) mm, this allows for the preservation of (0.34±0.02)·$10^9$ electrons. Given that the subsequently injected electron bunch is likely to exhibit a different phase in the magnetron motion, it is possible to stack multiple injections of electrons radially inside the potential well.
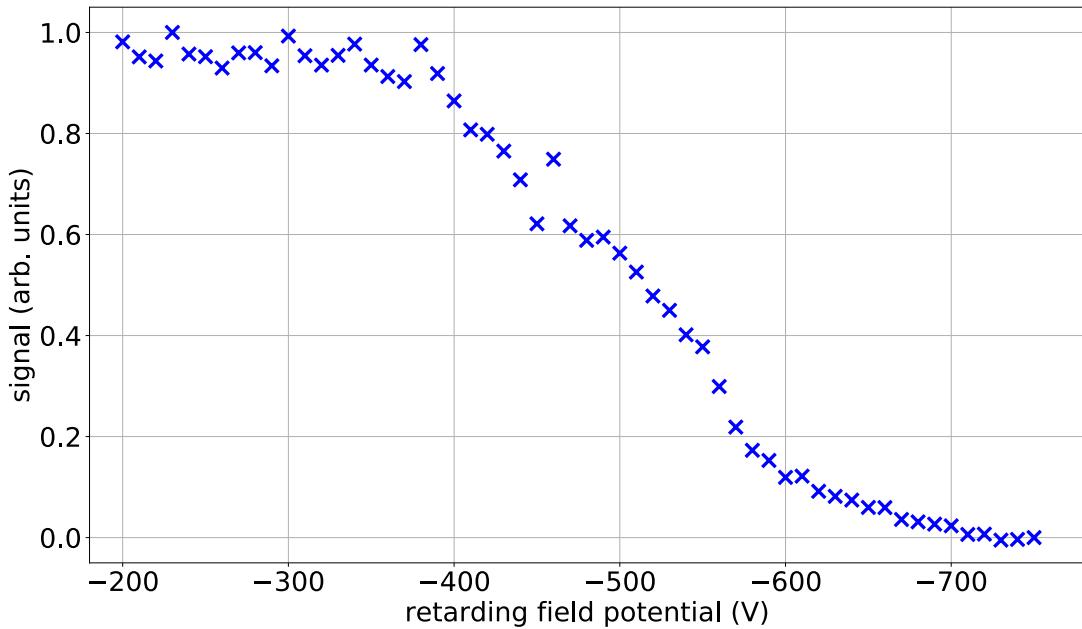
Figure 5.5: Measurement of the space-charge produced by the electron plasma. The electrons are confined between the two long end-cap electrodes and upon extraction, they are accelerated by the space-charge potential. By applying and scanning a retarding field potential on the extraction-side capture electrode, it is possible to determine the space-charge potential and consequently the number of stored electrons. The integrated electron signal on an MCP detector is plotted over the retarding field potential. It can be observed that electrons with the highest energy can pass -700 eV, corresponding to $(3.4\pm0.2)\cdot10^9$ trapped electrons.

The assumption of radial stacking is supported by the fact, that the observed on-axis space-charge potential only insignificantly increases for multiple injections in comparison to the above presented value for a single bunch of electrons.

Simulations indicate that an electron plasma comprising $10^9$ electrons with a density of $10^7$ electrons per cubic centimetre is optimal for efficient electron cooling. As presented above, the predicted number is already exceeded with a single injection of electrons. A reduction in number can be readily achieved by lowering the confining potential, consequently limiting the maximum space-charge potential which, in turn, also limits the number of stored electrons. Should the anticipated number prove to be insufficient, the stacking technique allows for the electron number to be increased to the order of $10^{10}$ through the accumulation of multiple injections.

The density of the plasma can be estimated by assuming the plasma volume to be a cylinder with a radius equal to the magnetron radius and a length corresponding to the distance between the confining electrodes. For a single injection and storage between the two long end-cap electrodes, this yields an electron density of $(2.5\pm0.8)\cdot10^{12}$ electrons/cm$^3$. The magnetron radius is extrapolated here as the mean of the two magnetron radii calculated in Sec. 5.1.2, namely $(65\pm6)\,\mu$m, as the available trap volume is located between the volumes employed in the corresponding section. Given that the radius of the electron beam is of the same order of magnitude as the magnetron radius of the cloud, the approximation of an evenly distributed, cylinder-shaped plasma is justifiable. The resulting density is orders of magnitude higher than

the optimal value expected from simulations.

According to [97], an exceedingly high density would accelerate the cooling process, but would also considerably increase the recombination rate of ions with the electron plasma. If this behavior is indeed also experimentally confirmed, the magnetron radius could be increased by shifting the electron injection trajectory radially away from the symmetry axis of the trap, thereby reducing the electron density while maintaining the number of electrons.

In this case, the assumption of an evenly distributed electron plasma over a cylindrical volume is no longer valid. Instead, the electron plasma assumes the shape of a hollow cylinder. Inside the 'wall' of the cylinder, the electron density is then still extremely high, as the results of Sec. 5.1.2 show that the density along the magnetron motion is independent of the magnetron radius. This scenario has not been treated by simulations but must be investigated experimentally.

## 5.2  Storage of Highly Charged Ions

The HITRAP Cooling Trap is designed for the specific purpose of electron cooling on heavy, highly charged ions. As previously stated, the availability of such heavy ions is limited to short periods of beamtime, rendering commissioning a Penning trap with these ions unfeasible. To address this challenge, a local EBIT ion source (see Sec. 3.2.7) is available to prepare the setup for accelerator-produced ions. The crucial parameter to achieve comparable conditions to heavy, highly charged ions is the mass-to-charge ratio, which is in the case of hydrogen-like uranium approximately 2.6. This ratio is easily attainable with an EBIT for light to medium-heavy ions. With the electron plasma ready for tests of electron cooling, as presented in the preceding sections, the following section will examine the preparation and properties of locally produced ions in greater detail. For this phase of the commissioning process, $^{40}\text{Ar}^{16+}$ is selected as ion species, which has a mass-to-charge ratio of 2.5.

### 5.2.1  Ion Production and Transport

For the production of $^{40}\text{Ar}^{16+}$, high purity argon gas is injected into the EBIT. As the natural abundance of argon-40 is 99.6% [180], beam contamination by other argon isotopes can be neglected. The atomic gas is introduced into the source by a dosing valve[1], thus ensuring a constant gas pressure. An electron beam with a current of approximately 19 mA and an energy of 6.5 keV then ionises the argon atoms, which are subsequently trapped on a source potential of 4 kV. The end-cap electrodes, operated at 4.1 kV, prevent the ions from escaping axially.

Following a breeding time of 1.3 s, the ion bunch is ejected towards the adjacent beam line by lowering the confining potential on the corresponding side. The ions are now accelerated by the source potential, acquiring a kinetic energy of 4 keV/$q$ and transported through the 11-metre-long beam line connecting the EBIT with the Cooling Trap (see Fig. A.6 and A.5). This transport line also incorporates a 90-degree magnetic bender (GTR6MV1), which enables charge separation as the deflection angle of an ion in a magnetic field is dependent on its charge.

As outlined in Sec. 3.2.7, the statistical nature of the ionisation process in the EBIT results in a variety of charge states within the extracted ion bunch. This is illustrated on the left side of Fig. 5.6 in blue, which depicts the ion signal detected on the Faraday cup (GTR6DC2) in close proximity before the magnetic bender plotted over time. The observed charge states range from

---

[1]Pfeiffer UDV 146 with RVG 050 C control unit
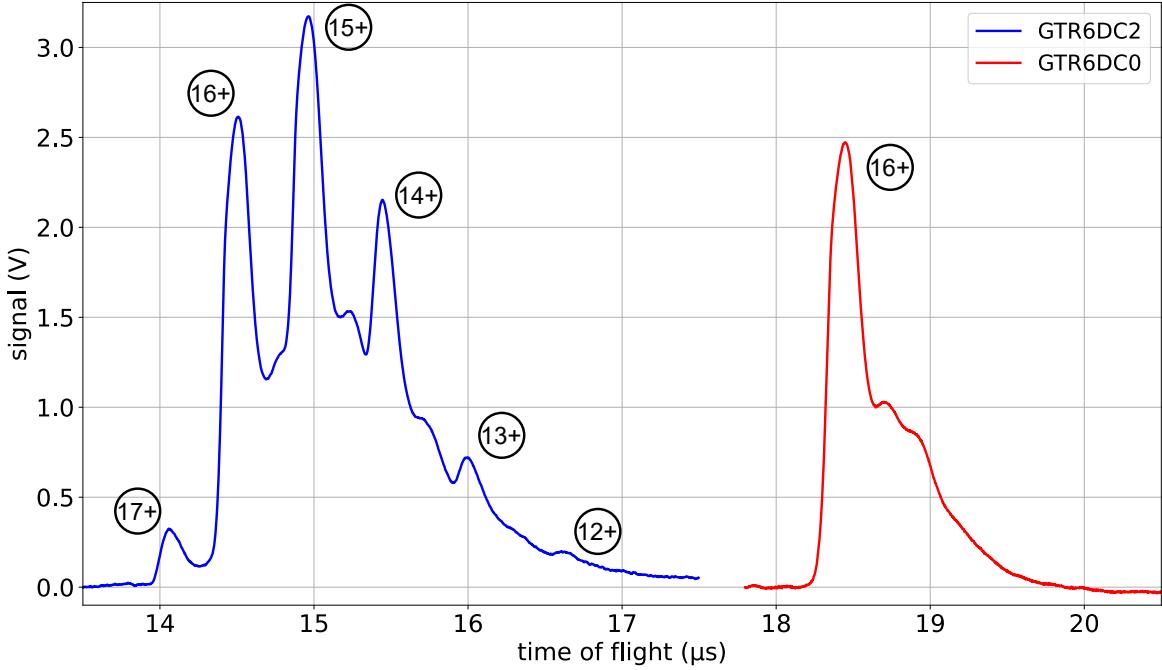
Figure 5.6: Ion signal detected on the Faraday cups in two positions: before charge separation in the magnetic dipole deflector (GTR6DC2, blue) and after charge separation in front of the Cooling Trap (GTR6DC0, red). Prior to charge separation, a multitude of charge states, all produced in the EBIT, is observed, ranging from 12+ to 17+. After passing the magnetic deflector, only a single charge state, 16+, remains. The signal of $Ar^{16+}$-ions reaching the trap corresponds to $(4.2\pm0.1)\cdot10^5$ ions.

12+ to 17+, clearly separated in time. This is due to the fact that the velocity of ions with a fixed energy per charge is contingent upon the charge state. The maximum of the charge state distribution is determined by the breeding time in the EBIT and is, in this case, 15+ as it has a higher production probability than the selected charge state 16+. After separation in the dipole magnet, a clean bunch of $Ar^{16+}$-ions can be detected by the last Faraday cup prior to the Cooling Trap (GTR6DC0) as presented on the right side Fig 5.6 in red. A substitution of the electron charge in Eq. 5.1 with the charge of the ion enable the number of ions in the signal to be extracted, which is $(4.2\pm0.1)\cdot10^5$.

Following transportation of the ions through the trap, they can be detected by a retarding field energy analyser (RFEA, see Sec. 3.2.8) installed in GTR5DK2. By scanning the applied potential, it is possible to extract the energy distribution of the incoming ion bunch, as illustrated in Fig. 5.7. The data points in blue represent the integrated signal detected on the MCP detector of the RFEA, which are plotted over the applied retarding field potential. Increasing the potential results in a reduction in the detected signal, as only ions with an energy per charge in the velocity component parallel to the electric field that exceeds the applied potential can pass the grates and contribute to the signal. Consequently, the shape of the data set not only depends on the ions' total kinetic energy $E$ but also on the angle $\theta$ under which they hit the detector. The higher the deviation from the ideal angle of 0 degrees to the symmetry axis of the beam line, the lower is the kinetic energy in the longitudinal component of the motion $E_\perp$ (perpendicular to the mesh)
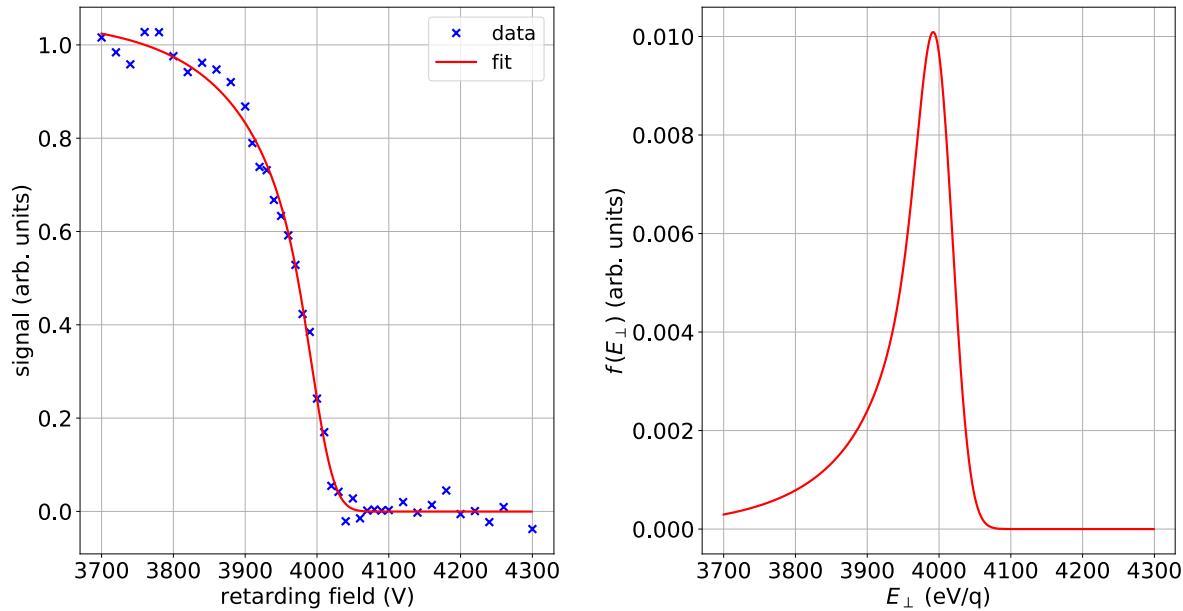
Figure 5.7: Left: signal measured on the retarding field energy analyser plotted over the applied retarding field potential (blue). To improve clarity, error bars are omitted. The data is fitted with the function given in Eq. 5.8 which results in the red curve. Right: Distribution of kinetic energy in the longitudinal component of the motion, which is extracted from the fit parameters and Eq. 5.7.

and the maximum retarding field the ion can pass. This relation can be expressed as

$$E_\perp = E \cos^2(\theta). \tag{5.6}$$

The data is fitted assuming a Gaussian-shaped energy distribution around a central energy $E_0$ and a Gaussian-shaped angle distribution around a central angle $\theta_0$ to the perpendicular trajectory. A Gaussian-shaped angle distribution is a valid assumption for ions passing the magnetic field of the Cooling Trap and subsequently undergoing deflection in the diverging field based on their distance to the symmetry axis. In order to calculate the distribution of the kinetic energy in the longitudinal component $f(E_\perp)$, the joint distribution of energy and angle must be integrated over all possible angles

$$f(E_\perp) = \frac{A}{2\pi\sigma_E\sigma_\theta} \int_{-\pi/2}^{\pi/2} \exp\left(-\frac{\left(\frac{E_\perp}{\cos^2\theta} - E_0\right)^2}{2\sigma_E^2} - \frac{(\theta - \theta_0)^2}{2\sigma_\theta^2}\right) d\theta, \tag{5.7}$$

with the corresponding standard deviations $\sigma_E$ and $\sigma_\theta$ and amplitude $A$. The variable of the energy distribution is replaced according to Eq.5.6.
As the detector does not directly probe for $f(E_\perp)$ but rather detects all particles that are able to pass the applied retarding field potential $V$, a second integration is necessary in order to derive the measured distribution $f(V)$ as formulated with the equation

$$f(V) = \int_V^\infty f(E_\perp) dE_\perp. \tag{5.8}$$

Table 5.2: Parameters for fitting Eq. 5.8 to the data obtained from measuring an EBIT ion beam with the retarding field energy analyser. The raw data and the resulting fit curve are plotted in Fig. 5.7 over the applied retarding field.

| $E_0$ (eV/$q$) | $\sigma_{\mathrm{E}}$ (eV/$q$) | $\theta_0$ (°) | $\sigma_\theta$ (°) | $A$ (arb. units) |
|---|---|---|---|---|
| 4005.8$\pm$2.2 | 21.9$\pm$3.2 | 0.00$\pm$1.50 | 7.50$\pm$0.18 | 1.07$\pm$0.03 |

Eq. 5.7 does not have an analytical solution, consequently the integrals are solved numerically. The resulting fit, displayed on the left-hand side of Fig. 5.7 in red, yields the parameters listed in Tab. 5.2. As defined by the source potential, the central energy is observed to be (4005.8$\pm$2.2) eV/$q$ with a standard deviation of (21.9$\pm$3.2) eV/$q$. Former measurements based on laser spectroscopy predict a lower value for the standard deviation [133]. The result presented here is limited by the resolution of the detector and in good agreement with expectations based on the homogeneity of the electric field inside the mesh (see Sec. 3.2.8).

An examination of the distribution of kinetic energy in the longitudinal motion component, as displayed on the right-hand side of Fig. 5.7, reveals that it is primarily determined by the angle distribution of the ions hitting the detector. The maximum and standard deviation of the angle distribution are extracted from fit to be $\theta = (0.00 \pm 1.50)°$ and $\sigma_\theta = (7.50 \pm 0.18)°$, respectively. It is possible to reduce these values to some extend by optimising the beam line. The biggest impact is expected in the relatively short section between the Cooling Trap and the detector, as the diverging field of the trap's magnetic field presents a significant challenge to maintaining a beam trajectory parallel to the beam line axis.

The angle dependence of the detector can be eliminated by the addition of two apertures prior to the detector, only allowing ions moving parallel to the beam line axis to hit the detector in the first place. On the downside, this would also significantly reduce the beam intensity and, in turn, also the detected signal. Due to space limitations within the diagnostic chamber, the implementation of diaphragms would require a major redesign of the setup and is therefore not planned for the near future. However, it remains as a potential option to enhance the resolution of the detector and facilitate the analysis process.

### 5.2.2 Storage Process

In order to capture ions coming from the EBIT, a trapping scheme very similar to the one described in Sec. 4.3.1 and illustrated in Fig. 4.11 is employed. As the ions now arrive from the opposite direction, the aforementioned scheme is mirrored and the far side captured electrode is on the left side of the trap. Additionally, the electrical limitations of the setup, namely the maximum potential difference between two neighbouring electrodes of 10 kV, no longer present an issue, due to the lower kinetic energy per charge of the locally produced ions in comparison to the ones coming from the accelerator. Their energy of 4 keV/$q$ allows for an efficient storage process with capture potentials of only 7 kV. Furthermore, the manipulation of the stored ions' energy through the alteration of the reference potential (steps 3 and 4 in Fig. 4.11) can now be achieved in a single step, consequently allowing for shorter storage times and less complex trapping schemes. The lifetime of the stored ions can be extracted in a manner analogous to that described in Sec. 4.3.2 by measuring the ion signal after ejection with an MCP detector for various storage times. Figure 5.8 illustrates the results of such a series of measurements. For each data point the
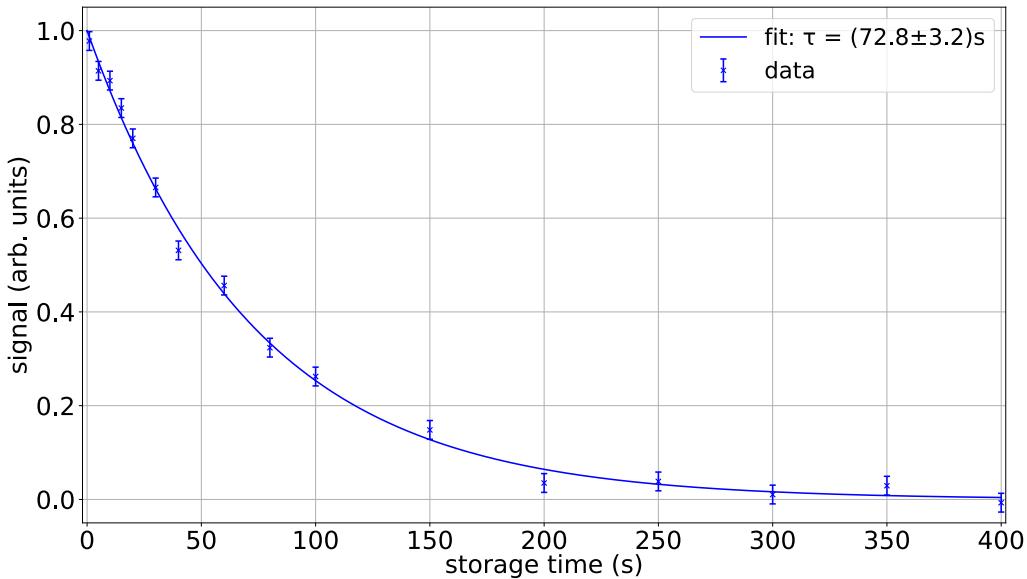
Figure 5.8: Signal of Ar-ions plotted over the storage time in the Cooling Trap. For each data point, the ions are stored in the trap for a given time and observed after extraction by an MCP detector. Fitting an exponential decay onto the data yields an ion lifetime of (72.8±3.2) s.

mean value of four consecutive injections of ions is calculated. By fitting an exponential decay function, Eq. 2.62, to the data it is possible to determine the ions' lifetime to be (72.8±3.2) s. It is important to note that this lifetime corresponds to the lifetime of a particle, rather than a certain charge state. The charge state lifetime is likely significantly smaller.

One possible approach to measure the lifetime of a charge state is to separate the charge states during the ejection process. Assuming the total kinetic energy of a stored ion remains unchanged during the process of charge exchange, the kinetic energy per charge consequently increases when the charge state is reduced. To illustrate, an $Ar^{16+}$-ion with a kinetic energy of $4\,keV/q$ would become an $Ar^{15+}$-ion with $4.27\,keV/q$ after charge exchange with residual gas. These two charge states can be separated by switching the extraction-side electrode not to zero but to a potential that blocks ions in the initial charge state of 16+ and allows only ions with lower charge state to pass, e.g. $4.15\,kV$. This technique is employed and discussed extensively in [30] and [104]. The results of these measurements show an unexpected behaviour of the charge exchange process, primarily due to the observation that the charge state lifetime is not constant over time. Instead, the storage process can be divided into two phases with a very short lifetime of only a few seconds in the first phase and a significantly longer lifetime in the second phase, which is approximately one order of magnitude higher.

These result are tested with a similar measurement technique, which employs the retarding field energy analyser in GTR5DK2. The separation of charge states is then achieved through the constant retarding field of the mesh which eliminates any potentials uncertainties that may arise from the switching process of the capture electrode. If the above stated assumption, that the total kinetic energy remains constant throughout the storage process, is correct, scanning the retarding field potential should yield a series of distinct peaks, each corresponding to a different
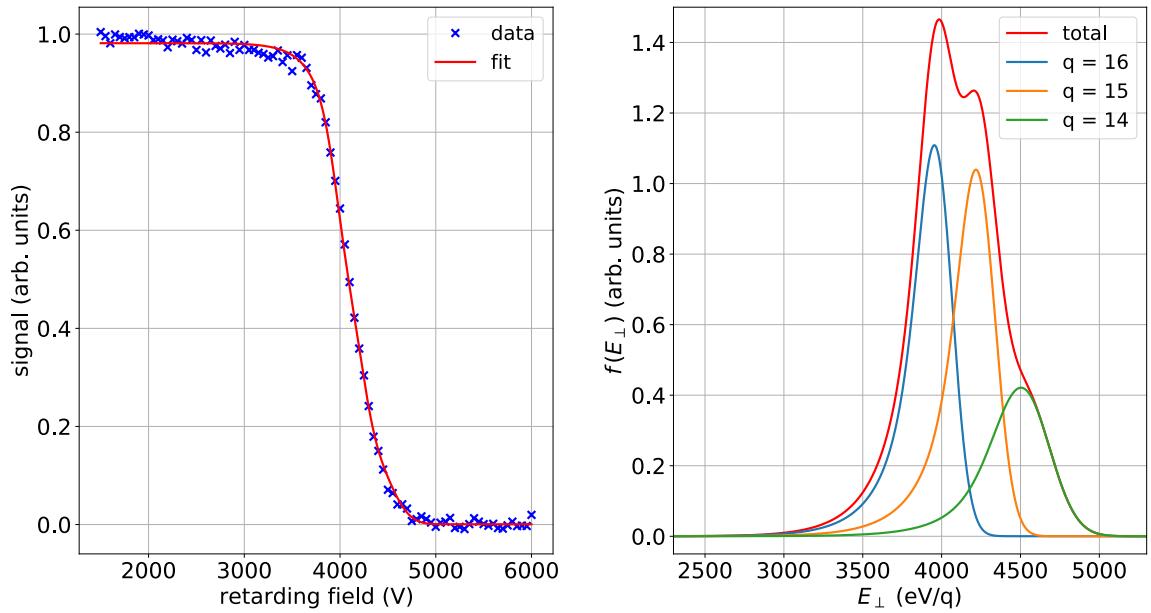
Figure 5.9: Left: signal of ions after 2 s of storage measured with the RFEA and plotted over the applied retarding field potential (blue). To improve clarity, error bars are omitted. The data is fitted with Eq. 5.8 assuming no energy transfer to residual gas during charge exchange which results in the red curve. Right: Distribution of kinetic energy in the longitudinal component of the motion, extracted from the fit parameters and Eq. 5.7.

charge state in the trap. Given that the FWHM, defined as

$$FWHM = 2\sqrt{2\ln 2}\sigma_{\mathrm{E}}, \tag{5.9}$$

of the distribution of kinetic energy in the longitudinal component of the ions' motion is 72.5 eV/$q$ (see Sec. 5.2.1) and thereby smaller than the separation of two charge states ($\geq$270 eV/$q$), it can be expected that the peaks are easily distinguishable.

In Fig. 5.9, the results of a measurement series with a storage time of 2 s is depicted. The data analysis is conducted in an equivalent manner as described in the preceding section. In order to account for charge exchange, it is assumed that the signal consists of multiple charge states. The central energy is fixed in the fit routine based on the injection energy of (4005.8±2.2) eV/$q$ and the assumption that the total kinetic energy of an ion remains constant during charge exchange. The optimal fit result is obtained using three charge states (16+, 15+ and 14+) yielding the parameters listed in the first column of Tab. 5.3. Assuming less charge states involved would not result in a satisfactory description of the data and yield a significantly higher value for $\chi^2$. Including an additional charge state 13+ into the fit routine yields a negligible contribution of such ions to the total energy contribution.

In comparison to the properties of the uncaptured ion beam, the standard deviation of the energy distribution is now significantly higher, which can be attributed to ion-ion or ion-residual gas collisions. The slightly wider angle distribution hints towards less favorable beam line settings between trap and detector. The greatest discrepancy between the observed and expected values lies in the parameters for the amplitudes. While the data presented in [30] and [104] predict

Table 5.3: Parameters for fitting Eq. 5.8 onto the data produced by measuring ions after a storage time of 2 s. The fit routine with fixed $E_0$ assumes no energy transfer to residual gas during charge exchange and consequently fixed values for the central energies. Leaving also these values variable yields similar results but with extremely high uncertainties. Raw data and resulting curve of the fixed-energy fit are plotted in Fig. 5.9 over the applied retarding field.

| fit routine | $E_0$ **fixed** | $E_0$ **variable** |
|---|---|---|
| $E_0(q = 16)$ **(eV/$q$)** | 4005.8±2.2 | 4050±101 |
| $\sigma_{\mathrm{E}}(q = 16)$ **(eV/$q$)** | 98.1±28.0 | 99±59 |
| $E_0(q = 15)$ **(eV/$q$)** | 4272.9±2.3 | 4315±114 |
| $\sigma_{\mathrm{E}}(q = 15)$ **(eV/$q$)** | 104.7±46.7 | $119^{+226}_{-119}$ |
| $E_0(q = 14)$ **(eV/$q$)** | 4578.1±2.5 | 4496±1641 |
| $\sigma_{\mathrm{E}}(q = 14)$ **(eV/$q$)** | 159.7±55.8 | $239.1^{+531}_{-239}$ |
| $\theta_0$ **(°)** | 0.13±2.00 | 0.1±5.8 |
| $\sigma_\theta$ **(°)** | 10.54±0.22 | 11.8±1.4 |
| $A(q = 16)$ **(arb. units)** | 0.39±0.12 | $0.4^{+0.4}_{-0.4}$ |
| $A(q = 15)$ **(arb. units)** | 0.39±0.13 | $0.4^{+1.6}_{-0.4}$ |
| $A(q = 15)$ **(arb. units)** | 0.22±0.15 | $0.2^{+3.5}_{-0.2}$ |

that approximately 30% of the ions undergo charge exchange within the first 2 seconds of storage, this measurement yields with (61±10)% about twice that value. One possible explanation for this discrepancy is a potentially higher residual gas density inside the trap volume.

If the data is fitted with non-fixed values for the central energy, the fit parameters show only minor deviations as presented in the second column of Tab. 5.3, but with extreme uncertainties that are often higher than the parameter itself. This leads to the conclusion that a wide range of values are able to describe the measured energy distribution, and that the results strongly depend on the given boundary conditions. This renders a reliable investigation of charge exchange processes with this detector unfeasible. Nevertheless, the shift of the distribution's maximum towards a higher energy per charge compared to the measurement of ions without storage in the Cooling Trap (see Fig. 5.7), demonstrates the presence of ions with lower charge states despite them being hardly visually distinguishable.

These observations not only demonstrate that the energy analyser is unable to separate charge states, but also question the reliability of the results presented in [30] and [104]. These earlier attempts at charge state separation are independent of any angular distribution after ejection, as the separation is performed in the homogeneous region of the magnetic field, forcing the ions onto a trajectory parallel to the beam axis. The values for the standard deviation derived in this study indicate that the FWHM of the ions' energy distributions is comparable to the energy difference between two charge states. Consequently, this technique is no more suited to separate charge states than the RFEA.

In order to provide a definitive account of charge exchange processes occurring within the trap, it is necessary to implement a more sophisticated method of charge separation after ejection. One possible approach would be the utilisation of the magnetic bender GTR6MV1, which is already

employed to separate charge states of ions coming from the EBIT. While this approach is easily applicable for ions from the GSI accelerator, it comes with two significant technical challenges for ions produced by the EBIT:

- The ions need to pass through the beam line in both the direction of the Cooling Trap and in the opposite direction, back towards the source. As the beam line is almost exclusively equipped with electrostatic beam-guiding elements, only minor adjustments for most elements are expected due to a slightly different trajectory. In contrast, the magnetic bender requires a change in polarity to direct the ions back, which is realised by switching between two separate power supplies. A simple change of the polarity after a single power supply would prove insufficient, as hysteresis effects within the magnet demand two separate current values. In accordance with Lenz's law, the alteration of the magnetic field is impeded by the generation of a counter-orientated field during the magnet's ramping process. The change of polarity therefore takes a macroscopic period of time, compared to switching electrostatic potentials, in the order of a few seconds, limited by the power of the employed power supplies. Consequently, this restricts the minimum storage time and prevents an investigation of the charge exchange process for short storage times.

- A detector is required that is non-destructive for ions on their path towards the Cooling Trap, yet capable of detecting them on their way back. This issue is addressed by the design of an off-axis MCP detector, as described in detail in Sec. 3.2.8, which is implemented in GTR6DK2 and GTR6DK4. The ions are then deflected onto the MCP by a switchable potential on the deflector plate. If the deflection potential is set to zero, the ions should be able to pass the detector uninfluenced. Unfortunately, this design proved to be flawed as several issues with yet unidentified cause arise during operation.

The investigation of these issues is still ongoing at the time of writing, and in addition, alternative detector designs are under discussion. In the current state, this faulty detector design prevents a reliable charge separation after storing the ions in the Cooling Trap and consequently the lifetime of a charge state remains uncertain. This value becomes particularly relevant in the context of electron cooling of heavy HCI, as their higher charge state will accelerate the rate of charge exchange with residual gas. Additionally, the recombination rate with the electron plasma is to date only predicted by simulations for highly charged ions. At this point, a reliable charge separation becomes imperative to validate the results of the simulations.

### 5.2.3 Towards non-destructive detection

An alternative to charge separation after the storage process is the non-destructive detection of ions that are still confined the trap. This approach is widely employed in trap setups and based on the detection of the particles' modes of motion, as discussed in Sec. 2.2.5. As the three motions in a Penning trap, namely axial, magnetron and reduced cyclotron oscillation, are contingent upon the ion's charge state, the observation of one of these motions will allow for the investigation of charge exchange processes during the storage period.
The detection requires the careful configuration of frequency-dependent filters and amplifiers. Consequently, a prior knowledge of the motion frequencies is beneficial for the preparation stage. In an ideal Penning trap with a harmonic electrical field, these frequencies can be precisely calculated. Given the 'bathtub'-like configuration of the Cooling Trap is far from a harmonic

potential, it is not possible to make an accurate mathematical prediction. An experimental approach is therefore adopted in order to determine the motion frequencies.

As previously stated in Sec 2.2.5, the eigenmotions of the ion can not only be detected by measuring induced image currents, but also resonantly excited. This is accomplished by applying a radio-frequency signal to an electrode that matches the frequency of the ion's motion. Depending on the eigenmotion, the external field should be either a dipole field (axial motion) or a quadrupole field (magnetron and cyclotron motion) which consequently affects the choice of electrode. A quadrupole field can only be produced by a segmented electrode, which leaves for the Cooling Trap the central ring electrode as the only option.

In order to detect the eigenmotion non-destructively, it is essential to precisely adjust the power of the signal. If the power is excessive, the energy in the eigenmotion will increase to a point where the storage conditions become unstable and the ions are lost. This behaviour is exploited in this initial attempt to determine the oscillation frequencies. A signal generator is connected to two opposing segments of the ring electrode to excite the ions' eigenmotions. The amplitude is set to $10\,\mathrm{V}$ and the frequency is scanned between two injections of ions. The ions are captured by potentials of $7\,\mathrm{kV}$ at the capture electrodes and stored for $1\,\mathrm{s}$ and the signal is sent in for $900\,\mathrm{ms}$, starting $50\,\mathrm{ms}$ after the ion capture. Due to limitations of the frequency generator, the magnetic field of the trap is reduced to $(3.84\pm0.01)\,\mathrm{T}$, in order to make the cyclotron frequency accessible.

After extraction, the ions are guided towards the MCP detector in GTR5DK2, where the induced signal is observed. The results of this frequency scan are presented in Fig. 5.10, which plots the integrated ion signal as a function of the frequency setting of the frequency generator. Multiple dips are visible in the observed spectrum that correspond to different excitation schemes. It should be noted that not only the fundamental frequency of a motion is suited to excite the eigenmotion, but also higher harmonics and combinations of any of these frequencies. From a mathematical perspective, excitation by a sender frequency $\omega$ is possible if the condition

$$\omega = a\omega_{\mathrm{z}} + b\omega_{+} + c\omega_{-} \tag{5.10}$$

is satisfied with integer $a, b, c$. In Tab. 5.4, the centres of the fundamental frequencies are listed together with the corresponding FWHM.

The efficiency of the excitation depends on the eigenmotion and the values $a, b$, and $c$. Higher harmonics are generally less suited for excitation than the fundamental frequency, as demonstrated in the bottom-left frame of Fig. 5.10, which shows the fundamental magnetron frequency and its second harmonic. Furthermore, the width of the motional frequency spectrum is of importance. As the Cooling Trap does not provide a harmonic potential, the width becomes dependent on the energy in the eigenmotion, as discussed in Sec. 2.2.3. This is experimentally demonstrated by the particularly broad distribution of the axial frequency (Fig. 5.10 bottom-middle). Given that the electric potential is constant for a significant portion of the trap volume, the distribution of the axial frequency is largely determined by the kinetic energy distribution of the ion bunch. In this example, a modulation is also observed in the dip produced by the axial eigenfrequency. This observation can be attributed to a simultaneous high-harmonic excitation of the magnetron motion, which explains the modulation frequency being equal to the magnetron frequency. The weaker excitation by the higher harmonic is insufficient to cause unstable trapping conditions. However, it does transfer energy into the magnetron eigenmotion. As a consequence, the magnetron radius is reduced and the subsequent ejection and transfer of the ion beam towards the detector facilitated, thereby counteracting the reduction in ion signal by excitation of the axial
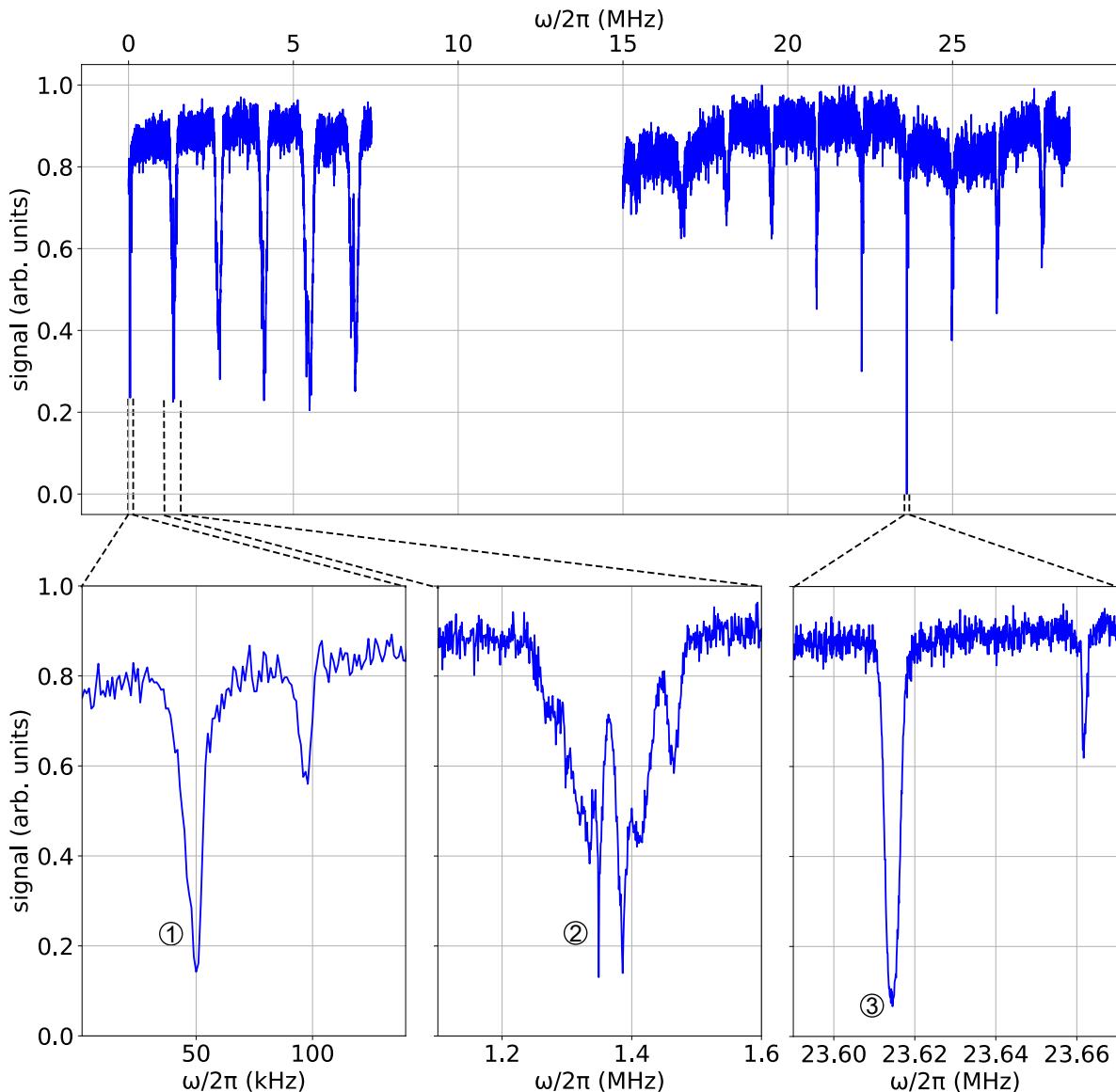
Figure 5.10: Top: detected ion signal after 1 s of storage with an RF signal sent into the trap plotted against the frequency. A dip in the signal intensity indicates a resonant excitation of an ion motion, which subsequently results in a (partial) loss of the stored ions. A multitude of dips are visible, each corresponding to either the axial, magnetron or cyclotron eigenmotion, a higher harmonic of these motions, or an arbitrary combination. Bottom: close-up of the fundamental frequencies. In the left subplot, the magnetron frequency of $(49.01\pm0.13)$ kHz (1) is visible as well as its second harmonic. The axial frequency is observable in the middle plot (2) with a centre frequency of $(1368.5\pm1.3)$ kHz. The signal is modulated with the magnetron frequency, which is indicative of simultaneous high-harmonic excitation of this eigenmotion. On the right-hand side, the cyclotron frequency (3) is observed at a frequency of $(23614.466\pm0.013)$ kHz, together with the sum of cyclotron and magnetron frequency.

Table 5.4: Central frequency of the eigenmotions of ions trapped in the Cooling Trap along with the corresponding FWHM. The listed positions correspond to the dips marked in Fig. 5.10. Ions are confined in the Penning trap by potentials of 7 kV and a magnetic field of (3.84±0.01) T.

| eigenmotion | position | $\omega/2\pi$ (kHz) | FWHM/$2\pi$ (kHz) |
|---|---|---|---|
| magnetron motion | 1 | 49.01±0.13 | 9.61±0.38 |
| axial motion | 2 | 1368.5±1.3 | 152.1±3.8 |
| cyclotron motion | 3 | 23614.466±0.013 | 3.933±0.031 |

motion.

In contrast to the relatively broad axial eigenmotion, the observed dip caused by the cyclotron frequency (Fig. 5.10 bottom-right) is a factor of 40 narrower as it is predominately determined by the magnetic field. The relative width of the cyclotron frequency is approximately $2 \cdot 10^{-4}$, which corresponds to the homogeneity of the magnetic field. In close proximity to the cyclotron frequency an additional dip is observed that is caused by the sum frequency of the cyclotron and magnetron eigenmodes.

Furthermore, these results allow for an empirical prediction of the eigenfrequencies for different settings of magnetic and electric fields:

- In the case of the magnetron motion, this is already described in [104]. The magnetron motion is purely determined by regions with overlapping magnetic and electric fields. Regions of constant electric potential exert no influence on the magnetron motion and can therefore be disregarded from consideration. This effectively reduces the relevant trap length and consequently yields an 'effective' trap parameter of $d_{\mathrm{eff}} = 5.6$ cm, which is within the uncertainty of the value determined in [104] of (5.0±0.6) cm.

- Like the magnetron frequency, also the reduced cyclotron frequency is defined by the the $E \times B$-field. As the above described measurement is conducted with the central ring electrode, which is located in a region of constant field, the influence of the electric field can be neglected. Instead, the observable motion corresponds to the unperturbed cyclotron motion, which is defined in Eq. 2.37. For $^{40}\mathrm{Ar}^{16+}$ ions and the measured frequency of $\omega_{\mathrm{c}}/2\pi = 23614.466 \pm 0.013$ kHz, this yields a magnetic field of 3.841 T. This result is well within the uncertainty of the set value of (3.84±0.01) T applied to the superconducting magnet.

- As previously stated in Sec. 2.2.3, for the 'bathtub'-like configuration of the Cooling Trap, the axial frequency is expected to be solely dependent upon the ions' kinetic energy. A purely geometrical approach would suggest that $^{40}\mathrm{Ar}^{16+}$ ions with an energy of (4005.8±2.2) eV/$q$ oscillate between the capture electrodes with a frequency of

$$ f = \frac{v}{2l} = \frac{\sqrt{2E/m}}{2l}, \tag{5.11} $$

with the distance between the capture electrodes $l$. Given that the employed ring electrode is located right in between the capture electrodes, the observed frequency will be twice this value. This approach yields an axial frequency of (1437.5±19.2) kHz, a value that is

slightly higher than the measured frequency. This purely geometrical approach assumes a constant velocity, which is not applicable when the ions approach the capture electrode and enter the steadily rising electric field. Consequently, the velocity in these regions is reduced and, resulting in a corresponding decrease in the observed axial frequency. Simulations that account for the electric field gradient but also neglect the magnetic field predict an axial frequency of 1386.8 kHz, which is in better agreement with the observed value. This supports the hypothesis that the axial frequency only depends on the ions' kinetic energy.

The results presented in this section represent a first step towards the implementation of non-destructive detection methods for the Cooling Trap. In order to observe the small signals induced by the ions' eigenmotions, it is necessary to employ prior amplification and noise-filtering. In a first step, the corresponding filters will be installed outside the Cooling Trap, which facilitates the design but also diminishes the signal-to-noise ratio. To achieve superior precision and efficiency, cryogenic filters can be installed in the intended space in close proximity to the electrode stack (left side in Fig. 3.7). Both approaches are currently in the design phase, with the plan to install the non-cryogenic devices by the end of this year. Given that the efficiency of both filters and amplifiers is frequency-dependent, the here presented determination of the ions' eigenfrequencies in the trap greatly facilitates the design and renders an extensive search over a broad frequency range unnecessary.

## 5.3 Electron Cooling

The preceding two sections 5.1 and 5.2 demonstrate that the requirements expected from simulations for electron cooling are satisfied for both the electron plasma and ions. When stored independently, a plasma of more than $10^9$ electrons can be produced, and the ion lifetime significantly exceeds the predicted time required for electron cooling. Consequently, the next step is the simultaneous storage of both particle species and the demonstration of electron cooling. As outlined in Sec. 2.2.3, the simultaneous confinement of particles of opposite charges necessitates the utilisation of a nested-trap potential and therefore a combination of the trapping schemes for ion and electron storage. A schematic representation of this configuration is provided in Fig. 5.11. which will be discussed in more detail in the following:

- **Step 1:** The electrons are produced by the electron source, guided into the Cooling Trap and captured between negative potentials applied to the long end-cap electrodes. Subsequently forming a well of positive potential with the ring electrode allows for compression of the electron plasma in the centre of the Penning trap. By repeating this procedure, it is possible to accumulate multiple injections of electrons, thereby increasing their number and density (see Sec. 5.1.1).

- **Step 2:** Prior to the production of ions, the trap potentials may be adjusted to accommodate a range of potential scenarios. Should the kinetic energy of the ions be altered upon injection, the reference potential can be set accordingly. Furthermore the long end-cap electrodes can be returned to ground potential, thereby ensuring that all electrons are confined in the trap centre. An alternative approach is to elongate the electron plasma by removing the positive potential well, thus storing the electrons between the long end-cap electrodes. After the preparation of the trap and electron plasma is finished, the ions are
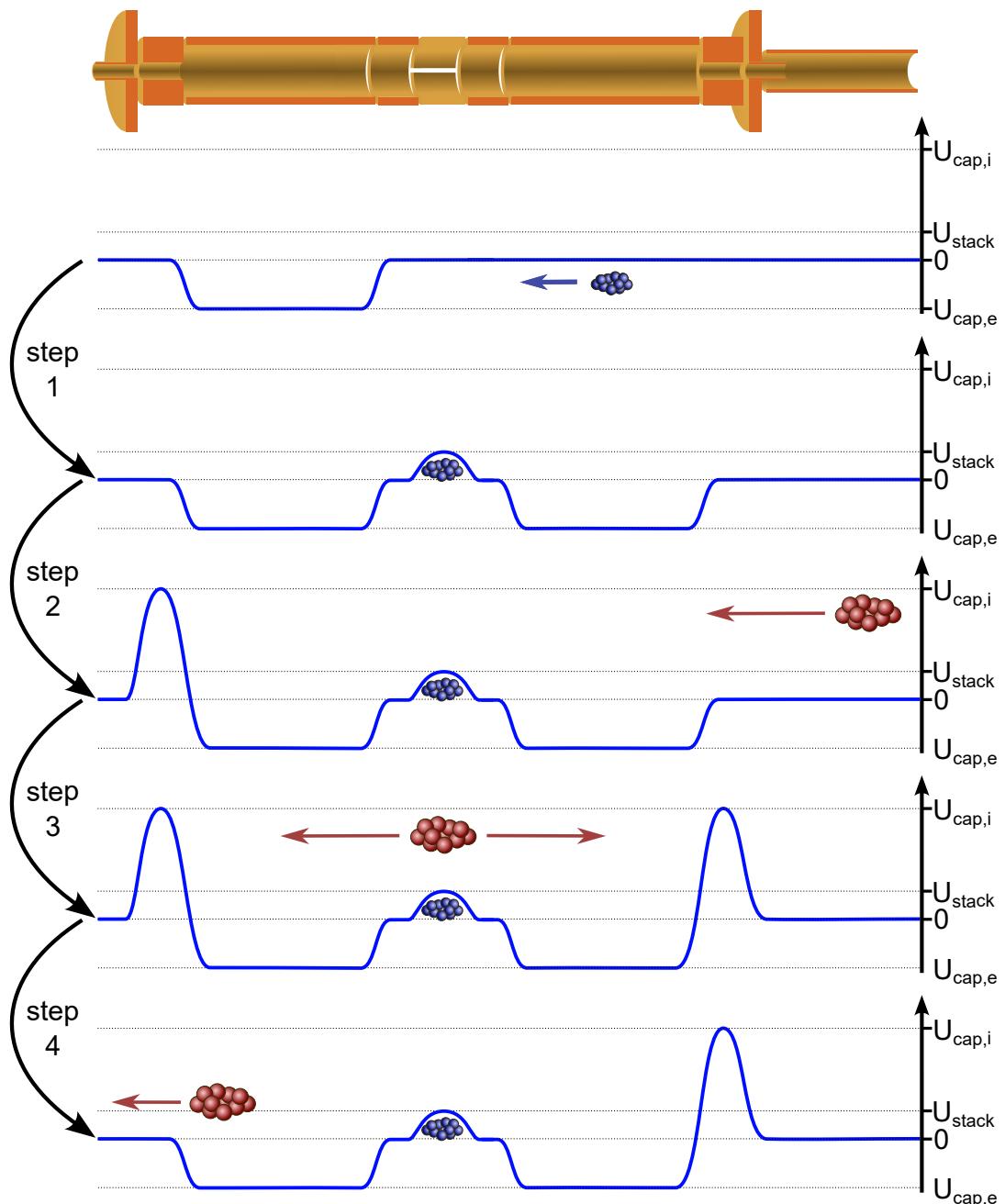
Figure 5.11: Trapping scheme for the simultaneous storage of electrons and ions in a nested trap for application of electron cooling. First, the electrons are injected and captured in the trap centre, with the option of stacking multiple injections (step 1). Subsequent to the electron preparation, ions are injected (step 2) and trapped simultaneously with the electron plasma (step 3). With electrons and ions confined in the same volume, the ions are cooled by the electrons. Following the cooling process, the ions are ejected towards an MCP detector for analysis (step 4). At this point, the electrons can be removed from the trap or kept for the next injection of ions.

produced in the EBIT ion source, guided to the trap (see Sec. 5.2.1) and captured with a trapping scheme analogous to the one described in Sec. 4.3.1.

- **Step 3:** The incoming ion bunch is captured between the two capture electrodes and is now simultaneously stored with the electron plasma. During the predefined storage time, the ions can transfer energy to the co-trapped electrons via Coulomb interactions. The amount of transferred energy is contingent upon the storage time and properties of the ion and electron clouds. In order to facilitate the transport to the detector after storage, the mean kinetic energy of the ions can be increased upon extraction by elevating the trap to a more positive potential.

- **Step 4:** After the electron cooling is finished, the ions are extracted from the trap and guided towards a detector. The remaining electrons can either stay trapped until the next injection of ions or be removed from the trap by setting the confining potentials back to ground.

### 5.3.1 Experimental Results

In order to demonstrate electron cooling experimentally, electrons and ions are confined simultaneously according to the trapping scheme presented in Fig. 5.11. A bunch of approximately $10^9$ electrons is captured between the two long end-cap electrodes and stored for a period of 1 s. During this interval, the electrons dissipate their kinetic energy and accumulate in the positive potential well formed by the ring electrode. Subsequently, the right end cap is lowered, the next injection of electrons transported into the Penning trap and also captured between the long end-cap electrodes. This process is repeated until a plasma comprising a total of ten stacks of electrons is accumulated in the trap. By removing the positive potential well in the trap centre, the electron cloud is evenly distributed between the long end-cap electrodes.

Following the plasma preparations, a bunch of approximately $10^5$ $Ar^{16+}$-ions is prepared in the EBIT, transported to the Cooling Trap and confined between the capture electrodes. Both electrons and ions are stored simultaneously for a storage time of 2 s, after which the ions are ejected towards the MCP detector in GTR5DK2. The observed signal, averaged over five repetitions of the above described process, is plotted in Fig. 5.12 in red over the ions' time-of-flight to the detector. The time reference is provided by the trigger signal, which is sent to the switching unit connected to the left capture electrode. In the same figure, a reference signal is plotted in blue for which no electrons are trapped simultaneously with the ions. In order to ensure comparable conditions, only the trigger for the flash lamp that produces the electrons in the first place is omitted in the scheme employed for the reference signal. All other aspects, namely potentials, storage time or switching processes, remain unaltered.

The ion signal, produced with a co-trapped electron plasma, commences after a longer time-of-flight of $t_2 = (3.22 \pm 0.02)$ µs in comparison to the reference signal, which starts after $t_1 = (3.04 \pm 0.02)$ µs. Given that the time-of-flight is inversely proportional to the square root of the kinetic energy, this proves that the ions transfer a part of their kinetic energy to the electron plasma. The derived values for the time-of-flight allow for the calculation of the energy of the ions after storage $E_{\text{kin,f}}$ with co-trapped electrons via the equation

$$E_{\text{kin,f}} = \left(\frac{t_1}{t_2}\right)^2 E_{\text{kin,i}}, \tag{5.12}$$
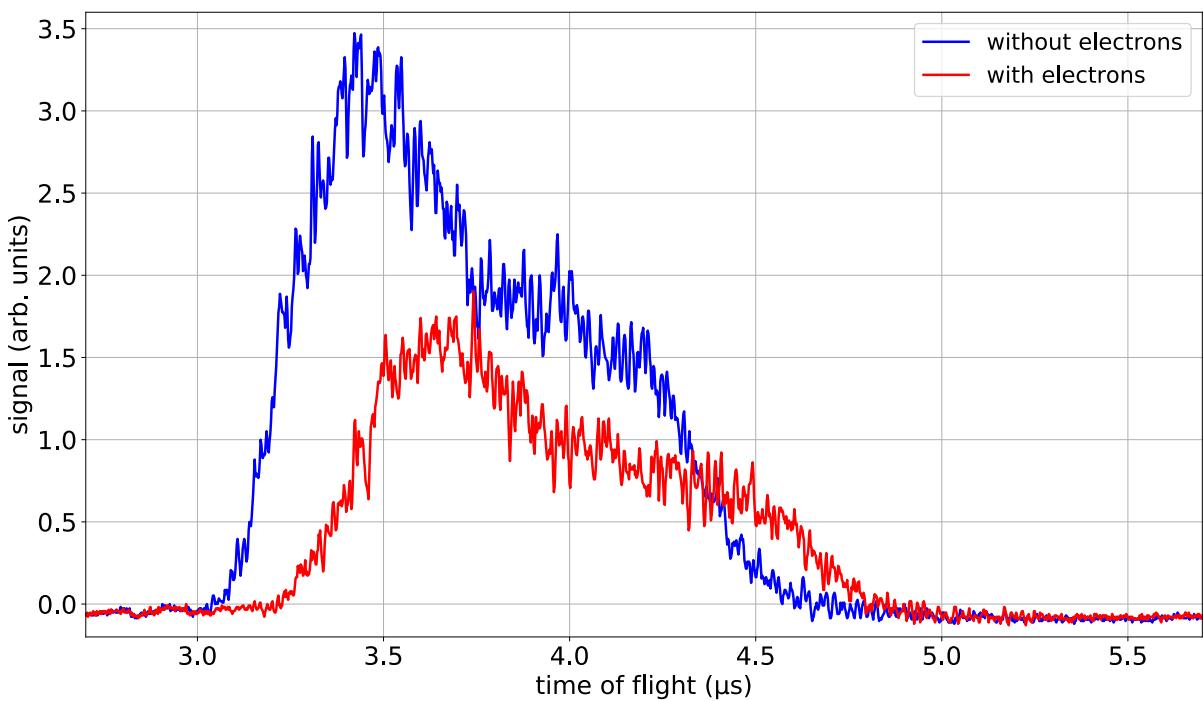
Figure 5.12: Signal of ions stored with a co-trapped electron plasma (red) observed after ejection on the MCP detector GTR5EF2 plotted over the ions' time-of-flight to the detector. As a reference, the ion signal without a simultaneously stored electron cloud is depicted in blue. The longer time-of-flight of the red curve proves a transfer of kinetic energy to the electron plasma.

where $E_{\mathrm{kin,i}}$ denotes the initial kinetic energy of the ion bunch. Assuming again that no energy transfer occurs during charge exchange and that the initial kinetic energy of the ion bunch is $(4006\pm2)\,\mathrm{eV}/q$, which is equivalent to $(64.1\pm0.1)\,\mathrm{keV}$, the total kinetic energy of the ions is reduced to $(57.1\pm1.0)\,\mathrm{keV}$ or $(3570\pm65)\,\mathrm{eV}/q$ for a charge state of 16+.

In addition to the difference in time-of-flight, the two signals depicted in Fig. 5.12 also significantly differ in intensity. Ions that are not simultaneously stored with electrons produce approximately twice the signal intensity compared to ions with co-trapped electrons. This is not attributed to an increased loss of stored ions; rather it can be explained by the energy acceptance of the beam line between the trap and the detector. The beam line comprises two electrostatic einzel lenses, which are optimised for the transport of ions with a kinetic energy of $4\,\mathrm{keV}/q$. If ions with a different energy are transported through this beam line, a reduced transport efficiency can be expected. This is particularly the case for ions with reduced kinetic energy, given that the einzel lenses are set to a positive potential of up to $3.1\,\mathrm{kV}$. Ions with a kinetic energy below $3.1\,\mathrm{keV}/q$ are unable to pass through this einzel lens and as their kinetic energy approaches this limit, the transport efficiency decreases.

This behaviour is investigated in greater detail in a separate series of measurements. To this end, the trapping scheme is modified as follows: it starts again with a single injection of electrons, which are captured between the two long end-cap electrodes. Subsequently, one second after the electron capture, a bunch of ions is injected and stored together with the electrons for $2\,\mathrm{s}$. After the storage time, the ions are again sent to the MCP detector where their signal is observed.
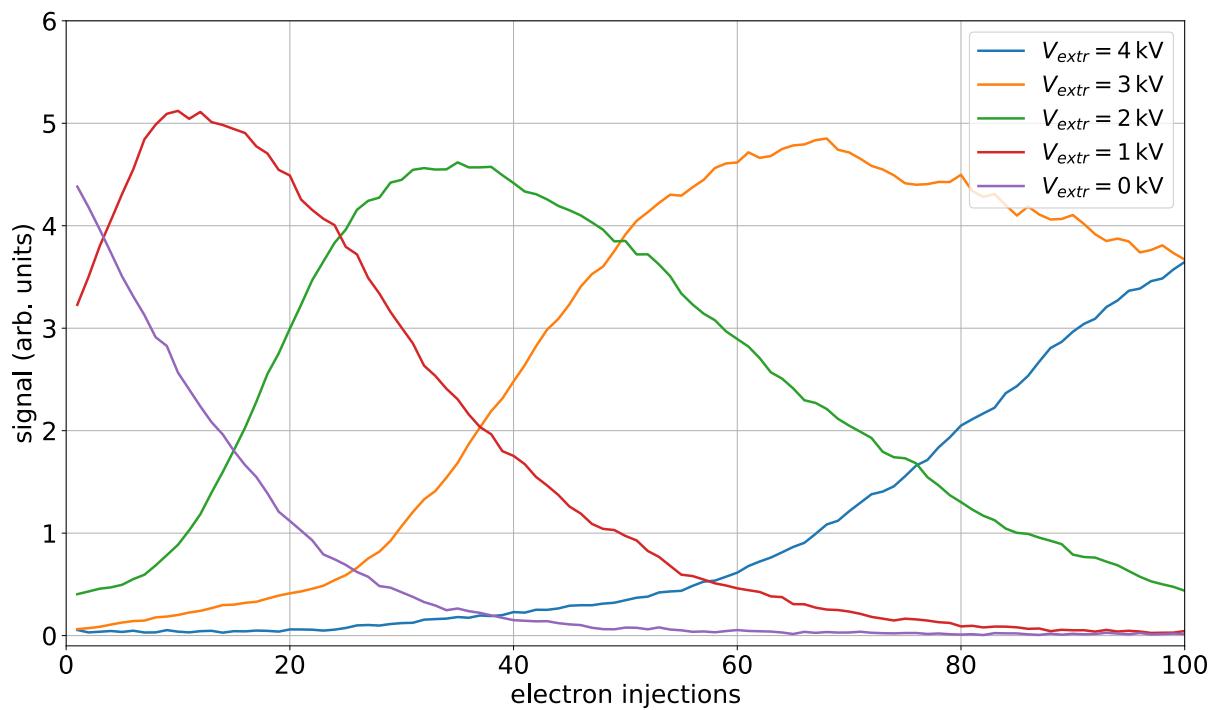
Figure 5.13: Integrated ion signal plotted against the number of electron injections for different extraction potentials. A maximum in a curve correlates with an ideal transport efficiency after ion ejection (for further details see text for details). The data points are connected to guide the eye.

The electrons remain in the trap and a second bunch of electrons is accumulated, before the next injection of ions takes place. This procedure is repeated multiple times, thereby allowing for an investigation of the ion signal with a steadily increasing amount of stored electrons.

The result of the measurement campaign is illustrated in Fig. 5.13 in purple, where the integrated ion signal is plotted against the number of electron injections. To improve the statistical reliability, this series of measurements is repeated five times, with the value for each data point subsequently averaged over all measurements. With an increasing number of injections, corresponding to higher electron densities, the ion signal decreases steadily. As the cooling power of the electron plasma increases with the electron density, a greater amount of energy is dissipated from the ion bunch, resulting in a reduction in the ion signal due to a lower transport efficiency through the beam line.

This hypothesis can be supported by conducting the same series of measurements for varying extraction potentials. If the reference potential $U_{\text{ref,f}}$ of the Cooling Trap is set to a positive value during the storage time, the ions are accelerated upon extraction according to Eq. 4.6, thus counteracting the loss in transport efficiency. The results for an extraction potential of 1 kV are presented in Fig. 5.13 in red. As the transport efficiency decreases in the purple curve for no acceleration after storage, it increases in the red curve. The maximum is reached after 11 injections, which corresponds to the point at which the ion energy after extraction meets the optimal transport conditions of the beam line. As the number of stored electrons, and consequently the cooling power are further increased, the transport efficiency begins to decline

once more, due to a further decrease in the ion energy.

The same principle is employed also for 2, 3 and 4 kV of extraction potential, as plotted in Fig. 5.13 with green, orange and blue curves, respectively. These curves all follow a comparable trend, with an initial increase in signal corresponding to a rising number of stored electrons. The higher the extraction potential is chosen, the slower is the observed increase of the ion signal. This can be attributed to a reduction in stacking efficiency. The accumulation of additional electrons is limited by the number of electrons already stored in in the positive potential well formed by the ring electrode as the space-charge limit is approached (see Sec. 5.1.1 for details). To some extent, the slope of the curves can be optimised by improving the efficiency of electron accumulation. An increase in the number of electrons accumulated with each injection would result in an overall increase in slope, both in the rising and falling sections of the curves. Nevertheless, at some point the space-charge limit is approached and the electron loss between injections will cancel with the gain from additional stacks. As the space-charge limit is determined by the stacking potential, it can be increased by the application of a higher potential.

In the case of the blue curve, which corresponds to an extraction potential of 4 kV, the point of maximum signal is not reached. Assuming that a maximum in the curve corresponds to the ideal transport conditions, which are expected at a kinetic energy of $4\,\text{keV}/q$ after ejection, for a 4 kV extraction potential this would correspond to a kinetic energy of close to $0\,\text{keV}/q$ inside the trap. As a negative energy is not possible, a decrease in the blue curve would therefore presumably indicate an actual decrease in ion number.

There are two possible mechanisms that would lead to an increased rate of ion loss compared to the storage without a co-trapped electron plasma. One option is the recombination of ions with the electron plasma to the point where confinement is no longer possible. With the kinetic energy approaching 0, it is expected that the rate of recombination will be significantly increased [97]. Alternatively, it is also possible that the ions remain confined within the negative potential well of a long end-cap electrode, which is supposed to keep the electron in the trap. If energy is transferred to the electron cloud while inside a region of negative potential with respect to the reference, at some point the ions are no longer able to leave this region. This can be observed by removing the negative potential after releasing the ion bunch, as a second signal appears that can clearly be assigned to additional ions trapped inside the long end-cap electrode. An increased rate of recombination, on the other hand, is challenging to prove with the existing means of charge separation.

Both of the above presented measurements demonstrate that the ions transfer energy to the electron plasma, resulting in a reduction in the mean kinetic energy of the ions after the storage process. However, neither of these techniques allows for more than a very rough estimation of the ion energy, and also the shape and width of the energy distribution remain unknown. In order to gain further insight into the energy distribution, the retarding field energy analyser in GTR5DK2 is employed. In each series of measurements, ions are captured in the trap for a period of 2 s after a given number of electron injections. They are then observed by the MCP detector of the RFEA while the applied potential is scanned. Following each individual measurement, the electrons are removed from the trap to ensure reproducible conditions. In order to minimise the influence of the beam line between the Cooling Trap and the detector, the ions are accelerated upon extraction with a potential $V_{\text{ext,f}}$, depending on the number of electron injections. Furthermore, the einzel lenses are changed to a negative potential which should also increase the acceptance range of the beam line.

Table 5.5: Parameters for fitting Eq. 5.8 onto the data produced by measuring ions after simultaneous storage with electrons. With the parameters for $E_{0,\mathrm{i}}$, $\sigma_{\mathrm{E,i}}$ and $A_{\mathrm{i}}$ the total kinetic energy distribution can be extracted independently of the angle. The values show a reduction in the mean kinetic energy. However, due to the high uncertainties of the fit a more detailed analysis of the ion properties remains inaccessible. Raw data and fits are displayed in figures 5.9, A.1, A.2 and A.3.

|  | no cooling | 10 stacks | 30 stacks | 40 stacks |
|---|---|---|---|---|
| $V_{\mathrm{ext,f}}$ (kV) | 0 | 0 | 3 | 3 |
| $E_{0,16}$ (eV/$q$) | 4006±2 | 3688±25 | 937±25 | 778±46 |
| $\sigma_{\mathrm{E},16}$ (eV/$q$) | 98±28 | 53±39 | $51^{+56}_{-51}$ | $19^{+36}_{-19}$ |
| $E_{0,15}$ (eV/$q$) | 4273±2 | 4049±37 | 1279±69 | 1107±109 |
| $\sigma_{\mathrm{E},15}$ (eV/$q$) | 105±47 | 117±92 | 262±122 | 269±101 |
| $E_{0,14}$ (eV/$q$) | 4578±3 | 4333±1142 | 2059±74 | 1852±87 |
| $\sigma_{\mathrm{E},14}$ (eV/$q$) | 160±56 | $319^{+497}_{-319}$ | 137±118 | 120±105 |
| $\theta_0$ (°) | 0.1±2.0 | 0.4±4.0 | 0.0±3.7 | 0.0±2.8 |
| $\sigma_\theta$ (°) | 10.5±0.2 | 12.6±0.7 | 14.6±0.5 | 5.5±0.7 |
| $A_{16}$ (arb. units) | 0.39±0.12 | 0.28±0.13 | 0.18±0.12 | 0.14±0.12 |
| $A_{15}$ (arb. units) | 0.39±0.13 | $0.46^{+0.54}_{-0.46}$ | 0.75±0.13 | 0.79±0.14 |
| $A_{14}$ (arb. units) | 0.22±0.15 | $0.21^{+0.65}_{-0.21}$ | 0.13±0.04 | 0.12±0.06 |

The data analysis is conducted in an analogous manner to that presented in Sec. 5.2.2, considering three possible charge states with variable central kinetic energies after extraction. In Tab. 5.5, the resulting fit parameters are presented together with the corresponding extraction potential. With the fitted values of the central energies, their width and amplitudes, the total kinetic energy distribution can be extracted independently of the angle under which the ions hit the detector. These distributions are plotted in Fig. 5.14. As a reference, both in the table and in the figure, the values and plot for ion storage without a co-trapped electron plasma are also provided.

The results of the measurement confirm the reduction in the mean kinetic energy with increasing amounts of stored electrons. However, due to the considerable uncertainties associated with the fit parameters, the reliability of the derived values, e.g., for the widths or amplitudes of different charge states, is very limited. For instance, while the energy width for the charge state 16+ decreases with higher cooling power, as would be expected for electron cooling, the energy width for the charge state 15+ increases. This can be attributed to the high correlation between the fit parameters. Increasing the width and amplitude of one charge state can compensate a lower amplitude in another. These results demonstrate that the detector setup in its current configuration is unable to provide a reliable assessment of the efficiency of electron cooling or charge exchange and recombination processes.

With the currently available detection methods, only the reduction of the mean kinetic energy can be proven with certainty. However, the main purpose of electron cooling is the reduction of the energy distribution width. A qualitative proof of this can be easily provided if electron cooling is
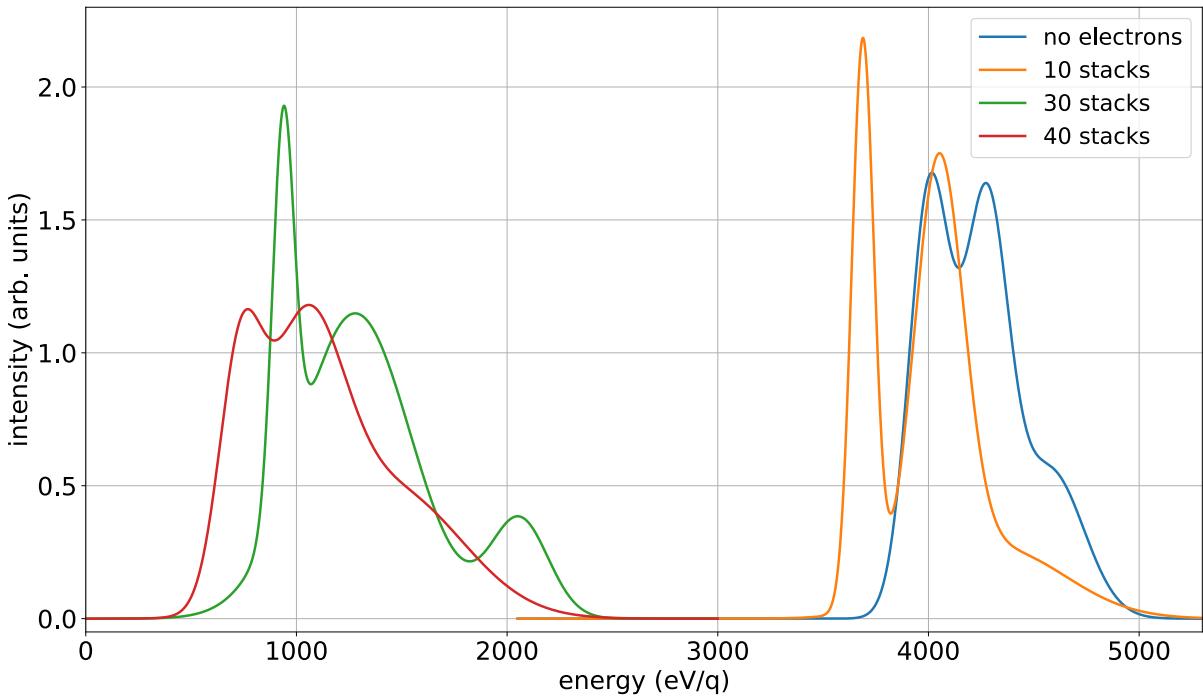
Figure 5.14: Energy distribution of ions that are stored simultaneously with an electron plasma for different numbers of electron injections. The distributions are extracted from the fit parameters presented in Tab. 5.5 and show a reduction of the mean kinetic energy with higher electron numbers. Raw data and fits are displayed in figures 5.9, A.1, A.2 and A.3.

applied to accelerator-produced ions during a beamtime. The broad energy distribution observed in Sec. 4.3 will prevent an efficient transport of the ions over a long distance. According to the discussion in Sec. 2.3.1, in particular the transport through the magnetic dipole will result in significant losses if the width of the energy distribution is not reduced in the Cooling Trap. An efficient transport through the beam line following the trap, will consequently already proof the reduction of the width of the energy distribution.

In order to investigate this observable also quantitatively, further development of the setup is required. One approach to this challenge is the implementation of charge separation following the storage process. In combination with the RFEA, this would significantly reduce the number of fit parameters, thereby facilitating the subsequent analysis. Ultimate precision may be achieved by equipping the detector with additional apertures to remove the angle dependency of the data. In Sec. 5.2.2, the current state of developments towards charge separation is presented in more detail. An alternative approach would be to employ non-destructive detection methods, which could provide further insights already during the storage and cooling process. As discussed in Sec. 5.2.3, the axial frequency of the stored ion bunch is predominantly determined by the energy distribution of the ions. A reduction in the width of the energy distribution should also result in a narrowing of the distribution of the axial frequency.

With established charge-sensitive detection methods, the process of electron cooling can be further investigated and optimised. As previously stated, the primary objective of electron cooling is the reduction of the energy width, which represents the next big step for the commissioning

process of the Cooling Trap. Furthermore, the simultaneous storage of electrons and ions must be investigated with respect to electron number and plasma density. Simulations indicate that the recombination rate between electrons and ions is particularly sensitive to these parameters. Another currently unknown variable is the spatial overlap between electrons and ions. While the position of the electron cloud can be precisely determined as presented in Sec. 5.1.2, the position of the ion bunch is uncertain. The phosphor screen detector employed for determining the position of the electron bunch is in the current state not sufficiently sensitive for ion detection. An upgrade is underway, with the installation of a single microchannel plate to improve sensitivity and also enable ion detection. With this upgrade, it will be possible to determine also the position of the ion bunch in the trap and to adjust the spacial alignment between ions and electrons.

# 6 Conclusion and Outlook

This work presented the most recent developments of the HITRAP facility, with a the particular focus on the linear decelerator and the Cooling Trap. Following a period of almost eight years of shutdown, the two deceleration stages, namely the IH-structure and the RFQ, were successfully recommissioned, thus recreating the results of the last beamtime in 2014. This objective was already achieved in the first of the three beamtime discussed in this work, which took place in 2022, when $^{58}$Ni$^{28+}$ ions were decelerated from an initial energy of 4 MeV/u to approximately 6 keV/u. The following two beamtimes, both of which took place in 2024, employed $^{12}$C$^{6+}$, $^{18}$O$^{8+}$ and $^{36}$Ar$^{18+}$ and marked the first significant advancement for the HITRAP facility in the last ten years. For the first time, the ions could be transported further along the beam line following deceleration in the RFQ. This enabled additional characterisation measurements with regard to the rebuncher and RFQ, and moreover, constituted the first determination of the RFQ's output energy with accelerator-produced ions. By analysing the $^{36}$Ar$^{18+}$ ions' time-of-flight between two spatially separated detectors, their mean kinetic energy was determined to be (6.28±0.09) keV/u.

The most significant progress was achieved with the subsequent capture of these ions in the Cooling Trap. To the authors knowledge, the confinement of accelerator-produced highly charged ions in a Penning trap has never been achieved before. The lifetime of the stored ions was found to be (11.6±0.5) s, which is, according to simulations, a sufficient period for the ultimate goal of electron cooling. Following the storage period, the ions were ejected and detected in the adjacent beam line. The kinetic energy of the ions could be arbitrarily selected by the operator by modifying the potential of the entire trap setup, thus decelerating and accelerating the ions upon injection and extraction, an indispensable feature for future operation.

Due to the limited availability of accelerator-produced ions to brief periods of beamtime, the designated next step in the commissioning of the HITRAP facility, namely electron cooling of these ions, could not be tested. Instead, the process was extensively investigated with ions produced in a local EBIT ion source. As test ion species, bunches of about $10^5$ $^{40}$Ar$^{16+}$ ions were produced in the EBIT and subsequently captured in the Cooling Trap. In preparation for the future application of non-destructive detection techniques, the frequencies of the stored ions' eigenmotions were experimentally observed. The results obtained will allow for the prediction of eigenfrequencies for various trap settings thus facilitating the preparation of non-destructive detection.

The required electrons are provided by a pulsed photoionisation source, which produces up to $5.7{\cdot}10^9$ electrons per pulse. Measurements of the space-charge potential of trapped electrons indicate that approximately $3.3{\cdot}10^9$ of these electrons can be captured for a single injection. By the application of a novel stacking technique, this number was significantly enhanced when multiple bunches of electrons were accumulated in the trap. The stored electron plasma was also employed to improve the alignment of the trap setup, thereby also increasing the density of

the plasma, both indispensable advancements for the observation of electron cooling.

In order to test electron cooling in the Penning trap, a plasma comprising approximately $10^{10}$ electrons was confined simultaneously with about $10^5$ $^{40}$Ar$^{16+}$ ions in a nested-trap potential. The transfer of energy from the ions to the electron plasma could be initially confirmed by an increased time-of-flight of the ions after extraction towards the detector. A retarding field energy analyser was employed to further investigate this phenomenon. It was observed that the kinetic energy of the ions could be reduced from an initial value of $4 \, \mathrm{keV}/q$ down to below $1 \, \mathrm{keV}/q$ after just two seconds of simultaneous storage. This constitutes the world-wide first confirmed application of electron cooling of highly charged ions in a Penning trap.

The next steps in commissioning the HITRAP facility will focus on the implementation of electron cooling also for accelerator-produced ions, representing the last major step towards the availability of heavy, highly charged ions at rest for precision experiments. This will be attempted in the next commissioning beamtime in 2025 with highly charged silver and krypton ions. In the previous runs, such heavy isotopes were beyond the range of the decelerator due to a malfunctioning IH-structure. A prior repair of this decelerator unit is already underway and will be essential for further commissioning of the decelerator.

There is already the first experimental campaign scheduled for 2025, which will employ decelerated gold ions with an energy of approximately $6 \, \mathrm{keV/u}$ for surface ionisation studies after the RFQ [20]. However, the majority of setups necessitate subsequent cooling in the Cooling Trap to allow for confinement in ion traps. These experiments include next to the already established ARTEMIS [19] and SPECTRAP [17] setups also the newly formed Helmholtz Young Investigator Group that aims to employ highly charged ions for the development of high-precision atomic clocks [4].

In preparation for the aforementioned upcoming beamtimes, the Cooling Trap will undergo further commissioning with locally produced HCI. The precision of the herein presented results is mainly limited by the lack of a reliable method for separating ion charge states after the storage and cooling process. The implementation of charge-sensitive detection methods will allow for a more comprehensive investigation of the electron cooling process. In particular, charge-changing processes, such as charge exchange with residual gas or recombination with the electron plasma require a more detailed examination. Potential approaches to this challenge include the implementation of non-destructive detection methods during the storage process and charge separation after extraction, both of which are currently under development.

# A  Appendix

## A.1  Raw Data of Electron Cooling Measurements
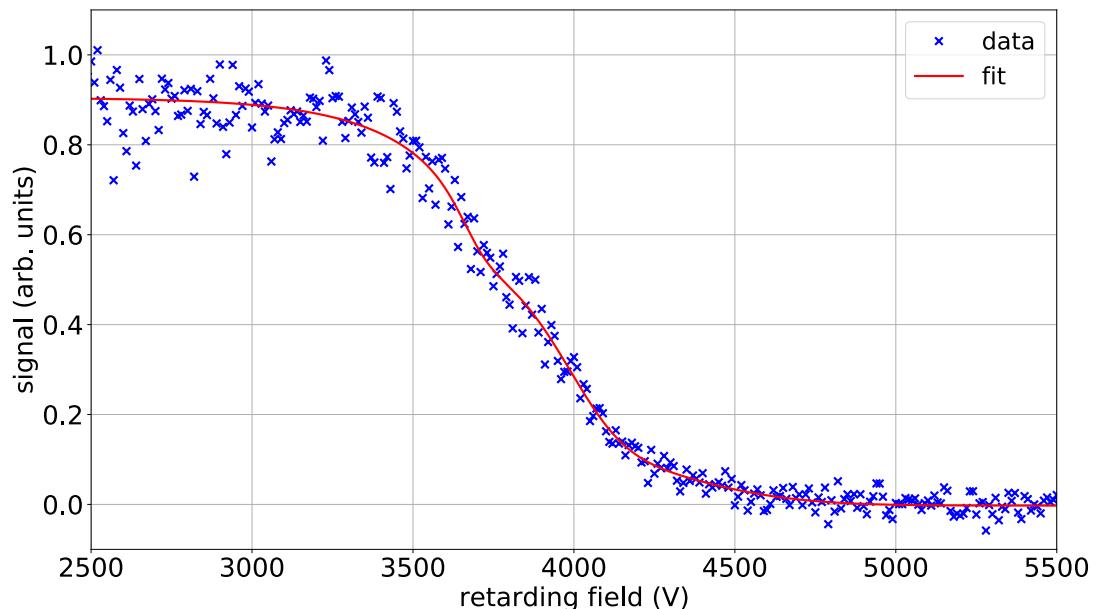


Figure A.1: Signal of stored ions with 10 stacks of electrons measured on the retarding field energy analyser plotted over the applied retarding field potential (blue). The data is fitted with the function given in Eq. 5.8 for three charge states (16+, 15+ and 14+) which results in the red curve. Details and fit parameters can be found in Sec. 5.3.1 and Tab.5.5.
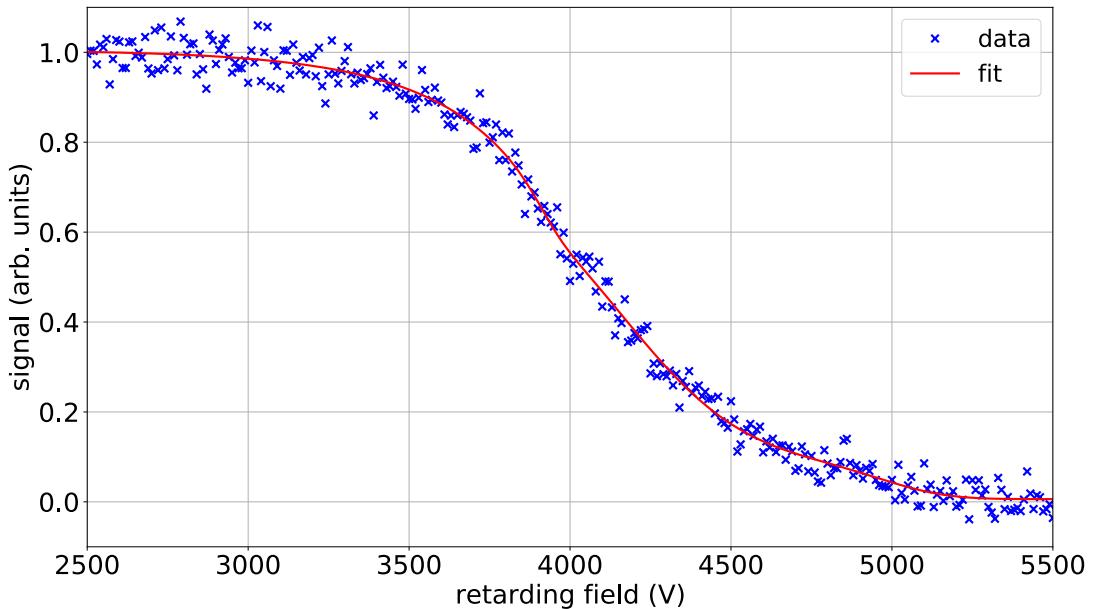
Figure A.2: Signal of stored ions with 30 stacks of electrons measured on the retarding field energy analyser plotted over the applied retarding field potential (blue). The data is fitted with the function given in Eq. 5.8 for three charge states (16+, 15+ and 14+) which results in the red curve. Details and fit parameters can be found in Sec. 5.3.1 and Tab.5.5.
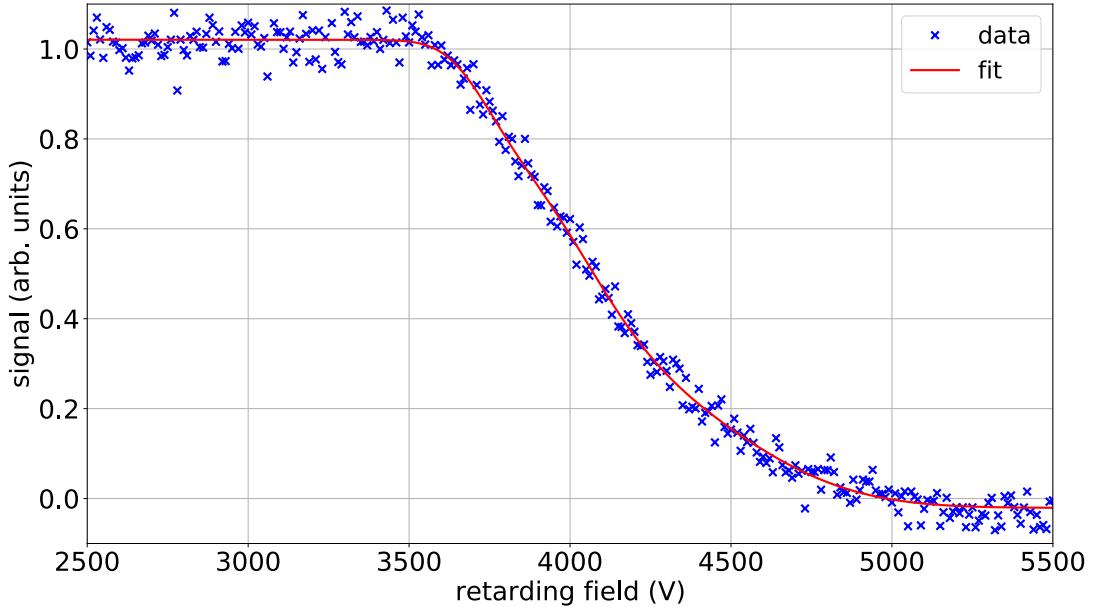


Figure A.3: Signal of stored ions with 40 stacks of electrons measured on the retarding field energy analyser plotted over the applied retarding field potential (blue). The data is fitted with the function given in Eq. 5.8 for three charge states (16+, 15+ and 14+) which results in the red curve. Details and fit parameters can be found in Sec. 5.3.1 and Tab.5.5.

## A.2 Schematic Layout and Nomenclature of the HITRAP facility
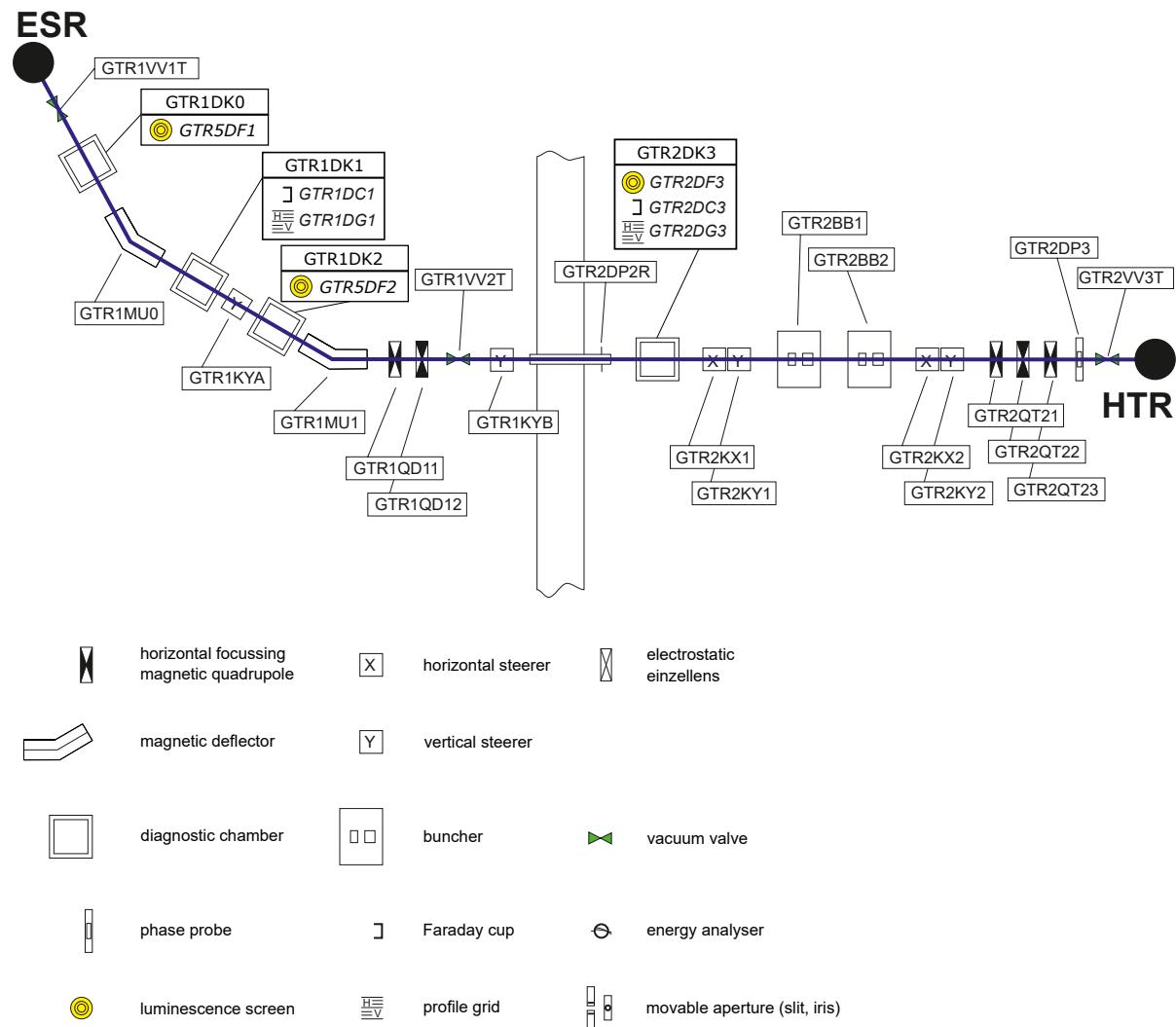


Figure A.4: Overview of all installed devices in the beam line, starting at the ESR ending in front of the IH structure.
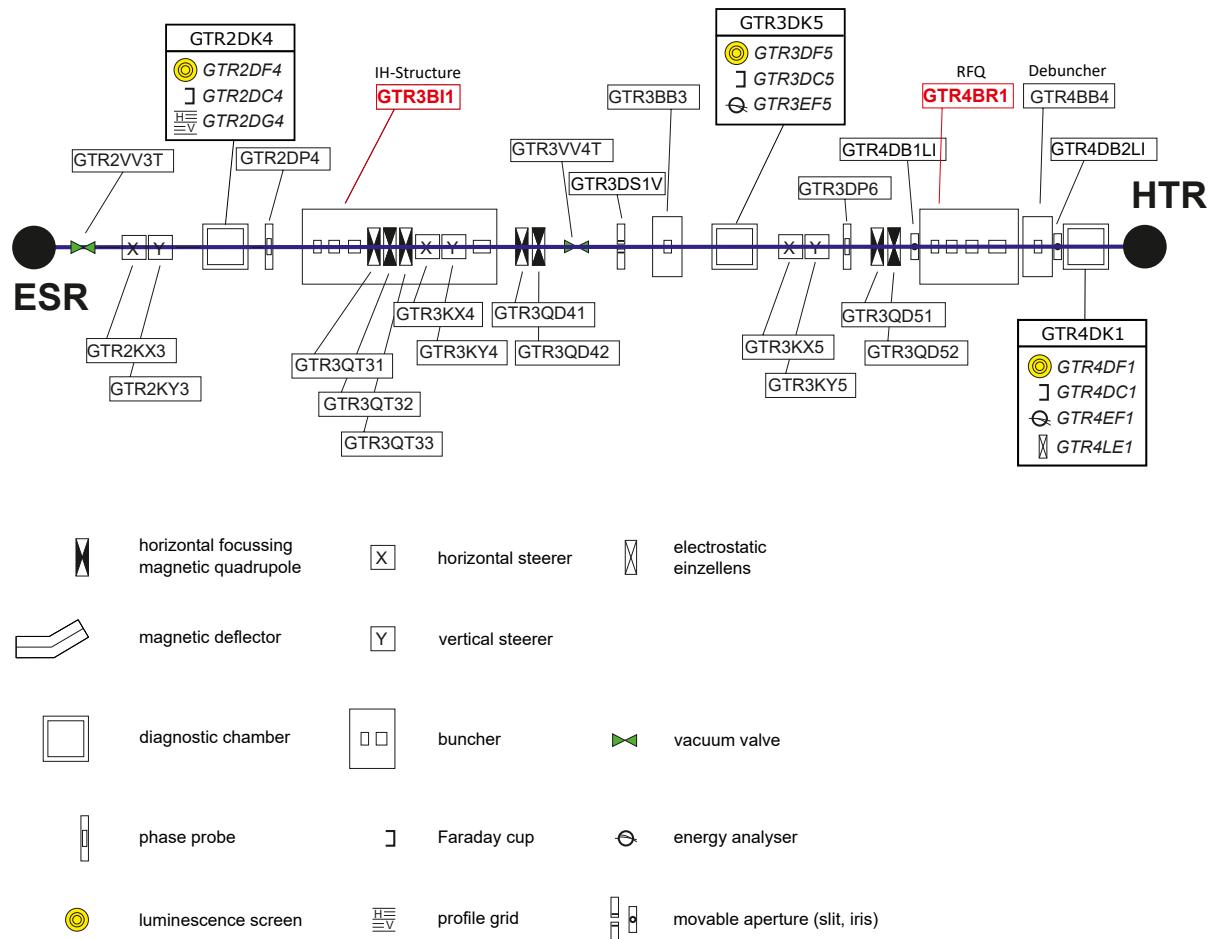
Figure A.5: Overview of all installed devices in the beam line, starting in front of the IH structure until the first diagnostic chamber after the RFQ.
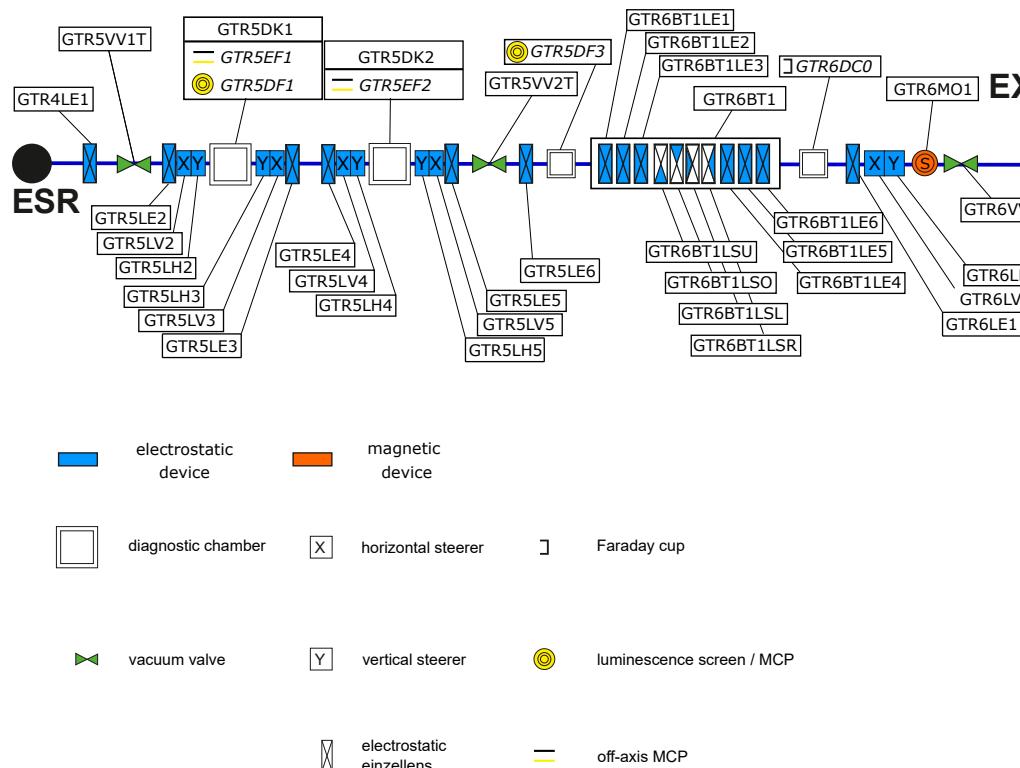
Figure A.6: Overview of all installed devices in the beam line, starting after the RFQ ending after the Cooling Trap.
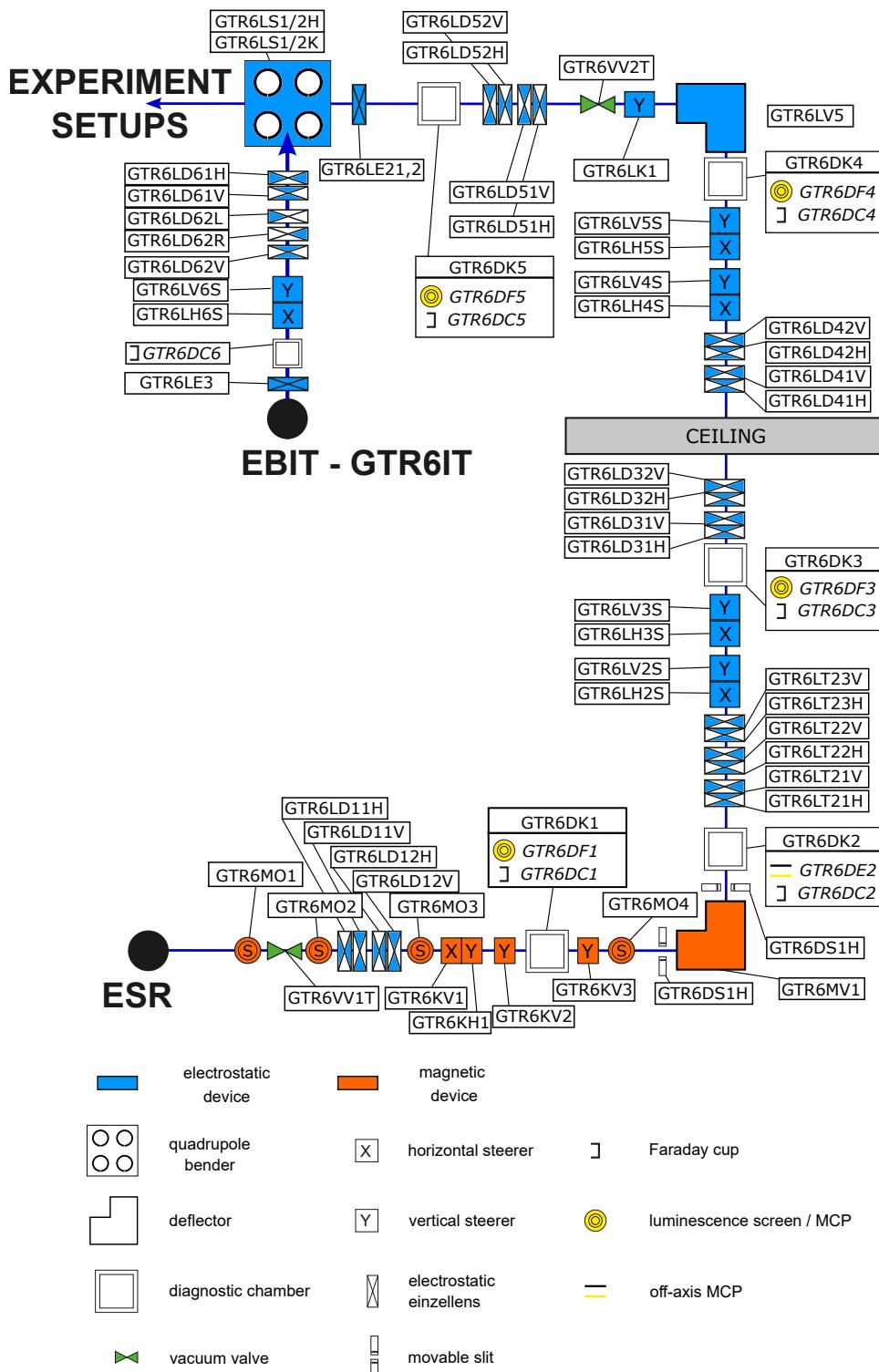
Figure A.7: Overview of all installed devices in the beam line, starting after the cooling trap until the EBIT and experimental platform.

# Bibliography

[1]     C. E. Anderson and K. W. Ehlers, "Ion Source for the Production of Multiply Charged Heavy Ions", Review of Scientific Instruments **27**, 809–817 (1956).

[2]     E. O. Lawrence, "The evolution of the cyclotron", Nobel Lecture, 23 (1951).

[3]     G. Kraft et al., "Tumortherapy with ion beams", Nuclear Instruments and Methods in Physics Research Section A: Accelerators, Spectrometers, Detectors and Associated Equipment **454**, 1–10 (2000).

[4]     S. A. King, L. J. Spieß, P. Micke, et al., "An optical atomic clock based on a highly charged ion", Nature **611**, 43–47 (2022).

[5]     V. M. Shabaev, A. N. Artemyev, V. A. Yerokhin, O. M. Zherebtsov, and G. Soff, "Towards a Test of QED in Investigations of the Hyperfine Splitting in Heavy Ions", Phys. Rev. Lett. **86**, 3959–3962 (2001).

[6]     H. Häffner, T. Beier, N. Hermanspahn, et al., "High-Accuracy Measurement of the Magnetic Moment Anomaly of the Electron Bound in Hydrogenlike Carbon", Phys. Rev. Lett. **85**, 5308–5311 (2000).

[7]     S. Sturm, A. Wagner, B. Schabinger, et al., "$g$ Factor of Hydrogenlike $^{28}\text{Si}^{13+}$", Phys. Rev. Lett. **107**, 023002 (2011).

[8]     V. Hannen, J. Vollbrecht, Z. Andelkovic, et al., "Lifetimes and g-factors of the HFS states in H-like and Li-like bismuth", Journal of Physics B: Atomic, Molecular and Optical Physics **52**, 085003 (2019).

[9]     G. Zschornacka, M. Schmidt, and A. Thorn, "Electron beam ion sources", CAS-CERN Accelerator School: Ion Sources (2014).

[10]    A. Girard, D. Hitz, G. Melin, and K. Serebrennikov, "Electron cyclotron resonance plasmas and electron cyclotron resonance ion sources: Physics and technology (invited)", Review of Scientific Instruments **75**, 1381–1388 (2004).

[11]    V. Shevelko, N. Winckler, and I. Y. Tolstikhina, "Stripping of relativistic uranium-ion beams by foils", Nuclear Instruments and Methods in Physics Research Section B: Beam Interactions with Materials and Atoms **479**, 23–34 (2020).

[12]    J. Ullmann, Z. Andelkovic, C. Brandau, et al., "High precision hyperfine measurements in Bismuth challenge bound-state strong-field QED", Nature communications **8**, 15484 (2017).

[13]    D. Hanneke, S. Fogwell, and G. Gabrielse, "New Measurement of the Electron Magnetic Moment and the Fine Structure Constant", Phys. Rev. Lett. **100**, 120801 (2008).

[14]    A. Aeppli, K. Kim, W. Warfield, M. S. Safronova, and J. Ye, "Clock with $8 \times 10^{-19}$ Systematic Uncertainty", Phys. Rev. Lett. **133**, 023401 (2024).

[15] A. Rischka, H. Cakir, M. Door, et al., "Mass-Difference Measurements on Heavy Nuclides with an eV/c$^2$ Accuracy in the PENTATRAP Spectrometer", Phys. Rev. Lett. **124**, 113001 (2020).

[16] F. Herfurth, T. Beier, L. Dahl, et al., "Highly charged ions at rest: The HITRAP project at GSI", AIP Conference Proceedings **793**, 278–292 (2005).

[17] T. Murböck, S. Albrecht, Z. Andelkovic, et al., "SpecTrap: precision spectroscopy of highly charged ions—status and prospects", Physica Scripta **2013**, 014096 (2013).

[18] P. Micke, T. Leopold, S. King, et al., "Coherent laser spectroscopy of highly charged ions using quantum logic", Nature **578**, 60–65 (2020).

[19] M. Vogel, G. Birkl, M. Ebrahimi, et al., "Extreme-field physics in Penning traps: The ARTEMIS and HILITE experiments", Hyperfine Interactions **236**, 65–71 (2015).

[20] A. Niggas, M. Werl, F. Aumayr, and R. A. Wilhelm, "Charge exchange of slow highly charged ions from an electron beam ion trap with surfaces and 2d materials", Journal of Physics B: Atomic, Molecular and Optical Physics **57**, 072001 (2024).

[21] F. Herfurth, Z. Andelkovic, W. Barth, et al., "The HITRAP facility for slow highly charged ions", Physica Scripta **2015**, 014065 (2015).

[22] P. A. M. Dirac and R. H. Fowler, "The quantum theory of the electron", Proceedings of the Royal Society of London. Series A, Containing Papers of a Mathematical and Physical Character **117**, 610–624 (1928).

[23] J. Verdú, S. Djekić, S. Stahl, et al., "Electronic $g$ Factor of Hydrogenlike Oxygen $^{16}$O$^{7+}$", Phys. Rev. Lett. **92**, 093002 (2004).

[24] Sturm, Sven and Vogel, Manuel and Köhler-Langes, Florian and Quint, Wolfgang and Blaum, Klaus and Werth, Günter, "High-Precision Measurements of the Bound Electron's Magnetic Moment", Atoms **5** (2017).

[25] W. Demtröder, *Experimentalphysik 3: Atome, Moleküle und Festkörper*, Vol. 5 (Springer Spektrum, 2016).

[26] A. V. Volotka, D. A. Glazov, G. Plunien, and V. M. Shabaev, "Progress in quantum electrodynamics theory of highly charged ions", Annalen der Physik **525**, 636–646 (2013).

[27] W. Nörtershäuser, J. Billowes, M. Bissell, et al., *Dielectronic Recombination-assisted laser spectroscopy: A new tool to investigate the hyperfine-puzzle in Bi$^{80+,82+}$*, approved experiment proposal E128, GSI G-PAC45, 2022.

[28] T. Beier, "The $g_j$ factor of a bound electron and the hyperfine structure splitting in hydrogenlike ions", Physics Reports **339**, 79–213 (2000).

[29] J. Schwinger, "On Gauge Invariance and Vacuum Polarization", Phys. Rev. **82**, 664–679 (1951).

[30] M. H. Horst, "Laser Spectroscopy of $^{208}$Bi$^{82+}$ and Commissioning of the HITRAP Cooling Trap", PhD thesis (Technische Universität, Darmstadt, 2023).

[31] B. Povh, K. Rith, C. Scholz, F. Zetsche, and W. Rodejohann, "Particles and nuclei", An Introduction to the Physical Concepts, Berlin and Heidelberg: Springer-Verlag (2015).

[32] S. Sturm, G. Werth, and K. Blaum, "Electron g-factor determinations in Penning traps", Annalen der Physik **525**, 620–635 (2013).

[33] N. P. M. Brantjes, "The g-factor of hydrogen-like heavy ions as a test for QED", PhD thesis (Ruperto-Carola Universität, Heidelberg, 2012).

[34] G. Breit, "The Magnetic Moment of the Electron", Nature **122**, 649–649 (1928).

[35] V. M. Shabaev, D. A. Glazov, M. B. Shabaeva, et al., "g factor of high-Z lithiumlike ions", Phys. Rev. A **65**, 062104 (2002).

[36] N. Bohr, "On the constitution of atoms and molecules", The London, Edinburgh, and Dublin Philosophical Magazine and Journal of Science **26**, 1–25 (1913).

[37] H. A. Bethe, "The Electromagnetic Shift of Energy Levels", Phys. Rev. **72**, 339–341 (1947).

[38] W. Demtröder, *Experimentalphysik 4: Kern-, Teilchen- und Astrophysik*, Vol. 4 (Springer Spektrum, 2014).

[39] V. M. Shabaev, "Hyperfine structure of hydrogen-like ions", Journal of Physics B: Atomic, Molecular and Optical Physics **27**, 5825 (1994).

[40] O. Brüning, H. Burkhardt, and S. Myers, "The large hadron collider", Progress in Particle and Nuclear Physics **67**, 705–734 (2012).

[41] K. Blasche and B. Franczak, "The heavy ion synchrotron SIS", Proc. EPAC, 9 (1992).

[42] P. Spiller, R. Balss, P. Bartolome, et al., "The FAIR Heavy Ion Synchrotron SIS100", Journal of Instrumentation **15**, T12013 (2020).

[43] B. Franzke, "The heavy ion storage and cooler ring project ESR at GSI", Nuclear Instruments and Methods in Physics Research Section B: Beam Interactions with Materials and Atoms **24-25**, 18–25 (1987).

[44] F. Herfurth, A. Brauning-Demian, W. Enders, H. Danared, et al., "The low energy storage ring CRYRING@ESR", Proc. COOL'13, 189–191 (2013).

[45] V. Shevelko, Y. A. Litvinov, T. Stöhlker, and I. Y. Tolstikhina, "Lifetimes of relativistic heavy-ion beams in the High Energy Storage Ring of FAIR", Nuclear Instruments and Methods in Physics Research Section B: Beam Interactions with Materials and Atoms **421**, 45–49 (2018).

[46] P. Seelig, S. Borneis, A. Dax, et al., "Ground State Hyperfine Splitting of Hydrogenlike $^{207}$Pb$^{81+}$ by Laser Excitation of a Bunched Ion Beam in the GSI Experimental Storage Ring", Phys. Rev. Lett. **81**, 4824–4827 (1998).

[47] D. R. DeWitt, R. Schuch, W. Zong, et al., "Dielectronic recombination of Ar$^{13+}$ at CRYRING", Physica Scripta **1997**, 96 (1997).

[48] T. Radon, H. Geissel, G. Münzenberg, et al., "Schottky mass measurements of stored and cooled neutron-deficient projectile fragments in the element range of $57 \leq Z \leq 84$", Nuclear Physics A **677**, 75–99 (2000).

[49] B. Seiferle, L. von der Wense, P. V. Bilous, et al., "Energy of the $^{229}$Th nuclear clock transition", Nature **573**, 243–246 (2019).

[50] K. Pyka, N. Herschbach, J. Keller, and T. E. Mehlstäubler, "A high-precision segmented Paul trap with minimized micromotion for an optical multiple-ion clock", Applied Physics B **114**, 231–241 (2014).

[51] C. D. Bruzewicz, J. Chiaverini, R. McConnell, and J. M. Sage, "Trapped-ion quantum computing: Progress and challenges", Applied Physics Reviews **6**, 021314 (2019).

[52] F. M. Penning, "Die Glimmentladung bei niedrigem Druck zwischen koaxialen Zylindern in einem axialen Magnetfeld", physica **3**, 873–894 (1936).

[53] H. Dehmelt, "Experiments with an Isolated Subatomic Particle at Rest", Reviews of modern physics **62**, 525 (1990).

[54] J. Repp, C. Böhm, J. Crespo López-Urrutia, et al., "PENTATRAP: a novel cryogenic multi-Penning-trap experiment for high-precision mass measurements on highly charged ions", Applied Physics B **107**, 983–996 (2012).

[55] J. Verdú, S. Kreim, J. Alonso, et al., "Penning Trap Measurement of the Magnetic Moment of the Antiproton", AIP Conference Proceedings **796**, 260–265 (2005).

[56] K. Kromer, C. Lyu, M. Door, et al., "High-precision mass measurement of doubly magic $^{208}$Pb", The European Physical Journal A **58**, 202 (2022).

[57] H. Raimbault-Hartmann, D. Beck, G. Bollen, et al., "A cylindrical Penning trap for capture, mass selective cooling, and bunching of radioactive ion beams", Nuclear Instruments and Methods in Physics Research Section B: Beam Interactions with Materials and Atoms **126**, 378–382 (1997).

[58] L. S. Brown and G. Gabrielse, "Geonium theory: Physics of a single electron or ion in a Penning trap", Rev. Mod. Phys. **58**, 233–311 (1986).

[59] W. Jones, "Earnshaw's theorem and the stability of matter", European Journal of Physics **1**, 85 (1980).

[60] M. Vogel, *Particle Confinement in Penning Traps* (Springer, 2023).

[61] J. Malmberg and C. Driscoll, "Long-Time Containment of a Pure Electron Plasma", Physical Review Letters **44**, 654 (1980).

[62] G. Gabrielse and F. Mackintosh, "Cylindrical Penning traps with orthogonalized anharmonicity compensation", International Journal of Mass Spectrometry and Ion Processes **57**, 1–17 (1984).

[63] G. Gabrielse, L. Haarsma, and S. Rolston, "Open-endcap Penning traps for high precision experiments", International Journal of Mass Spectrometry and Ion Processes **88**, 319–332 (1989).

[64] H.-U. Hasse, S. Becker, G. Dietrich, et al., "External-ion accumulation in a Penning trap with quadrupole excitation assisted buffer gas cooling", International Journal of Mass Spectrometry and Ion Processes **132**, 181–191 (1994).

[65] M. Singer, S. König, M. R. Stoneking, et al., "Non-neutral plasma manipulation techniques in development of a high-capacity positron trap", Review of Scientific Instruments **92**, 123504 (2021).

[66] G. Vorobjev, C. Andre, W. Barth, et al., "Diagnostic scheme for the HITRAP decelerator", 10th European Workshop on Beam Diagnostics and Instrumentation for Particle Accelerators DIPAC2011, 311–313 (2015).

[67] W. Shockley, "Currents to Conductors Induced by a Moving Point Charge", Journal of Applied Physics **9**, 635–636 (2004).

[68] S. Ramo, "Currents Induced by Electron Motion", Proceedings of the IRE **27**, 584–585 (1939).

[69] S. Schmidt, T. Murböck, Z. Andelkovic, et al., "Non-destructive single-pass low-noise detection of ions in a beamline", Review of Scientific Instruments **86**, 113302 (2015).

[70] O. Kester, W. Barth, L. Dahl, et al., "Deceleration of highly charged ions for the HITRAP project at GSI", Proc. of the LINAC06, Knoxville, Tennessee, USA, 189–191 (2006).

[71] J. Ketelaer, K. Blaum, M. Block, et al., "Recent developments in ion detection techniques for Penning trap mass spectrometry at TRIGA-TRAP", The European Physical Journal A **42**, 311–317 (2009).

[72] D. J. Wineland and H. G. Dehmelt, "Principles of the stored ion calorimeter", Journal of Applied Physics **46**, 919–930 (1975).

[73] C.-E. Roux, "High-resolution mass spectrometry: The trap design and detection system of PENTATRAP and new Q-values for neutrino studies", PhD thesis (Ruprecht-Karls Universität Heidelberg, 2012).

[74] A. G. Marshall, C. L. Hendrickson, and G. S. Jackson, "Fourier transform ion cyclotron resonance mass spectrometry: A primer", Mass spectrometry reviews **17**, 1–35 (1998).

[75] Z. Andelkovic, "Setup of a Penning trap for precision laser spectroscopy at HITRAP", PhD thesis (Johannes Gutenberg-Universität, Mainz, 2012).

[76] C. Bowick, *RF circuit design* (Elsevier, 2011).

[77] J. J. Bollinger, D. Heinzen, F. Moore, et al., "Electrostatic modes of ion-trap plasmas", Physical Review A **48**, 525 (1993).

[78] P. Paasche, C. Angelescu, S. Ananthamurthy, et al., "Instabilities of an electron cloud in a Penning trap", The European Physical Journal D-Atomic, Molecular, Optical and Plasma Physics **22**, 183–188 (2003).

[79] T. Porobić, M. Beck, M. Breitenfeldt, et al., "Space-charge effects in Penning ion traps", Nuclear Instruments and Methods in Physics Research Section A: Accelerators, Spectrometers, Detectors and Associated Equipment **785**, 153–162 (2015).

[80] A. Müller and E. Salzborn, "Scaling of cross sections for multiple electron transfer to highly charged ions colliding with atoms and molecules", Physics Letters A **62**, 391–394 (1977).

[81] S. Aumüller, L. Bozyk, and P. Spiller, "Room temperature vacuum chamber with cryogenic installations", 14th International Particle Accelerator Conference, 4279–4282 (2023).

[82] J. Liu, E. J. Salumbides, U. Hollenstein, et al., "Determination of the ionization and dissociation energies of the hydrogen molecule", The Journal of chemical physics **130**, 174306 (2009).

[83] J. Ye, S. Blatt, M. M. Boyd, et al., "Precision measurement based on ultracold atoms and cold molecules", International Journal of Modern Physics D **16**, 2481–2494 (2007).

[84] G. K. Campbell and W. D. Phillips, "Ultracold atoms and precise time standards", Philosophical Transactions of the Royal Society A: Mathematical, Physical and Engineering Sciences **369**, 4078–4089 (2011).

[85]  M. Vogel and W. Quint, "Trap-assisted precision spectroscopy of highly charged ions", Journal of Physics B: Atomic, Molecular and Optical Physics **42**, 154016 (2009).

[86]  S. Humphries, *Charged particle beams* (Courier Corporation, 2002).

[87]  G. R. Blumenthal and R. J. Gould, "Bremsstrahlung, Synchrotron Radiation, and Compton Scattering of High-Energy Electrons Traversing Dilute Gases", Rev. Mod. Phys. **42**, 237–270 (1970).

[88]  W. M. Itano, J. C. Bergquist, J. J. Bollinger, and D. J. Wineland, "Cooling methods in ion traps", Physica Scripta **1995**, 106 (1995).

[89]  Z. Andelkovic, R. Cazan, W. Nörtershäuser, et al., "Laser cooling of externally produced Mg ions in a Penning trap for sympathetic cooling of highly charged ions", Phys. Rev. A **87**, 033423 (2013).

[90]  S. Ulmer, H. Kracke, K. Blaum, et al., "The quality factor of a superconducting rf resonator in a magnetic field", Review of Scientific Instruments **80**, 123302 (2009).

[91]  R. deCarvalho, J. M. Doyle, B. Friedrich, et al., "Buffer-gas loaded magnetic traps for atoms and molecules: A primer", The European Physical Journal D-Atomic, Molecular, Optical and Plasma Physics **7**, 289–309 (1999).

[92]  C. Droese, S. Eliseev, K. Blaum, et al., "The cryogenic gas stopping cell of SHIPTRAP", Nuclear Instruments and Methods in Physics Research Section B: Beam Interactions with Materials and Atoms **338**, 126–138 (2014).

[93]  S. Schmidt, T. Murböck, Z. Andelkovic, et al., "Sympathetic cooling in two-species ion crystals in a Penning trap", Journal of Modern Optics **65**, 538–548 (2018).

[94]  G. Gabrielse, X. Fei, L. A. Orozco, et al., "Cooling and slowing of trapped antiprotons below 100 meV", Phys. Rev. Lett. **63**, 1360–1363 (1989).

[95]  D. S. Hall and G. Gabrielse, "Electron Cooling of Protons in a Nested Penning Trap", Phys. Rev. Lett. **77**, 1962–1965 (1996).

[96]  S. F. Paul, "Precision mass measurements for the astrophysical rp-process and electron cooling of trapped ions", PhD thesis (Ruperto-Carola Universität, Heidelberg, 2023).

[97]  G. Maero, "Cooling of highly charged ions in a Penning trap for HITRAP", PhD thesis (Ruperto-Carola Universität, Heidelberg, 2008).

[98]  G. Zwicknagel, "Electron Cooling of Highly Charged Ions in Penning Traps", AIP Conference Proceedings **862**, 281–291 (2006).

[99]  A. S. Richardson, *2019 NRL plasma formulary* (Naval Research Laboratory Washington, DC, 2019).

[100]  J. Bernard, J. Alonso, T. Beier, et al., "Electron and positron cooling of highly charged ions in a cooler Penning trap", Nuclear Instruments and Methods in Physics Research Section A: Accelerators, Spectrometers, Detectors and Associated Equipment **532**, International Workshop on Beam Cooling and Related Topics, 224–228 (2004).

[101]  L. H. Andersen and J. Bolko, "Radiative recombination between fully stripped ions and free electrons", Phys. Rev. A **42**, 1184–1191 (1990).

[102]  D. A. Knapp, R. E. Marrs, M. B. Schneider, et al., "Dielectronic recombination of heliumlike ions", Phys. Rev. A **47**, 2039–2046 (1993).

[103] A. Müller and A. Wolf, "Production of antihydrogen by recombination of $\bar{p}$ with $e^+$: What can we learn from electron–ion collision studies?", Hyperfine Interactions **109**, 233–267 (1997).

[104] S. Rausch, M. Horst, Z. Andelkovic, et al., "Commissioning of the HITRAP Cooling Trap with Offline Ions", Atoms **10** (2022).

[105] G. Münzenberg, S. Hofmann, F. Heßberger, et al., "Identification of element 107 by $\alpha$ correlation chains", Zeitschrift für Physik A Atoms and Nuclei **300**, 107–108 (1981).

[106] G. Münzenberg, P. Armbruster, H. Folger, et al., "Identification of element 108", Zeitschrift für Physik A Atoms and Nuclei **317**, 235–236 (1984).

[107] G. Münzenberg, W. Reisdorf, S. Hofmann, et al., "Evidence for element 109 from one correlated decay sequence following the fusion of $^{58}$Fe with $^{209}$Bi", Zeitschrift für Physik A Atoms and Nuclei **315**, 145–158 (1984).

[108] A. Ghiorso, D. Lee, L. Somerville, et al., "Evidence for the possible synthesis of element 110 produced by the $^{59}$Co + $^{209}$Bi reaction", Physical Review C **51**, R2293 (1995).

[109] S. Hofmann, V. Ninov, F. Heßberger, et al., "The new element 111", Zeitschrift für Physik A Hadrons and Nuclei **350**, 281–282 (1995).

[110] S. Hofmann, V. Ninov, F. Hessberger, et al., "The new element 112", Zeitschrift für Physik A Hadrons and Nuclei **354**, 229–230 (1996).

[111] W. Barth, M. Basten, C. Burandt, et al., "Advanced basic layout of the HElmholtz LInear ACcelerator for cw heavy ion beams at GSI", Journal of Physics: Conference Series **2687**, 052009 (2024).

[112] M. Durante, P. Indelicato, B. Jonson, et al., "All the fun of the FAIR: fundamental physics at the facility for antiproton and ion research", Physica Scripta **94**, 033001 (2019).

[113] W. Geithner, Private communication, 2024.

[114] Z. Nouri, R. Li, R. Holt, and S. Rosner, "A Penning sputter ion source with very low energy spread", Nuclear Instruments and Methods in Physics Research Section A: Accelerators, Spectrometers, Detectors and Associated Equipment **614**, 174–178 (2010).

[115] R. Hollinger, M. Galonska, and P. Spadtke, "Development of a vacuum arc ion source for injection of high current uranium ion beam into the unilac at GSI", XXIst International Symposium on Discharges and Electrical Insulation in Vacuum, 2004. Proceedings. ISDEIV. **2**, 547–549 (2004).

[116] I. Brown and E. Oks, "Vacuum arc ion sources: recent developments and applications", IEEE Transactions on Plasma Science **33**, 1931–1943 (2005).

[117] H. Wiedemann, *Particle accelerator physics* (Springer Nature, 2015).

[118] J. Glatz and L. Groening, "Beam Acceleration in the Single-Gap Resonator Section of the UNILAC Using Alternating Phase Focusing", Proc. of the EPAC-02, Paris, 897–899 (2002).

[119] W. Barth, U. Scheeler, H. Vormann, et al., "High brilliance beam investigations at the universal linear accelerator", Physical Review Accelerators and Beams **25**, 040101 (2022).

[120] D. Ondreka, C. Dimopoulou, H. Hüther, et al., "Recommissioning of SIS18 after FAIR upgrades", 10th Int. Particle Accelerator Conf.(IPAC'19), Melbourne, Australia, 19-24 May 2019, 932–935 (2019).

[121] H. Geissel, P. Armbruster, K. H. Behr, et al., "The GSI projectile fragment separator (FRS): a versatile magnetic system for relativistic heavy ions", Nuclear Instruments and Methods in Physics Research Section B: Beam Interactions with Materials and Atoms **70**, 286–297 (1992).

[122] M. Steck and Y. A. Litvinov, "Heavy-ion storage rings and their use in precision experiments with highly charged ions", Progress in Particle and Nuclear Physics **115**, 103811 (2020).

[123] F. Nolden, K. Beckert, F. Caspers, et al., "Stochastic cooling at the ESR", Nuclear Instruments and Methods in Physics Research Section A: Accelerators, Spectrometers, Detectors and Associated Equipment **441**, 219–222 (2000).

[124] D. Möhl, "Stochastic cooling", CAS - CERN Accelerator School : 5th Advanced Accelerator Physics Course, 587–671 (1995).

[125] G. Budker, N. Dikanskij, D. Pestrikov, et al., "Experimental studies of electron cooling", Part. Accel. **7**, 197–211 (1976).

[126] M. Steck, P. Beller, K. Beckert, B. Franzke, and F. Nolden, "Electron cooling experiments at the ESR", Nuclear Instruments and Methods in Physics Research Section A: Accelerators, Spectrometers, Detectors and Associated Equipment **532**, International Workshop on Beam Cooling and Related Topics, 357–365 (2004).

[127] C. Scheidenberger, K. Beckert, P. Beller, et al., "Isobar separation at FRS-ESR - a development towards pure isomeric stored beams", Hyperfine Interactions **173**, 61–66 (2006).

[128] B. Schlitt, K. Beckert, F. Bosch, et al., "Schottky mass spectrometry at the ESR: a novel tool for precise direct mass measurements of exotic nuclei", Nuclear Physics A **626**, Proceedings of the Third International Conference on Nuclear Physics at Storage Rings, 315–325 (1997).

[129] M. Steck, K. Beckert, P. Beller, et al., "Improved Performance of the Heavy Ion Storage Ring ESR", Proceedings of EPAC 2004, Lucerne, Switzerland, 1168–1170 (2004).

[130] D. Winzen, V. Hannen, M. Bussmann, et al., "Laser spectroscopy of the $^2S_{1/2}$-$^2P_{1/2}$, $^2P_{3/2}$ transitions in stored and cooled relativistic $C^{3+}$ ions", Scientific reports **11**, 9370 (2021).

[131] J. Vollbrecht, Z. Andelkovic, A. Dax, et al., "Laser spectroscopy of the ground-state hyperfine structure in H-like and Li-like bismuth", Journal of Physics: Conference Series **583**, 012002 (2015).

[132] J. Jin, H. Bekker, T. Kirschbaum, et al., "Excitation and probing of low-energy nuclear states at high-energy storage rings", Phys. Rev. Res. **5**, 023134 (2023).

[133] K. T. Mohr, "First laser spectroscopy of $Mg^+$ at CRYRING@ ESR and He-Like Boron at HITRAP", PhD thesis (Darmstadt, 2022).

[134] D. Zisis, "Design of a New Penning Trap for SPECTRAP", Masterthesis (Uppsala, 2023).

[135] K. Kanika, "Studies and Cooling of Highly Charged Ion Ensembles in the ARTEMIS Trap and High-Precision Mass Measurements of $^{221}$Fr, $^{219}$Rn, $^{213}$Bi, $^{211}$Pb, $^{209}$Pb, $^{207}$Tl and $^{207}$Pb at SHIPTRAP", PhD thesis (Johannes Gutenberg-Universität, Mainz, 2023).

[136] W. T. Milner, "Double-Drift Beam Bunching Systems", IEEE Transactions on Nuclear Science **26**, 1445–1449 (1979).

[137] C. Kitegi, U. Ratzinger, and S. Minaev, "The IH cavity for HITRAP", Proceedings of the LINAC 2004, Lübeck, Germany, 54–56 (2004).

[138] L. Dahl, W. Barth, M. Kaiser, et al., "The HITRAP decelerator project at GSI", Proc. of the EPAC2006, Edinburgh, UK, 1568–1570 (2006).

[139] R. Tiede, U. Ratzinger, H. Podlech, C. Zhang, and G. Clemente, "KONUS beam dynamics designs using H-mode cavities", Proc. HB'08, 223–230 (2008).

[140] M. Maier et al., "Offline commissioning of the old and new HITRAP RFQ", GSI Scientific Reports, 272 (2012).

[141] S. Yaramyshev, W. Barth, G. Clemente, et al., "A new Design of the RFQ-Decelerator for HITRAP", GSI Scientific Reports, 274 (2012).

[142] F. Chill, "Vermessung der Pumpeigenschafen einer kryogenen Oberfäche", PhD thesis (Johann Wolfgang Goethe-Universität, Frankfurt am Main, 2016).

[143] W. E. Gifford, "The Gifford-McMahon Cycle", Advances in Cryogenic Engineering, edited by K. D. Timmerhaus, 152–159 (1966).

[144] F. Herfurth, S. Eliseev, O. Kester, et al., "The HITRAP project at GSI: trapping and cooling of highly-charged ions in a Penning trap", TCP 2006: Proceedings of the 4th International Conference on Trapped Charged Particles and Fundamental Physics (TCP 2006) held in Parksville, Canada, 3–8 September, 2006, 249–257 (2007).

[145] Z. Andelkovic, J. Fischer, F. Herfurth, et al., "Development of the HITRAP cooling trap and the EBIT offline ion source", Hyperfine Interactions **240**, 1–9 (2019).

[146] J. Viering, "Design und Inbetriebnahme der neuen HITRAP Kühlfalle", Masterthesis (Darmstadt, 2018).

[147] T. Mohamed, H. Imao, N. Oshima, A. Mohri, and Y. Yamazaki, "Fast electron accumulation and its mechanism in a harmonic trap under ultrahigh vacuum conditions", Physics of Plasmas **18**, 032507 (2011).

[148] A. Einstein, "Über einem die Erzeugung und Verwandlung des Lichtes betreffenden heuristischen Gesichtspunkt", Annalen der physik **4**, 132–148 (1905).

[149] C. Krantz, "Intense Electron Beams from GaAs Photocathodes as a Tool for Molecular and Atomic Physics", PhD thesis (Ruperto-Carola Universität, Heidelberg, 2009).

[150] J. Scheer and J. van Laar, "GaAs-Cs: A new type of photoemitter", Solid State Communications **3**, 189–193 (1965).

[151] *Xenon Flash Lamps Technical Information*, Datasheet, Hamamatsu Photonics K.K, Nov. 2022.

[152] K. Leach, A. Grossheim, A. Lennarz, et al., "The TITAN in-trap decay spectroscopy facility at TRIUMF", Nuclear Instruments and Methods in Physics Research Section A: Accelerators, Spectrometers, Detectors and Associated Equipment **780**, 91–99 (2015).

[153] P. M. Müller, "Laserspectroscopic determination of the nuclear charge radius of $^{13}$C", PhD thesis (Technische Universität, Darmstadt, 2024).

[154] U. Rosengård, G. Rouleau, and K. Rensfelt, "The Stockholm ECR ion source injector project", Nuclear Instruments and Methods in Physics Research Section B: Beam Interactions with Materials and Atoms **139**, 428–430 (1998).

[155] B. O'Rourke, S. Geyer, A. Silze, et al., "The SPARC EBIT at GSI; commissioning and future plans at the HITRAP beamline", Journal of Physics: Conference Series **163**, 012103 (2009).

[156] A. Sokolov, F. Herfurth, O. Kester, et al., "SPARC EBIT — a charge breeder for the HITRAP project", Journal of Instrumentation **5**, C11001 (2010).

[157] A. Lapierre, G. Bollen, D. Crisp, et al., "First two operational years of the electron-beam ion trap charge breeder at the National Superconducting Cyclotron Laboratory", Phys. Rev. Accel. Beams **21**, 053401 (2018).

[158] R. E. Marrs, S. R. Elliott, and D. A. Knapp, "Production and Trapping of Hydrogenlike and Bare Uranium Ions in an Electron Beam Ion Trap", Phys. Rev. Lett. **72**, 4082–4085 (1994).

[159] K. Brown and G. Tautfest, "Faraday-cup monitors for high-energy electron beams", Review of Scientific Instruments **27**, 696–702 (1956).

[160] B. Walasek-Hohne, C. Andre, P. Forck, et al., "Scintillating Screen Applications in Accelerator Beam Diagnostics", IEEE Transactions on Nuclear Science **59**, 2307–2312 (2012).

[161] M. Vogel, D. Winters, H. Ernst, H. Zimmermann, and O. Kester, "Scintillation light produced by low-energy beams of highly-charged ions", Nuclear Instruments and Methods in Physics Research Section B: Beam Interactions with Materials and Atoms **263**, 518–522 (2007).

[162] P. Bolton, M. Borghesi, C. Brenner, et al., "Instrumentation for diagnostics and control of laser-accelerated proton (ion) beams", Physica Medica **30**, 255–270 (2014).

[163] R. Paschotta, *Microchannel Plates*, RP Photonics Encyclopedia, June 2019.

[164] J. L. Wiza et al., "Microchannel plate detectors", Nucl. Instrum. Methods **162**, 587–601 (1979).

[165] A. Reiter, C. Kleffner, and B. Schlitt, "Improved Signal Treatment for Capacitive Linac Pickups", Proceedings of DIPAC2011, 128–130 (2011).

[166] F. Herfurth, W. Barth, G. Clemente, et al., "HITRAP — Heavy, Highly-Charged Ions and Antiprotons at Rest", Acta Physica Polonica B **41**, 457 (2010).

[167] S. Fedotova, "Experimental characterization of the Hitrap Cooler trap with highly charged ions", PhD thesis (Ruperto-Carola Universität, Heidelberg, 2013).

[168] H. Poth and R. Hasse, *The HITRAP project at GSI*, tech. rep. (Gesellschaft fuer Schwerionenforschung mbH, 1990).

[169] L. Dahl, W. Barth, T. Beier, et al., "The HITRAP-DECELERATOR for heavy highly-charged ions", proceedings of the LINAC04, Lübeck, Germany, 39 (2004).

[170] F. Herfurth, T. Beier, L. Dahl, et al., "Precision measurements with highly charged ions at rest: The HITRAP project at GSI", International Journal of Mass Spectrometry **251**, 266–272 (2006).

[171] L. Dahl, W. Barth, P. Gerhard, et al., "The HITRAP Decelerator Project at GSI-Status and Commissioning Report", Proc. LINAC08, MOP019, 100–102 (2008).

[172] M. Puglisi, "Conventional RF cavity design", CAS - CERN Accelerator School : RF Engineering for Particle Accelerators, 156–197 (1992).

[173] D. Beck, M. Kreider, C. Prados, et al., "The new White Rabbit based timing system for the FAIR facility", Proceedings of PCaPAC2012, 242–244 (2012).

[174] F. Walls, D. Wineland, and R. Drullinger, "New possibilities for frequency standards using laser cooling and detection of stored ions", in 32nd Annual Symposium on Frequency Control (1978), pp. 453–459.

[175] Drullinger, RE and Wineland, DJ and Bergquist, JC, "High-resolution optical spectra of laser cooled ions", Applied physics **22**, 365–368 (1980).

[176] L. S. Brown and G. Gabrielse, "Precision spectroscopy of a charged particle in an imperfect Penning trap", Phys. Rev. A **25**, 2423–2425 (1982).

[177] D. A. Church and H. G. Dehmelt, "Radiative Cooling of an Electrodynamically Contained Proton Gas", Journal of Applied Physics **40**, 3421–3424 (1969).

[178] D. J. Wineland, R. E. Drullinger, and F. L. Walls, "Radiation-Pressure Cooling of Bound Resonant Absorbers", Phys. Rev. Lett. **40**, 1639–1642 (1978).

[179] J. Aoki, Y. Kiwamoto, Y. Soga, and A. Sanpei, "Novel Application of Electron Vortex Dynamics to the Alignment of Magnetic and Cylinder Axes", Japanese Journal of Applied Physics **43**, 7777 (2004).

[180] J. K. Böhlke, J. R. de Laeter, P. De Bièvre, et al., "Isotopic Compositions of the Elements, 2001", Journal of Physical and Chemical Reference Data **34**, 57–67 (2005).

# Danksagung

Abschließend möchte ich mich bei allen bedanken, die mich während meines Studiums und meiner Promotion unterstützt und damit diese Arbeit ermöglicht haben.

An erster Stelle geht mein Dank natürlich an Wilfried Nörterhäuser, der mir die Möglichkeit gegeben hat, nicht nur meine Masterarbeit, sondern auch meine Promotion auf diesem einzigartigen Gebiet durchzuführen. Neben der fachlichen Unterstützung in zahlreichen Diskussionen ermöglichte er mir die Teilnahme an vielen Konferenzen und Strahlzeiten rund um den Globus, bei denen ich viele neue Erfahrungen sammeln konnte.

Als nächstes möchte ich mich bei meinen Kollegen an der GSI bedanken, insbesondere bei Zoran, der als erster Ansprechpartner immer ein offenes Ohr für mich hatte und mir unzählige Male bei größeren und kleineren Problemen weitergeholfen hat. Gleiches gilt auch für Frank und Rodolfo, die ihre große Erfahrung jederzeit gerne an mich weitergegeben haben. Ein großer Dank geht auch an Max, der vor fast fünf Jahren zusammen mit mir die Arbeit an der Kühlfalle wiederaufgenommen hatte und einen großen Anteil an den Erfolgen während meiner Promotion hat. Danke an Wolfgang und Dennis, deren Entwicklung am Kontrollsystem der Anlage mir die Arbeit immens erleichtert hat. Vielen Dank an Nils und Dimitrios für ihre tägliche Hilfe bei der Inbetriebnahme und Verbesserung der Anlage und an Konstantin für die zahlreichen tiefgehenden Diskussionen. Außerdem möchte ich mich bei Serge, Davide, Jonas, Gleb, Svetlana und Nikita für ihre Unterstützung bei der Weiterentwicklung des Experiments bedanken. Ein besonderer Dank geht an die ganze Gruppe, nicht nur für die produktive Zusammenarbeit, sondern auch für die vielen spannenden und unterhaltsamen Gespräche über alle möglichen Themen abseits der Arbeit, die ein tolles Umfeld geschaffen haben.

Bedanken möchte ich mich auch bei der LaserSpHERe-Gruppe für die vielen Diskussionen, die Unterstützung und die gute Zusammenarbeit bei zahlreichen Strahlzeiten. Insbesondere sind hier Patrick, Laura, Kristian und Bernhard zu nennen, mit denen ich viel Zeit bei Konferenzen und Strahlzeiten verbringen durfte.

Ich möchte mich auch bei Robert Roth und Michael Vogel für die Teilnahme an meiner Verteidigung bedanken.

Vielen Dank auch an meine Kommilitonen und Freunde, die mich während meines Studiums und abseits davon begleitet und unterstützt haben. Die vielen gemeinsamen Abende in Kneipen, Bars oder zu Hause auf dem Sofa, auf Partys, Konzerten oder Reisen haben immer Spaß gemacht und werden es sicher auch weiter machen. Ohne diese notwendigen Ablenkungen vom Studium und der Arbeit, wären die vergangenen Jahre nicht halb so gut gewesen.

Zum Schluss gilt mein größter Dank meiner Familie, allen voran meinen Eltern, die mich nicht nur in den letzten Jahren zu jeder Zeit und in jeder Hinsicht bedingungslos und mit viel Hingabe unterstützt haben! Diese Unterstützung hat es mir immer ermöglicht meinen Interessen nachzugehen und damit diese Arbeit erst möglich gemacht.